2021-01-14

Conceptual Design and Optimization of Hybrid Rockets

Messinger, Troy Leonard

UNIVERSITY OF CALGARY

Conceptual Design and Optimization of Hybrid Rockets

by

Troy Leonard Messinger

A THESIS

SUBMITTED TO THE FACULTY OF GRADUATE STUDIES

IN PARTIAL FULFILLMENT OF THE REQUIREMENTS FOR THE

DEGREE OF MASTER OF SCIENCE

GRADUATE PROGRAM IN MECHANICAL ENGINEERING

CALGARY, ALBERTA

JANUARY, 2021

Abstract

A framework was developed to perform conceptual multi-disciplinary design parametric and optimization studies of single-stage sub-orbital flight vehicles, and two-stage-to-orbit flight vehicles, that employ hybrid rocket engines as the principal means of propulsion. The framework was written in the Python programming language and incorporates many sub-disciplines to generate vehicle designs, model the relevant physics, and analyze flight performance. The relative performance (payload fraction capability) of different vehicle masses and feed system/propellant configurations was found. The major findings include conceptually viable pressure-fed and electric pump-fed two-stage-to-orbit configurations taking advantage of relatively low combustion pressures in increasing overall performance. The smallest launch vehicles assessed had lower payload fractions compared to larger vehicles. The vehicle configurations resulting in the highest performance used liquid oxygen and paraffin wax propellants. The smallest viable orbital launch vehicle, the vehicle with the highest payload fraction for the smallest payload considered, was a liquid oxygen and paraffin-wax-based launcher. The highest payload fraction found for the smallest payload class was 0.60 % of gross mass for a 10 kg payload delivered to 500 km Sun-synchronous orbit. The highest payload fraction for the investigated 150 kg payload class for the same Sun-synchronous orbit was found to be 1.2 %.

Table of Contents

List of Figures and Illustrations

List of Tables

List of Symbols, Abbreviations and Nomenclature

Symbol	Definition
A	Area
AR	Rocket aspect ratio
A_e	Nozzle exit area
A_p	Internal port area
A_t	Nozzle throat area
a	The regression rate proportionality parameter
BR_n	Nosecone bluntness ratio
b	Bilinear tangent steering normalized burn time modifier
c	Bilinear tangent steering shape constant
c_1	Particle swarm optimization cognitive parameter
c_2	Particle swarm optimization social parameter
c^*	Characteristic velocity
C_D	Drag coefficient
C_{D_w}	Wave drag coefficient
C_{D_f}	Skin friction drag coefficient
$C_{D_{base}}$	Base drag coefficient
C_N	Normal force coefficient
C_{N_α}	Normal force derivative wrt angle of attack
c_{pg}	Pressurant gas mass margin factor
C_T	Thrust coefficient
D	Drag force
D_{exit}	Nozzle exit diameter
E_{ep}	Electric pump required energy
F_{ax}	Axial force
f_n	Nosecone fineness ratio
G	Oxidizer axial mass flux
g	Earths local gravitational acceleration
g_0	Earths standard gravitational acceleration
ID	Inner diameter
I_{sp}	Specific impulse
I_t	Total impulse
$\mathbf{K}$	Stiffness matrix

k	Number of other particles of awareness in PSO
L	Vehicle length
$\mathbf{M}$	Mass matrix
M	Mach Number
N	Normal force
n	The regression rate exponent parameter
$\mathcal{N}$	Number of particles used in PSO
OD	The rocket body outer diameter
OF	The oxidizer-to-fuel ratio on a mass basis
OF_{av}	The burn-time-averaged oxidizer-to-fuel ratio
P_{amb}	Ambient pressure
P_c	Nominal chamber pressure
P_e	Nozzle exit pressure
P_{fluct}	Amplitude of chamber pressure fluctuations, %
P_{up}	Upstream pressure
$\mathcal{P}_{ep}$	Pump required power
R	Specific gas constant
Re	Reynolds number
r	Radius
$\dot{r}_f$	Fuel surface regression rate
T	Temperature
$\mathcal{T}$	Thrust
$\mathcal{T}_{av}$	Average thrust
t	wall thickness
t_b	Burn time
T_{vac}	Thrust in a vacuum
U	free-stream air speed
v_e	Nozzle exit velocity
v	vehicle velocity magnitude
w	Particle swarm optimization weight/inertia parameter
x_{cp}	Center of pressure
x_{cg}	Center of gravity
α	Angle of attack
β	Prandtl-Glauert compressibility correction factor
β_T	Longitude
γ	Flight path angle
γ_c	Specific heat ratio of combustion products
γ_{pg}	Specific heat ratio of pressurant gas
ΔH	Change in flight altitude
ΔP_{ep}	Pressure drop across electric pump
ΔP_{inj}	Constant pressure drop across injector
ΔV	Change in velocity
δ_{be}	Battery energy density
δ_{bp}	Battery power density
δ_{nozzle}	Nozzle clearance parameter

ϵ	Roughness height
ζ	Flight Heading angle
η_c	Combustion efficiency
η_{ep}	Electric pump efficiency
ξ	Longitude
ρ	Density
σ	Material stress
τ_b	Normalized burnt time
ϕ	Latitude
χ	Bilinear tangent steering shape constant
ω_E	Angular velocity fo Earth

Subscript	Definition
av	Average
c	Combustion chamber
f	Fuel
H	Height
i	Initial, or instance (depends on context)
ox	Oxidizer
pg	Pressurant gas
ref	Reference
y	Yield

Abbreviation	Definition
BFGS	Broyden–Fletcher–Goldfarb–Shanno algorithm
CEA	Chemical Equilibrium with applications
CFD	Computational fluid dynamics
DOF	Degree of freedom
FEM	Finite element method
GA	Genetic algorithm
HRE	Hybrid rocket engine
HTPB	Hydroxyl-terminated polybutadiene
L-BFGS-B	limited memory, BFGS, bounded algorithm
LOx	Liquid oxygen
LRE	Liquid rocket engine
MEOP	Maximum expected operating pressure
MER	Mass estimating relationship
MDO	Multi-disciplinary design optimization
NPSP	Net positive suction pressure
NPSP,A	Available NPSP
NPSP,R	Required NPSP
PBAN	Polybutadiene acrylonitrile
PMMA	Polymethyl methacrylate

PSO	Particle swarm optimization
SECO	Second engine cut-off
SECO-1	The first instance of SECO
SOSE	Second-order shock expansion
SRM	Solid rocket motor
TVC	Thrust vector control

Chapter 1

Background and Introduction

1.1   Research Overview and Motivation

Hybrid rocket engines (HREs) have the potential to disrupt the launch industry by offering relatively simple mechanical design and lower cost at comparable performance to the existing liquid rocket technology that is prominent in the current launch industry. HREs have the benefit of being inherently safer and mechanically simpler when compared to solid and liquid bi-propellant propulsion systems. Recently, the small-satellite market has grown and many startups are competing to offer economical, dedicated small-satellite launch services. Many developers are pursuing the use of hybrid rocket propulsion. The research outlined in this thesis provides a detailed look at conceptual designs of optimal and minimum-mass configurations of multi-stage hybrid rocket-propelled launch vehicles with different feed systems and propellant combinations. The intent of the designs and research findings is to aid in the development of small-satellite launch vehicles using HREs for low-cost access to space.

1.2 Background

1.2.1 Levels of Development

The different successive levels of design and development for aerospace vehicles include the following (Hammond, 2001):

- Conceptual design
- Preliminary design
- Detailed design
- Manufacturing
- Testing
- Production
- Operations
- Field support

The investigation for this thesis mainly focuses on the conceptual multi-disciplinary design of hybrid rocket vehicles. Conceptual design, at the highest level, includes analysis, evaluation, and configuration initialization (Gage, 1996; Hammond, 2001). In the conceptual phase, the most fundamental theory is implemented in order to quickly evaluate the performance and cost of a design, iterate upon it, and determine its approximate configuration. Preliminary and detailed design follow the same methods as conceptual design but at successively finer levels of detail. The detailed design finalizes the design trades and configuration for production. The detailed design phase usually consists of teams operating in different disciplines communicating interfaces and constraints back and forth. During the detailed design, each team performs successive iterations until each discipline is satisfied that the design meets the requirements.

1.2.2 Multi-disciplinary Design Optimization

Multi-disciplinary design optimization (MDO) can be viewed as a design process that takes into account the mutually interacting phenomena of different disciplines (Martins and Lambe,

2013). The concept of MDO is used to find better performing configurations, which can only be found when considering many disciplines together rather than considering a single discipline at once, at each sequential design step. MDO can lead to a superior optimal, however the process can significantly increase the complexity of the design problem. The design of launch vehicles has historically been broken up into different disciplines (Hammond, 2001); these include but aren't limited to:

- Propulsion
- Structures
- Aerodynamics
- Trajectory, guidance, and navigation
- Control
- Avionics - software & hardware
- Materials
- Manufacturing

The disciplines considered in this thesis consist entirely of the first four: propulsion, structures, aerodynamics, and trajectory guidance and navigation. The chosen disciplines are selected for having the largest influence on the performance and configuration of the launch vehicle (Larson and Wetrz, 1999). Incorporating the control mechanism and system design into the conceptual framework would be the next logical step for adding useful fidelity, but it is beyond the scope of the current investigation.

The concept of multi-disciplinary design optimization has manifested itself as useful advice from designers in the launch industry. Akin's laws of spacecraft design (Akins, 2003) has advice on where design improvements are often found and where errors often occur.

Law 15 (Shea's Law): *"The ability to improve a design occurs primarily at the interfaces. This is also the prime location for screwing it up."*

The process of viewing the entire design at once, leading to globally optimal configurations, may not be as important in some industries, but is important in the transportation industry - especially in the launch industry. In the launch industry, optimization is needed to ensure mission success or product function. Optimization can also produce drastic improvements in build and operation cost between configurations.

1.2.3 Hybrid Rocket Propulsion

Hybrid rocket propulsion is a cross between two mature technologies: solid and liquid rocket propulsion. They sometimes offer improvements and occasionally force design compromises that must be considered, when compared to both. Hybrid rocket engine operation typically involves injection of a liquid or gaseous oxidizer into the central port (or ports) of a solid fuel grain. The central port flow causes the regression of the fuel surface where it is transported into flow and combusts (Sutton and Biblarz, 2001). A schematic of a hybrid rocket propulsion system is shown in Fig. 1.1.

History of Hybrid Rockets

Hybrid rockets have been developed and tested since the 1920s. Despite several arguable advantages over the competing technologies, all commercial orbital launch vehicle ventures based on it have failed so far. Recently, since the mid-90s, interest in hybrid propulsion has begun to rise. The revival in interest is attributed, in part, to the improvements in the
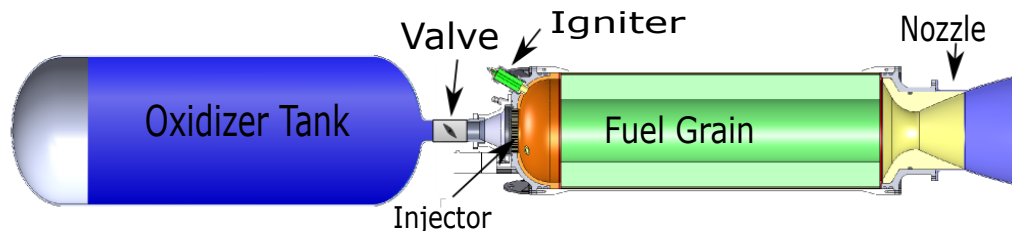
Figure 1.1: Hybrid rocket propulsion system, from Guyver (2017)

regression rates of the fuel with the use of liquefying-fuels (Karabeyoglu et al., 2002). The regression rates are directly tied to mass flow rate and thrust when using a solid fuel grain. The use of liquefying fuels has made simple single-port configurations more feasible, and reduced the required surface area of fuel grains by a significant amount.

The history of hybrid rockets begins in the early 1930's (Altman, 1991; Ribeiro and Junior, 2011). Initially, American and German researchers tested coal as fuel with nitrous oxide and gaseous oxygen as candidate oxidizers. Around the same time, Hermann Oberth, tested tar-wood-saltpeter and liquid oxygen as hybrid rocket propellants. Oberth is known for early fundamental contributions to rocketry. In 1933 Mikhail Tikhonravov and Sergi Korolev flight tested a pressure-fed liquid oxygen and gasoline gel HRE (Ribeiro and Junior, 2011). later, in 1956, General Electric tested a high-density-polyethylene and hydrogen peroxide HRE. In the 1960's NASA tested a hypergolic HRE with impregnated PBAN, and a liquid fluorine and oxygen mix as the oxidizer. In 1968 the United States company Beechcraft developed and tested the Sandpiper target drone which used hybrid rocket propulsion with PMMA/magnesuim fuel and Mon25 (mixed oxides of nitrogen) oxidizer. In 1983 Teledyne later developed a more successful target drone, named Firebolt, that entered the United States Air Force service using PMMA/PB solid fuel and a liquid nitric acid oxidizer. In 1984 the Starstruck Dolphin rocket was tested, which used liquid oxygen / HTPB, with later testing and development by the American Rocket Company (AMROC). In 1998, the use of paraffin was reported at Stanford University as a source of performance improvement. The use of paraffin allowed for a substantial increase in fuel surface regression rate (Karabeyoglu et al., 2002). Other developments were made by Lockheed in the 2000s and finally Scaled Composites and SpaceDev developed the nitrous oxide/HTPB hybrid rocket engine for the sub-orbital vehicle SpaceShipOne whose successor is operating today for Virgin Galactic as part of its suborbital flight program. Very recently, there has been significant interest in the application of HREs for launch and in-space propulsion (Schmierer et al., 2019b). Since the use of HREs can reduce design and mechanical complexity, the technology has

the possibility to disrupt the longstanding thinking of the launch and in-space propulsion industry by potentially offering lower costs of missions. The list of companies, known to this author, competing in the launch or propulsion industry, using hybrid rocket propulsion is listed in Table 1.1, majority of information taken from (Schmierer et al., 2019a).

Name	Country	Business	Fuel	Oxidizer
HyImpulse	Germany	500 kg SSO	Paraffin-based	LOx
TiSpace	Taiwan	350 kg 650 km SSO	HTPB	N_2O
Gilmour Space	Australia	215 kg 500 km SSO	3D-printed fuel	H_2O_2
Reaction Dynamics	Canada	150 kg 500 km SSO	Polymer	H_2O_2[1]
Equatorial Space Ind.	Singapore	30-70 kg LEO	Paraffin-based	LOx
Nammo	Norway	10kg 650 km Polar	HTPB	H_2O_2
Delta V Space Tech.	Turkey	Launch Vehicle	Paraffin-based	LOx[2]
Rocket Crafters	US	Launch Vehicle	3D-printed ABS	N_2O
T4I	Italy	Orbital propulsion	Paraffin-based	H_2O_2
Space Propulsion Group	US	Development, R&D	Paraffin-based	LOx & others
The Spaceship Company	US	Suborbital, manned	Polyamide	N_2O
Space Forest	Poland	Sounding rocket	Paraffin-based	N_2O
Space Link	Slovenia	Sounding rocket	Paraffin-based	LOx

Table 1.1: Start-up & established companies active in the

hybrid rocket propulsion field

---

[1]Not published, speculated based on patent application (Elzein et al., 2020) (Note in Table 1.1)
[2]Not published, speculated based on publications (Gegeoglu et al., 2019) (Note in Table 1.1)

Some of the advantages and disadvantages of hybrid rocket propulsion are organized below:

Advantages

- An intimate mixture of fuel and oxidizer cannot be easily made if the single oxidizer tank was to catastrophically fail. This safer failure mechanism greatly reduces the explosion potential compared to liquid rocket engines (LREs).

- The solid fuel grains are inert at ambient conditions in the absence of an oxidizer, making them safer to manufacture and transport compared to solid propellant rocket motors (SRMs).

- Grain failure (e.g., sloughing) in a hybrid is benign compared to SRMs. In SRMs, grain failure leads to increased burn rate and over-pressurization and catastrophic failure, since burn rate is pressure-dependent (Sutton and Biblarz, 2001).

- HREs can be throttled and terminated mid-burn with the use of a single valve, unlike SRMs.

- Energetic or stability-promoting additives can more easily be introduced to the propellants, compared to LREs. For example, additives like metal particles can be suspended in the solid fuel grain.

- The system complexity can be reduced relative to existing LREs since only the control and injection of one fluid propellant is required.

- The density of fuel is increased, compared to liquid fuels, since it exists in the solid phase.

- The combustion chamber doubles as a "fuel tank". This point can be viewed as either an advantage or disadvantage, depending on the type of feed system (if propellant

storage pressure is above or below combustion chamber pressure).

Disadvantages

- Typically liquid fuels are used in regenerative cooling applications in LREs. The fuels are typically chosen over the oxidizers to avoid oxidation issues. Regenerative cooling cannot be as readily done with a liquid oxidizer in the case of a HRE.

- In HREs, in addition to the chosen oxidizer mass injection rate setting, the effective oxidizer-to-fuel ratio OF is a function of two other things: fuel burning surface area and the local axial mass flux G (which drives the fuel surface regression rate, in a conventional HRE). These two quantities, in general, increase and decrease concurrently during a burn. Generally, their effects are not equal and the oxidizer-to-fuel ratio shifts during a nominal burn (Kuo and Chiaverini, 2007).

- Gimbaling of the entire engine is difficult/impractical compared to relatively small-chambered LREs.

- The HRE technology as a whole is less mature since its use is infrequent, compared to existing technologies (Kuo and Chiaverini, 2007).

Feed systems

Two main feed systems are considered in this thesis: electric pump-fed and pressure-fed. The pressure-fed category is comprised of self-pressurizing and back-fill pressurant-based systems. The self-pressurizing systems rely on two-phase fluids with a relatively high vapour pressure and liquid density at standard conditions (Zimmerman et al., 2013). Self-pressurizing propellants (in this case, oxidizers) maintain pressure upon depletion of liquid oxidizer from the system. Back-fill, or gas pressure-fed systems, use a pressurizing system comprised of a separate high-pressure storage vessel and a regulator (Sutton and Biblarz, 2001). When compared to pump-fed variants, the pressure-fed systems are inherently simpler. Pressure-

fed systems typically have larger inert masses since the tank pressure must be sufficiently higher than the combustion chamber pressure, while pump-fed systems (with pressurization downstream of storage) can have relatively low-pressure storage tanks (Sutton and Biblarz, 2001).

Pump-fed systems have typically used turbine-driven pumps, called turbopumps. In turbopump feed systems, the pump is driven by a turbine fed with a working fluid. Electric pump feed systems have a battery-powered electric motor in place of the classical turbine. The electric pump feed system has been considered since the 1990's for liquid bi-propellant systems and have shown to be as a higher-performing alternative to back-fill pressure-fed configurations for hybrid systems (Casalino et al., 2019b). Advances in battery technologies have made this feed system increasingly competitive (Rachov et al., 2013). Recently, Rocket Lab's Electron launch vehicle completed its 14th flight using Rutherford LREs with an electrically-driven pump feed system (RocketLab, 2020a).

1.3   Research Objectives

One of the research goals of this thesis is to answer the question: to what extent can hybrid rocket launch vehicles be scaled down? Put differently, and generally - what is the minimal size (gross liftoff mass or dry mass) of a two-stage hybrid rocket launch vehicle for a given payload mass, delivered to a low Earth orbit (LEO)? The minimization of dry mass is in general desirable, as the dry mass is assumed to be strongly linked to cost, in dollars. The use of dry mass in the absence of detailed cost data is a commonly used strategy by other researchers (Castellini, 2012; Miranda, 2015).

A follow up research question question is what does the minimal (optimal) configuration look like for different vehicle configurations (feed systems and propellant types)? The goals of this thesis are to answer these research questions, along with creating the framework necessary to attempt to answer them. The framework will be a combination of mathematical

models, simulating the physics of the various disciplines relevant to the performance of a hybrid rocket launch vehicle. The models will be incorporated into an object-oriented computer program, written in Python.

1.4   Methodology

The design space of a hybrid rocket vehicle is divided into the various relevant sub-disciplines. The design variables, for this study, were desired to be limited to the most fundamental defining physical quantities possible. The design variables, seen as inputs or constants, dictate the design of the launch vehicle as it propagates through the various sub-disciplines.

The propulsion system is the first conceptually designed sub-system. Orbital launch vehicles are typically comprised of a large portion of propellant, on a mass basis, which is necessary to fulfill the mission requirements (Larson and Wetrz, 1999). The propulsion system designed dictates: the propellant masses, propellant volumes, propulsive performance, and fuel and converging-diverging nozzle geometries. The vehicle structural configurations are then defined by vehicle elements (oxidizer tank, interstage, etc.), in order to close the design further. Structural and geometric inputs and constants (outer diameter, nosecone, etc.) further constrain the design. The aerodynamic modeling provides the aerodynamic forces, given the vehicle geometry and the simulated environment, resulting in the ability to calculate the vehicle dynamics and loads. The structure is then iteratively sized, based on material yield stress and buckling failure modes using in-flight and on-pad structural loads. The trajectory is converged to the target altitude and speed by altering initial flight path conditions and trajectory control points, while minimizing overall propellant use. The described process results in a single vehicle design solution. Numerous vehicle designs are then evaluated and successive design iterations altered using global optimization techniques dedicated to minimizing dry mass. The minimization of dry mass, for a given mission, results in optimal designs and the corresponding design variables.

Chapter 2

Literature Review

The following literature review surveys work on launch vehicle MDO. Within launch vehicle MDO, the engineering models and the MDO implementation strategies were assessed. Most works have been on large-scale liquid bi-propellant and SRM-based launchers. A relevant work on small-satellite hybrid launchers was found and reviewed. Work on small-satellite launch vehicle design, based on SRM and liquid bi-propellant technology, was investigated. Finally, there were several works found on hybrid rocket conceptual design that mainly focused on the optimization of the propulsion system quantities but avoided other disciplines.

2.1   Launch Vehicle MDO

The MDO of launch vehicles has been a topic of research for several years. The majority of studies investigated here focus on liquid bi-propellant and solid rocket-propelled expendable launchers. The studies surveyed on launch vehicle MDO have been decomposed into the MDO formulation and the engineering models. The engineering models are naturally divided into their respective disciplines (propulsion, aerodynamics, etc.).

2.1.1 Liquid Bi-propellant and Solid Rocket MDO

The work of Bayley (2007) was one of the earliest works on launch vehicle MDO. Bayley included the use of a genetic algorithm (GA) to optimize Earth-to-orbit SRM and LRE-based multi-stage rockets. The objective of the work was to minimize gross-take-off weight for a given mission. The propulsion modeling consisted of non-time-varying parameters: chamber pressure, and characteristic velocity, but incorporated varying thrust with changing back pressure. The structural elements were defined with user inputs rather than physics-based or even historical-based empirical methods. A closed-source missile aerodynamics design software was used to query aerodynamic coefficients for use with a six degree of freedom (6DOF) flight dynamics simulation. Despite that lack of physics-based formulation for the structural design, the validation study seemed to show agreement with existing rocket designs. The results showed that increasing scale increased a vehicle's payload mass fraction.

In contrast to maximizing payload fraction (or minimizing mass for a given payload), research was done towards estimating the cost and reliability of launch vehicles during the conceptual design phase (Krevor, 2007). Krevor's work included an optimization (maximizing reliability with minimal cost) using a GA. The vehicle mass was estimated using historical data from previous launch vehicle designs, which exist as empirical relations, commonly used and refereed to as mass estimating relationships (MERs). The propulsion system parameters were estimated using a tool called the Rocket Engine Design Tool for Optimal Performance - 2 (REDTOP-2) (Bradford et al., 2004). The REDTOP-2 tool returned thrust-to-weight ratios of the engine and specific impulse, given the defining input parameters: fuel type, oxidizer type, chamber pressure, and expansion ratio. The trajectory analysis in this methodology was completed using the Program to Optimize Simulated Trajectories (POST) (Brauer, 1975), which is a 3DOF trajectory simulation widely used at NASA. The work's contribution was mainly in the area of predicting and maximizing reliability while minimizing cost, and used existing modules to carry out the vehicle design aspect.

Engineering Model Advancements

The engineering discipline modeling fidelity used in launch vehicle MDO was greatly improved by the work of Castellini (Castellini, 2012; Castellini et al., 2014). Castellini's PhD dissertation described a MDO with a focus on the engineering formulation of launch vehicle conceptual design. The thesis reviewed many pieces of work, to its date, on MDO for aerospace vehicle design. The review of MDO presents the classifications advanced by Cramer et al. (1992). The work by Cramer et al. (1992) includes the Multi-disciplinary Feasible (MDF) and Individual Disciplines Feasible (IDF) formulations. A MDF framework is the most intuitive since the design is, at all iterations, feasible, such as moving a design from inputs through various departments (disciplines) to output. However, MDF, at some times, can waste computational resources on ensuring a feasible design during each iteration. The IDF framework introduces feasibility constraints at each interdisciplinary stage but the global optimizer drives the individual disciplines towards feasibility only at the end of the optimization process. IDF adds a constraint and parameter per interdisciplinary coupling, but in some situations can reduce the number of total design iterations. An analysis conducted by Castellini shows that MDF proved superior to IDF in launch vehicle design. Castellini had short iteration times but if loop time was increased, maybe with the use of high-computation-cost CFD or FEM, the extra effort in formulating the IDF framework could have proved worthwhile. Castellini presented the use of particle swarm optimization (PSO) and GA as the most promising global optimization schemes for launch vehicle design, suggesting the superiority of PSO's performance given the evidence in literature. Castellini found that PSO outperformed the GA in terms of convergence rate and consistency of finding the global optimal, and used it to generate all results.

The launch vehicle conceptual design models, which were the main focus of Castellini's work, were divided into two sections named conceptual and early-preliminary. The early-preliminary section was the result of feedback from an initial validation study and meetings with the European Space Agency's (ESA)'s engineers and specialists about the initial con-

ceptual framework. The overall vehicle structures included serial and or parallel staging of LRE and or SRM rocket boosters. The propulsion system design could either be defined based on existing engines (off-the-shelf database), or on fundamental SRM or LRE propulsion theory. The performance of new designs, of a chosen propellant combination, was predicted using NASA Chemical Equilibrium with Applications (CEA) (Sanford and Mcbride, 1994) for given mixture ratios and combustion pressure. The CEA outputs were used, assuming isentropic expansion, to determine theoretical specific impulse and nozzle geometry. Detailed combustion and nozzle efficiencies were applied based on combustion and nozzle design parameters. It was noted that certain efficiencies must be introduced to generate performance values that resemble operational engine's data, as the vehicle performance (payload mass for a mission) had the highest sensitivity to the propulsive performance. The nozzle and combustion efficiencies account for the divergence angle of the nozzle exit flow, boundary layer losses, finite combustion area, and real gas properties. All non-structural mass components were determined from MERs. The structural components were sized using structural material stress-based methods outlined for combined axial, bending, and pressure loads with thin-cylinder buckling for compression. Missile Datcom (Blake, 1998) was used for the aerodynamic parameters for the ogive-cylinder geometry used. The conceptual framework allowed diameter changes as well as side boosters, the latter of which could not be handled by Datcom. A simple averaging scheme was proposed and used for the additional drag and normal force from side boosters, which was used with a single validation point and with the admittance of probable inaccuracy. The choice of the aerodynamic modeling was defended by showing low sensitivity of the vehicle performance (payload mass for a mission) to uncertainty in drag. The flight simulation was modeled assuming a point mass in a 6DOF spherical-Earth coordinate system. The trajectory consisted of a pitch over after launch into an optimizible gravity turn, bi-linear tangent steering program, and upper stage coast and circularization burn. Castellini included cost, reliability and safety into the conceptual study by using cost estimating relationships and component failure probabilities based on histor-

ical data. After two successive validation runs comparing the code to the Ariane 5 ECA and VEGA launchers, Castellini concluded that predicted inert mass error was the largest contributor to the variance in deliverable payload mass (5%). The predicted error in propulsion system performance lead to a 3% difference in payload mass, and aerodynamic drag and normal force error lead to 2% difference in payload mass. The final, revised, conceptual methodology: called early preliminary was concluded to predict payload masses within 4 % and 6% for the Ariane 5 ECA and VEGA launchers, concluding that it is possible to develop relatively simple models permitting fast MDO cycles while still ensuring sufficient accuracy to place confidence in the achieved design solutions for expendable launch vehicles.

Mota (2015) used many of the engineering models used by Castellini. Mota's main contribution was in introducing a novel formulation to optimize trajectories by mixing a direct method and indirect method. The direct method used typical control point adjustment while drag effects were present in the atmosphere. Outside of the atmosphere, where drag could be neglected, the initial co-state variables for optimal thrust arcs in vacuum could were calculated in the indirect method. The method supplies optimal thrust arcs for the upper stages but still requires converging to the desired orbit and optimization using a non-linear algorithm.

The expendable launch vehicle MDO knowledge base was expanded by introducing first stage re-use modeling (Woodward, 2017). Woodward developed a tool for expendable and first-stage-boost-back reusable launch vehicle conceptual design. The work started with a comprehensive review on the state of the art of conceptual design and optimization of launch vehicles from both commercial and academic sources. In the conceptual design methodology, the propulsion system was characterized by constant specific impulse. MERs were used for the entire vehicle design, with no stress-based sizing. The trajectory was optimized using pitch rate parameters defined at instants into the burn as optimization variables coupled with a gravity turn and maximum dynamic pressure constraints. The flight simulation was conducted using a 3DOF round-Earth formulation which simulated initial flight and boost-

back. The aerodynamic coefficients were determined using missile aerodynamic empirical relations from Fleeman (2012). Woodward chose to keep track of the performance parameter ΔV, calculated using the Tsiolkovsky rocket equation (Moore, 1813) from specific impulse and mass fractions of the vehicles. The ΔV is the change in velocity of a launch vehicle and is a a measure of impulse per unit mass needed to perform a maneuver including launching to orbit. The net required ΔV budget was calculated incorporating drag, gravity, and steering losses which were quantified from the flight simulation. Their study was validated by comparing to existing rockets, which included: Gemini Launch vehicle (Titan II), Saturn V, and Falcon 9. It was estimated that the delta V losses that were predicted had an error on the order of 10%.

MDO Implementation

The MDO formulation, instead of the engineering modeling, was the main focus of other work (Balesdent, 2011). Balesdent wrote a very comprehensive and formal mathematical definition and review of MDO theory. Balesdent suggested that putting trajectory at the center of the optimization and having stage-wise optimization with defined coupling parameters would yield global optimal results efficiently. The entire problem was formulated as IDF and coupling parameters were defined between structures, propulsion, aerodynamics, and trajectory. The propulsion system modeling of Balesdent's work was a constant property system with constant chamber pressure and mass flow rates but altitude (back pressure) compensated. The aerodynamic drag was considered solely a function of Mach number, appearing un-cited. The trajectory was modeled as a piece-wise linear function of pitch angle vs time into flight, with optimization control points. A three-degree-of-freedom non-rotating spherical-Earth formulation was used for the flight simulation. The mass estimates for all vehicle structures and components were accomplished using MERs. The pressure vessel mass sizing was stress-based. The work appears to be very detailed in the MOD review and IDF formulation, however it does not contribute greatly to the launch vehicle design knowledge

base in the conceptual design of launch vehicles, and calls upon very basic functions.

2.1.2 Hybrid Rocket MDO

Miranda (2015), was found to be the only researcher who presented a comprehensive MDO for hybrid launch vehicles. Miranda conducted conceptual optimization studies on air-launched and ground-launched hybrid rockets. The optimization objective function included vehicle gross-take-off mass. Miranda's research question was: how do hybrid rocket vehicles (both ground and air-launched) compare to existing SRM technology in terms of cost and performance? Miranda, in short, found they had similar performance. Hybrid rocket vehicles had lower propellant mass fractions but higher specific impulse, compared to SRMs. Miranda built off the work of Van Kesteren (2013) on solid rocket conceptual design. Miranda's methodology included hybrid empirical regression rate law and used NASA CEA to predict combustion properties. The combustion products were expanded assuming frozen flow through the nozzle and isentropic relations. The formulation did not account for any time-varying aspects of hybrid propulsion such as the oxidizer-to-fuel ratio (OF) shift, however its absence was acknowledged and mentioned in the future work section. Oxidizer and combustion chamber tanks and cylindrical sections were sized using stress-based methods from axial and bending loads in-flight, while all other components used MERs. Missile Datcom was used for the aerodynamic coefficients. A 3DOF round-Earth model was used for simulating trajectories to orbit. The global optimization techniques used were GA and PSO. Miranda found that PSO out-performed the GA used. Miranda concluded the model was valid when comparing to data available from the NAMMO hybrid rocket (Faenza et al., 2019). The data of the NAMMO launcher was however redacted from the thesis. The work also showed that the vehicle can weigh substantially less (up to 75%) when air launching is used. The work found the minimized gross-take-off mass for a ground-launched 10 kg to 780 km circular LEO three-stage sorbitol/N$_2$O hybrid launch vehicle to be 1710 kg. The work concluded that hybrid rocket vehicles can have equal or greater performance than solid-rocket-based propul-

sion, since HREs offer theoretical higher performance but currently have lower propellant mass fractions. Future work suggestions also included adding OF and throttling parameters as optimization variables and using faster computing code with parallel computing for optimization studies. Miranda also suggested incorporating fluid equations of states and higher fidelity propulsion modules for further detailed preliminary design studies and optimization.

The work of Miranda shares many similarities in modeling methodology with the work in this thesis. Miranda's thesis also produced designs. Much of the suggested future work by Miranda was addressed in this work. The recommendations of Miranda and the suggested work are combined in the following:

- Implement the constraints of the solution-space directly into the optimizer.
- Use parallel computing and computational resources greater than a common desktop.
- Conduct a more extensive review of existing hybrid rocket technology.
- Explore more fuel and oxidizer combinations.
- Explore different oxidizer storage conditions.
- Include propellant oxidizer-to-fuel ratio and oxidizer flow rate as optimization variables.
- Prioritize fast computation in all code.

On top of the suggestions by Miranda, there were also many changes and refinement to the modeling methodology that took place that resulted in different findings of optimal and feasible configurations.

2.2   Hybrid Rocket Propulsion Design and Optimization

Initial hybrid rocket conceptual design was accomplished by analyzing the replacement of LRE and SRM upper-stages with hybrid alternatives. Casalino and Pastrone (2010a) investigated the optimization of a hybrid rocket upper stage to replace a SRM and LRE 3rd and 4th stage. The trajectory and motor parameters of a polyethylene and hydrogen peroxide motor were considered in a conceptual design optimization. Optimization parameters for

the motor included: number of ports, fuel geometry, initial thrust, chamber pressure, length, and nozzle area ratio. The ideal OF was found to differ from that corresponding to the highest specific impulse. It was found that a single pressure-fed hybrid stage could replace the third and fourth SRM and LRE stages for a four stage rocket with a mission profile based on the Vega launcher. Karabeyoglu et al. (2011) expanded the hybrid propulsion conceptual design literature by analyzing a pressure-fed hybrid for the replacement of an existing upper stage. The investigated propulsion systems were based on paraffin and liquid oxygen and were compared to existing all-SRM and all-LRE technologies. A single-port fuel configuration was used with hoop stress and Mach number constraints on the initial port diameter. Karabeyoglu et al. (2011) found that a pressure-fed upper stage had an advantage over a SRM upper stage due to its higher specific impulse. A 25% increase in payload mass was possible when using neat paraffin with liquid oxygen over the Orion 38 solid rocket motor upper stage. It was also found up to 40% payload increase was theoretically possible when using high-density performance additives. Karabeyoglu et al. concluded with a list of key technology developments needed for the advancement of HREs:

- Retaining high efficiencies and good stability for long duration burns
- Controlling/limiting the nozzle erosion rates
- Nozzle development
- Vacuum ignition and multiple ignitions
- Throttling
- Thrust augmentation for control: LITVC or GITVC capability

Casalino and Pastrone (2010b) added to their previous work by incorporating an electric pump feed system to HREs that would improve payload capability over the pressure-fed configuration. After the uptake of the electric pump feed cycle, Casalino et al. (2019b) wrote on the viability of using electric pump feed systems and produced more detailed quantitative analysis compared to his previous publications. In the recent work of Casalino et al. (2019b), three different feed systems were considered for a paraffin/ liquid oxygen hybrid rocket upper stage for a Vega-like launcher. The three propulsion systems were gas pressure-fed, electric

pump-fed, and advanced electric pump-fed. The trajectory error was minimized and payload mass concurrently maximized using a PSO. Six optimization parameters were used to define the design, the first five were: the grain outer radius, the web thickness, the fuel grain length, the final exhausted oxidizer mass, and the initial nozzle area ratio. The sixth parameter was the exhausted oxidizer mass for pressure-fed or pump discharge pressure for the pump-fed case. The increased payload mass over the pressure-fed case was found to be 12% and 18% for the electric pump and advanced electric pump versions respectively.

Casalino et al. (2019a) recently contributed to the area of small-satellite hybrid launcher conceptual design with a design and optimization of a three-stage pressure-fed hybrid small-satellite launcher. The launcher was based on a paraffin/liquid oxygen engine. The number of engines in each stage were six, three, and one for the stages, from first to last, respectively. The gross takeoff mass was set at 5000 kg while the payload mass was maximized. The optimization variables included: fuel grain outer radius, OF, pressurant gas volume, and overall oxidizer mass exhausted. The trajectory was optimized in an inner-loop for each motor configuration. The five motor parameters were simultaneously converged to their optimal values using a PSO to maximize payload mass. The design robustness was evaluated by incorporation deviations in the motor parameters (regression constants). The conservative estimate where each engine operated at the worst off-nominal conditions resulted in a 15 kg, or 26% payload reduction.

2.3   Small Launch Vehicle Design

Articles on the topic of small-payload orbital launch vehicles were reviewed. Whitehead (2005) asked the question: how small can a launch vehicle be? The author analyzed the ascent trajectory and drag effects on SRM and LRE-based rockets at different scales. Whitehead found that the effect of drag on smaller launch vehicles was relatively larger and resulted in higher required ΔV to attain the same orbit. The higher influence of drag on performance

was mitigated by steeper simulated launch trajectories, where the rocket spends less time in the atmosphere, but this also comes at a cost of higher ΔV due to larger circulation burns. It was concluded that scaling down does not impose a physical limit on launch vehicle size from the ascent and trajectory standpoint but increases required ΔV slightly. Whitehead states the technological challenge is obtaining high propellant mass fractions on such small launch vehicles, namely when components must be impractically small.

Greatrix and Karpynczyk (2005) presented a more detailed vehicle design concept for a relatively low-cost small-payload delivery to orbit. They presented two designs of a three-stage solid rocket configuration, one for air-launch and one for ground-launch. The payload was in the nano-satellite range of 10 kg. The target orbit was approximately 320 km orbit launching eastward in the proximity of Churchill Manitoba. A significant coast was used between 2nd stage burnout and 3rd stage re-light in order to coast to target altitude before conducting a ciruculization burn. The trajectories incorporated a steep ascent until outside of the atmosphere followed by aggressive turning accomplished by side thrusters. The motion was modeled using a 6DOF round earth formulation with aerodynamics from Missile Datcom. The reduced drag and ΔV requirements from air launching resulted in a vehicle gross mass of 1900 kg, versus 4500 kg for the ground launch case. The concluding remarks suggest addressed the use of HREs for low cost access to space citing the high specific impulse and availability of propellants compared to SRMs.

2.4   Summary and Areas of Improvement

The literature relating to launch vehicle MDO has mainly been comprised of large-scale liquid bi-propellant and SRM expendable launchers optimized based on paylaod fraction. Building on payload fraction optimizations, cost and reliability have been modeled and implemented into the MDO process. Later researchers worked to review, refine, and add fidelity to the engineering models to generate detailed results. Parallel to the engineering model refinement,

some researchers focused on the MDO process and proposed and used different strategies with less contributions to the engineering models. Recent work incorporated re-usability into the launch vehicle conceptual design process. MDO has been shown to be a powerful tool is producing high-performing launch vehicles. However, many of the empirical mass estimating relations used for large-scale vehicles are not effective for small-scale vehicle design. As such, there have been many recent works devoted to conceptual design at the smaller scale. Given the reviewed literature, the smallest conceptual launchers investigated have been in the range of 10 kg payload capability. The only identified drawbacks of very small launchers have been an increased influence of drag and impracticality of miniature hardware. Much of the work on hybrid rocket conceptual design and optimization has focused on the propulsion system specifically, without significant detail given to other disciplines.

Contributions can be made by expanding the current hybrid rocket full-vehicle MDO knowledge, especially with the recent propulsion system modeling using paraffin fuel and the electric pump feed system. The identified area of improvement in hybrid rocket launch vehicle MDO literature, coupled with the recent increase in small-satellite launcher design and development, offer the motivation for the present work. The present conceptual design framework will aim to use physics-based modeling given the lack of historical data and empirical mass models for small launchers.

Chapter 3

Mathematical Modeling

The change in velocity (ΔV) of a launch vehicle or spacecraft is a measure of the impulse per unit mass needed to perform a maneuver such as launching to orbit or an in-space orbital maneuver (Vallado, 2010). The ΔV of a launch vehicle can be determined using the Tsiolkovsky rocket equation:

$$\Delta V = v_e ln \frac{m_0}{m_f} = I_{sp} g_0 ln \frac{m_0}{m_f} \tag{3.1}$$

Where v_e is the nozzle exit velocity, I_{sp} is the specific impulse , and g_0 is Earth's standard gravitational acceleration. The values m_0 and m_f are the vehicle initial and final masses respectively. The derivation of the rocket equation can be first found by Moore (1813). The equation is derived by applying conservation of momentum on a one-dimensional vehicle with aligned thrust and velocity vectors. The derivation assumes an impulsive thrust and constant exhaust velocity. The derivation of the rocket equation neglects aerodynamic drag and gravity, and more subtly neglects steering losses, which arise whenever the direction of the thrust vector differs from that of the vehicle's forward velocity vector. Under the array of assumptions, mentioned above, the ΔV is remarkably only dependent on the propulsive performance (specific impulse , I_{sp}) and structural efficiency (mass ratio, $\frac{m_0}{m_f}$). It is evident from this relation that one should strive to minimize inert (dry) mass of a launch vehicle

while maximizing its propulsive performance in order to maximize overall performance. The impulsive thrust profile used in the derivation is a useful starting reference point, but losses related to steering, gravity, etc., will need to be accounted for at some point, and hopefully minimized in conjunction. However, one can note that in working towards the minimization of the gravity losses, the thrust becomes large, and leads to large maximum aerodynamic and thrust loads and stresses. All methods of minimizing gravity losses lead to large drag losses and large structural loads that require more structure mass for a given material's strength-to-weight ratio. Considering the extremes at all ends, there exists an optimal configuration trading off drag losses, gravity losses, and even propulsive performance, with additional structure mass. The optimal configuration requires a more detailed design of the launch vehicle to be formulated.

The flight trajectory of the vehicle is another aspect of launch that should be considered when the mission requires more than a maximum speed or altitude, such as obtaining orbit. The trajectory planning incorporates the trade-off between horizontal (tangential to the Earth's surface) or vertical profiles (normal to the Earth's surface) for a specific mission. More vertical approaches leave the atmosphere sooner and incur less drag losses but require larger magnitude circularization burns in preparation for entering a circular orbit at the required orbital speed. Loads due to the incurred angle of attack from pitching, lateral thrust forces, and steering losses, are also considered during the trajectory design stage. Finally the mass/total impulse distribution between stages is an optimization parameter with feasibility constraints.

In the design of a launch vehicle, the nozzle exhaust velocity, mass ratio, drag losses, gravity losses, steering losses, and trajectory are all coupled and exist as complicated functions of design inputs. To arrive at an optimal launch vehicle configuration for a mission with constraints, more assumptions must be made and details added to arrive at a design. In this investigation, optimal configurations will be found from an iterative conceptual design process using global optimization schemes, since the design spaces are highly coupled.

During the modeling formulation, inputs are selected that define physical quantities. Any parameter that is referred to in this methodology section may be seen as a constant or an optimization variable; the distinction will be made later.

3.1 Propulsion System Modeling

In this section, the propellant masses, solid grain fuel geometry, nozzle geometry, and component masses associated with a given feed system and propellant configuration are defined.

3.1.1 Initial Scaling Parameters and Propellant Attributes

The initial parameters specified are the rocket engine(s) nominal average thrust, $\mathcal{T}_{av}$, and total impulse, I_t. The burn time, t_b, can be equivalently used to replace either the thrust or total impulse parameters. The burn time is simply related to the other initial quantities by Eqn. 3.2:

$$t_b = \frac{I_t}{\mathcal{T}_{av}} \tag{3.2}$$

Since the total impulse and thrust are dependent on back pressure (outside ambient air pressure, which decreases with increasing altitude) for fixed geometry nozzles, the parameters are more accurately defined as liftoff thrust and sea-level total impulse. The sea-level definitions are generalized, with staging in mind, for any altitude, and are defined as thrust and total impulse - at ignition conditions.

The propellant combinations used in this thesis include paraffin wax with either liquid oxygen (LOx) or nitrous oxide (N_2O). The commonly used, axial-length-averaged fuel surface regression parameters of the fuel/oxidizer combinations investigated here, were found in literature (Karabeyoglu et al., 2007; Paccagnella et al., 2019). The relevant regression rate coefficients are presented in Table 3.1. The a parameters are for regression rates in m/s rates for flux values with units of $\frac{\text{kg}}{\text{m}^2\text{s}}$.

Fuel parameter (units)	Value
Regression constant - a - with oxygen	0.117E-3
Regression exponent - n - with oxygen	0.62
Regression constant - a - with nitrous oxide	0.155E-3
Regression exponent - n - with nitrous oxide	0.5
Chemical formula	$C_{73}H_{124}$
Heat of formation, (kJ/mol)	-1860600.0
Mass density (kg/m^3)	900

Table 3.1: Paraffin fuel attributes

The oxidizer and pressurant gas equilibrium thermodynamic fluid properties are found by use of equations of state accessed using the open source CoolProp package (Bell et al., 2014). The oxidizer properties are determined assuming a saturated liquid at a given temperature. The pressurant gas intensive properties are found by the two state variables; temperature and pressure. The relevant saturated properties: vapour pressure and liquid densities as a function of equilibrium temperature are presented in Figures 3.1 and 3.2 respectively. Nitrous oxide is used as a self-pressurizing oxidizer due to its high vapour pressure at ambient temperatures as shown in Fig. 3.1. The liquid density of the saturated fluid is also reasonably large at ambient temperature and subtitle for flight vehicles. The liquid density is comparable to LOx at relatively higher temperatures.

For the feed systems considered, the combustion chamber pressure (P_c) has to be below the feed system outlet pressure (P_{up}), by a margin. The margin is dictated by a flow devices (injectors) that stop the propagation of pressure fluctuations from the combustion chamber to the propellant tanks for pressure-fed systems, or to the pump outlet for pump-fed variants. The isolation of flow stops any feedback that can lead to feed-system-coupled combustion instabilities or catastrophic reverse flow (Huzel and Huang, 1992). During the conceptual design phase, a constant pressure drop (ΔP_{inj}) is assumed as the defining variable of the injector design. The oxidizer mass flow rate is assumed constant in this investigation and makes the constant pressure drop assumption more valid. The detailed design of the injector is concerned with the exact mechanism of isolating pressure fluctuations while the discour-
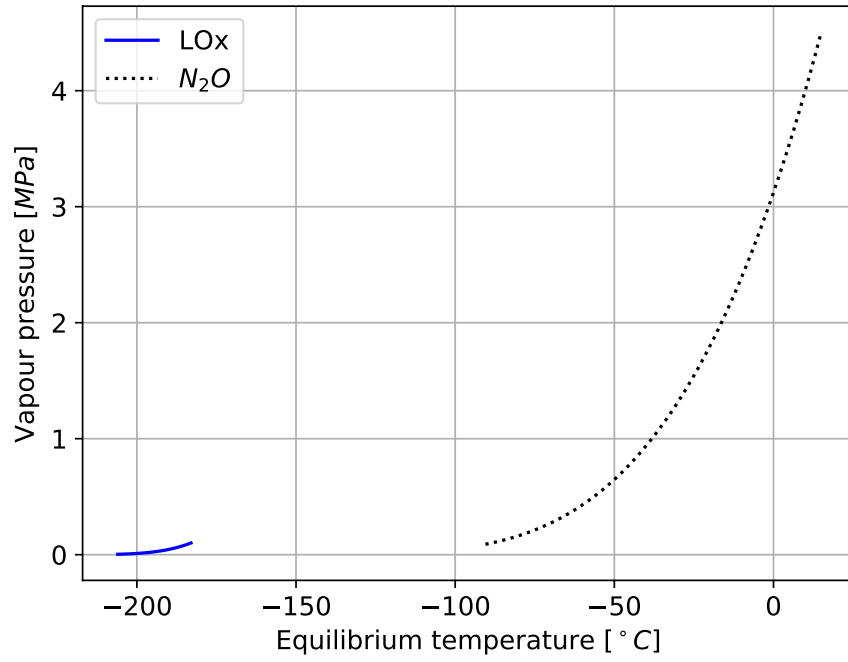
Figure 3.1: Oxygen and N$_2$O vapour pressure vs equilibrium temperature
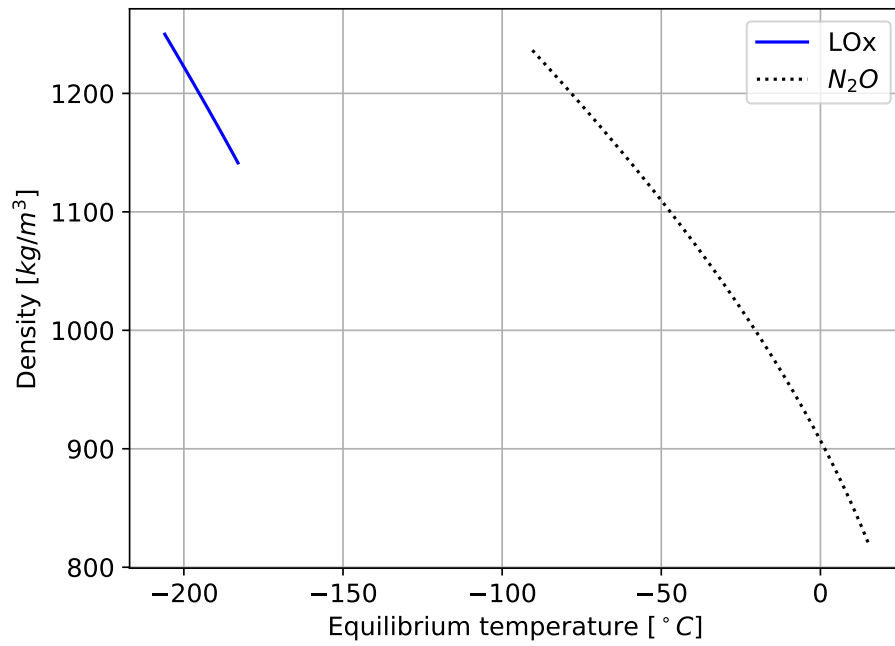
Figure 3.2: LOx and liquid N$_2$O density vs equilibrium temperature

aging of backflow, while, from the system point of view, must minimize pressure drop for a given flow rate. The injector must also promote effective spray, atomization, mixing, and stability for the combustion reaction.

The maximum operating combustion chamber pressure will be defined from the upstream pressure, pressure drop across the injector, and the pressure fluctuations (%) from the mean (P_{fluct}) (Eqn. 3.3). The chamber pressure fluctuation percent deviation from the mean will be 5 %, which is within range of stable combustion (Sutton and Biblarz, 2001). For pressure-fed systems, the upstream pressure is the oxidizer tank pressure, for this investigation. For pump-fed engines, the upstream pressure is the pump discharge, for this investigation. The chamber pressure, P_c, is constrained to the inequality of Eqn. 3.3. The injector pressure drop is desired to be minimized such that feed system pressures are the lowest for a given chamber pressure, and thus reduce inert mass. Constraints on injector pressure drop from LRE injector design were found in (Humble et al., 1995) and presented in Eqn. 3.4. The optimal design occurs when the mentioned inequality constraints are an equality, and the chamber pressure can be completely defined as a fraction of the upstream pressure.

$$P_c \leq \frac{P_{up} - \Delta P_{inj}}{1 + P_{fluct}/100\%} \tag{3.3}$$

$$\Delta P_{inj} \geq 0.5 P_c \tag{3.4}$$

The average oxidizer-to-fuel-ratio (OF_{av}) is defined as the ratio of oxidizer mass flow to fuel mass flow, averaged over the duration of the burn. As noted previously, the OF_{av} may not represent the instantaneous oxidizer-to-fuel-ratio (OF) as hybrid rockets can experience OF shifts caused by their passive fuel addition mechanism. The hybrid OF shift phenomena will be discussed in later sections.

NASA Chemical Equilibrium with applications (CEA) (Sanford and Mcbride, 1994) computer code provides the fuel-oxidizer equilibrium combustion reaction properties in the com-

bustion chamber and nozzle. The properties are used to predict specific impulse and thrust. The reaction is modeled as a constant-enthalpy-pressure (hp) process. Paraffin is modeled as the initial compound $C_{73}H_{124}$ with a heat of formation of -1,860,600 kJ/mol and reacted with either LOx or N_2O. The calculation inputs are reaction oxidizer-to-fuel ratio on a mass basis (OF), combustion pressure (P_c), and nozzle area ratio ($\frac{A_e}{A_t}$).

NASA CEA is used to calculate the ratio of specific heats of combustion products (γ_c), specific impulse (I_{sp}), and the characteristic velocity (c^*). The characteristic velocity is defined by Eqn. 3.5. The characteristic velocity, in the present modeling, is adjusted by multiplying the theoretical characteristic velocity by a combustion efficiency parameter as indicated in Eqn. 3.6.

$$c^* \equiv \frac{P_c A_t}{\dot{m}_{total}} \tag{3.5}$$

$$c^* = c^*_{ideal} \eta_c \tag{3.6}$$

It is worth noting that characteristic velocity can be expressed as a function of combustion temperature (T_c) along with combustion gas properties (specific gas constant: R_g and specific heat ratio: γ_c) Sutton and Biblarz (2001):

$$c^* = \sqrt{\frac{R_g T_c}{\gamma(\frac{2}{\gamma+1})^{\frac{\gamma+1}{\gamma-1}}}} \tag{3.7}$$

However, the formulation in this investigation will use specifically combustion pressure as an input when specifying propulsion system attributes. Equation 3.7 are equal 3.5 assuming the combustion gas is calorically perfect.

The nozzle exit pressure variable (P_e) is constrained by the Summerfield criteria (Eqn. 3.8; see (Stark, 2005)), to avoid flow separation during over-expansion:

$$P_e > 0.4P_{amb} \tag{3.8}$$

Four different methods of calculating the relevant propulsion system quantities are explored in this study. The first method, Method 1, uses only the equilibrium reaction properties in the combustion chamber. Method 1 assumes constant stagnation enthalpy, constant specific heat ratio (calorically perfect), and constant entropy in the nozzle expansion to predict theoretical properties. All the remaining methods do not use the calorically perfect gas assumption, but continue to use the isentropic assumption in the nozzle flow. Method 2 assumes that the chemical reaction is frozen in the combustion chamber, similar to Method 1, but the expanded gas is calorically imperfect. Method 3 is an extension, where the reaction is allowed to equilibrate and the reaction is frozen at the nozzle throat. Method 4 is allowed to equilibrate along the entire length of the nozzle. Method 4 is referred to as shifting equilibrium by other researchers (Castellini, 2012).

Each method's implementation will be assessed. The methods are re-listed below:

1. Calorically perfect, frozen in the chamber
2. Calorically imperfect, frozen in the chamber
3. Calorically imperfect, frozen at the nozzle throat
4. Calorically imperfect, shifting equilibrium

Method 1: Calorically Perfect Gas

Method 1, using calorically perfect gas, was found to be commonly used in the literature surveyed (Miranda, 2015; Casalino et al., 2019a). The prevalence of Method 1 is attributed to its relative simplicity, as the other methods require the nozzle area ratio as an input. This method first assumes that the specific heat ratio of combustion products is constant between inefficient combustion and efficient combustion. After assuming constant specific heat ratio and stagnation temperature, the thrust coefficient and area ratio for the design

30

are determined from Eqn. 3.9 and 3.10 respectively (Sutton and Biblarz, 2001):

$$C_T = \sqrt{\frac{2\gamma_c^2}{\gamma_c - 1}\left(\frac{2}{\gamma_c + 1}\right)^{(\gamma_c+1)/(\gamma_c-1)}\left[1 - \left(\frac{P_e}{P_c}\right)^{(\gamma_c-1)/\gamma_c}\right]} + \frac{P_e - P_{amb}}{P_c}\frac{A_e}{A_t} \tag{3.9}$$

$$\frac{A_t}{A_e} = \left(\frac{\gamma_c + 1}{2}\right)^{1/(\gamma_c-1)}\left(\frac{P_e}{P_c}\right)^{1/\gamma_c}\sqrt{\frac{\gamma_c + 1}{\gamma_c - 1}\left[1 - \left(\frac{P_e}{P_c}\right)^{(\gamma_c-1)/\gamma_c}\right]} \tag{3.10}$$

The variable P_{amb} is the ambient outside air pressure.

The thrust coefficient is used to determine the required nozzle throat area by Eqn. 3.11, given the thrust at ignition conditions ($\mathcal{T}_{av}$) input variable. The combustion products' characteristic velocity, defined in Eqn. 3.5, and ratio of specific heats (γ_c), are found using CEA (Eqn. 3.12).

$$A_t = \frac{\mathcal{T}_{av}}{C_T P_c} \tag{3.11}$$

$$c_{ideal}^*, \gamma_c = f(OF, P_c, fuelType, oxidizerType) \tag{3.12}$$

Method 2, 3, and 4: Calorically Imperfect Gas

The subsequent methods use NASA CEA's ability to calculate the change in relevant properties (stagnation enthalpy, specific heat ratio) through the nozzle and more accurately predict propulsive performance. The methodology using calorically imperfect gas is important as the performance of a launch vehicle is highly sensitive to propulsive performance (Castellini, 2012). NASA CEA can be used to return ideal vacuum specific impulse ($I_{sp,vac,ideal}$) and ideal characteristic velocity (c_{ideal}^*) (Eqn. 3.13). In contrast to Method 1, the nozzle expansion area ratio ($\frac{A_e}{A_t}$) is required.

$$I_{sp,vac,ideal}, c_{ideal}^*, P_e = f(OF, P_c, \frac{A_e}{A_t}, fuelType, oxidizerType) \qquad (3.13)$$

Since CEA is only capable of returning the ideal vacuum specific impulse or perfectly expanded specific impulse, the ambient specific impulse must be extracted. The relation of specific impulse to characteristic velocity and thrust coefficient are presented in equation 3.14. The value of reference gravity (g_0) used in this investigation is the value used by the CEA code: 9.806635 m/s^2.

$$I_{sp} = \frac{C_T c^*}{g_0} \qquad (3.14)$$

The thrust coefficient (Eqn. 3.9) can be viewed as the addition of terms relating to the momentum and external force (pressure). The change in pressure thrust is accounted for by subtracting the thrust due to adverse pressure difference resulting from back pressure:

$$I_{sp,ambient} = \eta_c \left(I_{sp,vac,ideal} - \frac{c_{ideal}^*}{g_0} \frac{P_{amb}}{P_c} \frac{A_e}{A_t} \right) \qquad (3.15)$$

The current thrust at altitude is calculated at each required time increment from Eqn. 3.16:

$$\mathcal{T} = \dot{m}_{total} I_{sp,ambient} g_0 \qquad (3.16)$$

Propulsion Methodology Comparison

A comparison is made between the four methods discussed in order to select one for the complete formulation. For all the cases, the reaction of paraffin and LOx was modeled in CEA at 2.4 MPa with a constant OF of 2.2 for different area ratios. The chamber pressure of 2.4 MPa was chosen for initial investigation as it is similar the value used in another work detailing the development of a sounding rocket (Messinger et al., 2019). The OF ratio was selected to maximize the specific impulse for this propellant combination. The results are presented in Fig. 3.3. All methods are in agreement for low values of nozzle

area ratio. Method 1 predicts relatively high performance for high area ratio nozzles. After investigation, the high performance was attributed to the low specific heat ratio that typically changes during expansions, for this reason this formulation was not used. The shifting equilibrium (Method 4) results in the highest predicted performance (I_{sp}) while the frozen reaction at the chamber, with calorically imperfect gas, predicts the lowest performance. In practice, the theoretical performance is bounded by the frozen in the chamber, and shifting equilibrium predictions. Method 3 is a compromise between the under prediction of Method 2 and optimism of Method 4. Method 3 is typically used to report combustion efficiencies (Castellini, 2012) so will be adopted here and used going forward.
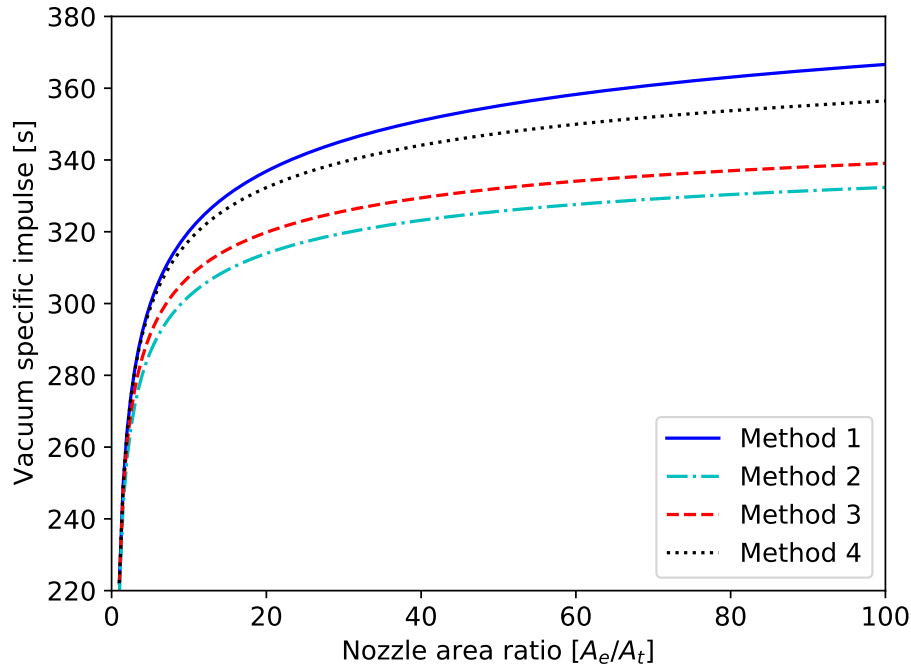
Figure 3.3: Vacuum specific impulse with different formulations for paraffin/LOx at $P_c = 2.4$ MPa, $OF = 2.2$

First/main Stage Nozzle Formulation

For first-stage nozzles, the above formulation is used with nozzle exit pressure provided as an input constrained by the flow separation criteria. Since a calorically imperfect gas

formulation was used, Eqn. 3.13 must be solved iteratively using a numerical Newton's method to find the area ratio for a given pressure ratio. The iterative method is in contrast to the analytic quality of Eqn. 3.10, which makes Method 1 a convenient choice.

The required mass flow rate for the first/main stages is calculated from modifying Eqn. 3.16 using average thrust and specific impulse at average conditions and initial ambient back pressure. The throat area is determined by modifying Eqn. 3.5. The first stage nozzle geometry, under the current formulation, has the possibility to affect the vehicle body diameter since the body diameter has to ensure coverage of all nozzles.

The perfectly expanded specific impulse is investigated for LOx/paraffin and N_2O/paraffin combinations at 50 kPa back pressure. The 50 kPa value was chosen as it meets Summerfield over-expansion criteria (Stark, 2005) with a 10 kPa margin - a potential first-stage nozzle design. The contour plots of OF and chamber pressure are presented in Fig. 3.4 and Fig. 3.5 for LOx and N_2O oxidizers respectively. The optimal OF lines are the lines of maximum I_{sp}, and change slightly across different chamber pressures. The optimal OF lines exhibit sharp transitions due to the resolution of the plotted data. LOx-based systems present higher specific impulse at lower OF values for the same chamber pressures.

Second-stage (Vacuum) Nozzle Formulation

A different formulation is introduced for upper stage nozzles. For upper stage nozzles, the available geometry is constrained by the first stage. For upper stages, the ambient pressure is usually small and the exit area is desired to be large. For vacuum-optimized nozzles, the maximum exit diameter is determined by vehicle body inner diameter of the housing section. The nozzle exit diameter is equal to the housing diameter minus an introduced non-dimensional clearance parameter (δ_{nozzle}) (Eqn. 3.17). The δ_{nozzle} parameter is the wall distance between the nozzle bell and the inner diameter of the interstage ($L_{nozzle,clearance}$), divided by the inner diameter of the interstage (Eqn. 3.18). The clearance parameter has a lower bound (Eqn. 3.19), to ensure feasible designs are generated with complete design

34
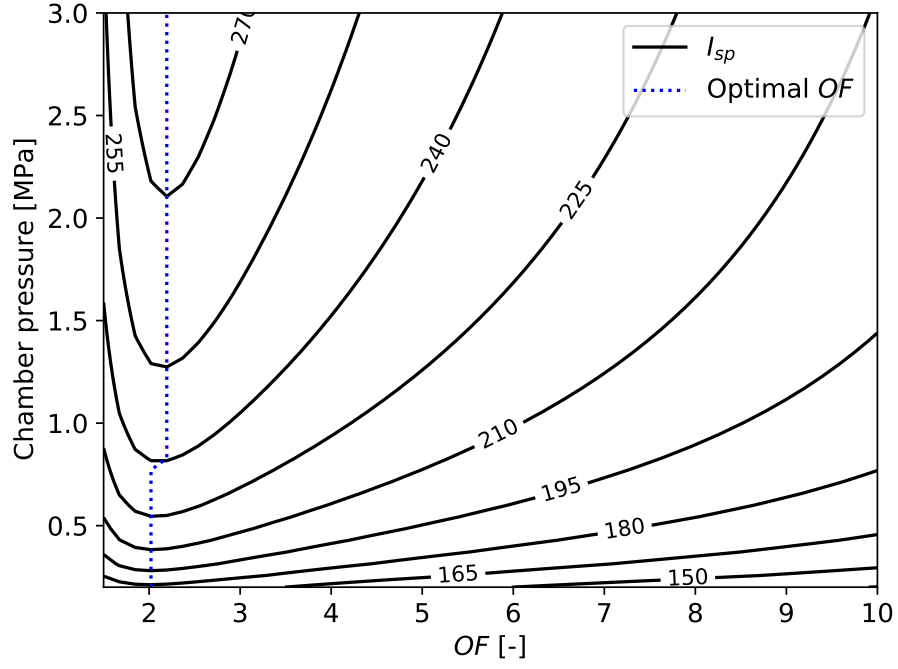
Figure 3.4: Typical first or main stage nozzle I_{sp} for LOx/paraffin and $P_e = P_{amb} = 50kPa$
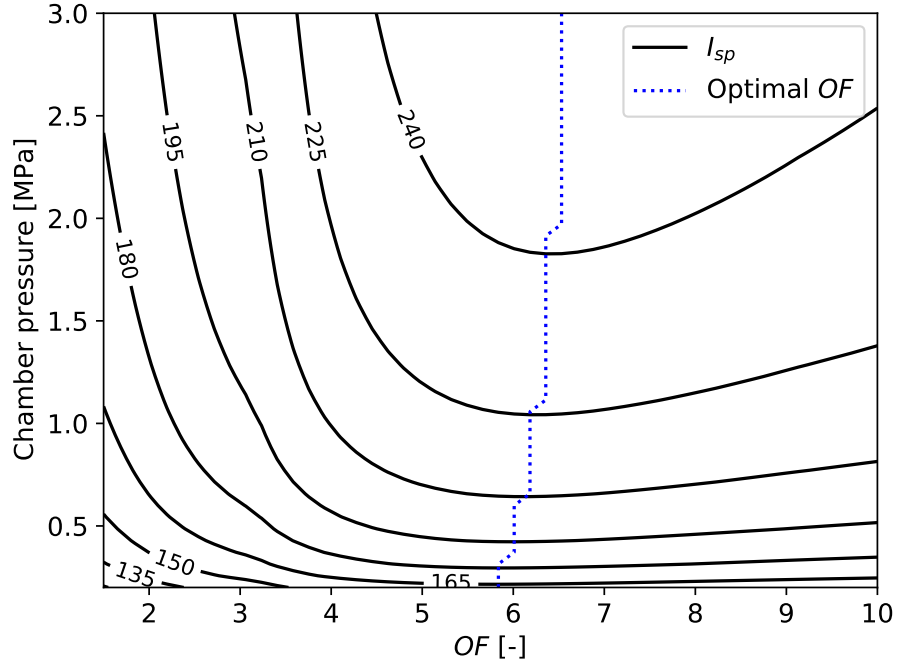
Figure 3.5: Typical first or main stage nozzle I_{sp} for N_2O/paraffin and $P_e = P_{amb} = 50kPa$

freedom to make any scale nozzle, within physical bounds. Upper stage nozzle throat area is determined iteratively with Newton's method with nominal vacuum thrust and exit area constraints (Eqns. 3.13, 3.15, and 3.16). The mass flow rate is calculated similarly to first-stage nozzles by modifying Eqn. 3.16 using average thrust and specific impulse at average conditions and zero initial back pressure assumed.

$$D_{exit} = (ID)_{interstage}(1 - 2\delta_{nozzle}) \tag{3.17}$$

$$\delta_{nozzle} = \frac{L_{nozzle,clearance}}{(ID)_{interstage}} \tag{3.18}$$

$$0.05 \leq \delta_{nozzle} < 0.5 \tag{3.19}$$

Propellant Masses and Geometry

The oxidizer and fuel nominal average mass flow rates are determined using the time-averaged oxidizer-to-fuel ratio (Eqn. 3.20). The variables $\dot{m}_{ox}$ and $\dot{m}_f$ are the oxidizer and fuel mass flow rates respectively, and $\dot{m}_{total}$ is the total combined mass flow rate with the over bar symbolizing a time-averaged quantity.

$$\overline{\dot{m}_{ox}} = \overline{\dot{m}_{total}} - \overline{\dot{m}_f} = \frac{\overline{\dot{m}_{total}}}{1 + (1/OF_{av})} \tag{3.20}$$

The individual propellant masses are determined by the average mass flow rates and burn time, Eqn. 3.21. The subscript i denotes an arbitrary propellant (fuel or oxidizer).

$$m_i = \overline{\dot{m}_i} \cdot t_b \tag{3.21}$$

A single-port, circular-cylinder fuel grain geometry is used in this study. The fuel radius regression-rate $(\dot{r}_f)$ power law, of the form shown by Eqn. 3.22, is used (Karabeyoglu et al.,

2007):

$$r_f = aG_{ox}^n \tag{3.22}$$

This regression rate from the given relation is spatially-averaged. The oxidizer mass flux (G_{ox}) is defined by Eqn. 3.23:

$$G_{ox} = \frac{\dot{m}_{ox}}{A_p} = \frac{\dot{m}_{ox}}{\frac{\pi}{4}(ID_f)^2} \tag{3.23}$$

The parameters a and n are empirically determined constants that are unique to each fuel and oxidizer combination. The regression rate constants used in this study are presented in Table 3.1. The parameter ID_f is the inner diameter of the fuel grain.

The oxidizer-fuel ratio in the aft of the chamber can be expressed as the ratio of respective mass flow rates. After incorporating the regression rate law, and rearranging, the oxidizer to fuel ratio can be approximately expressed by Eqn. 3.24. Variables ρ_f and L_f are the fuel mass-density and length.

$$OF = \frac{\dot{m}_{ox}}{\dot{m}_f} = \frac{\dot{m}_{ox}}{\rho_f \pi (ID_f) L_f a \left(\frac{\dot{m}_{ox}}{\frac{\pi}{4}(ID_f)^2} \right)^n} = \frac{\dot{m}_{ox}^{1-n}(ID_f)^{2n-1}}{4^n \pi^{1-n} a \rho_f L_f} \tag{3.24}$$

As seen in Eqn. 3.24, the OF will change during the duration of the burn (function of ID_f) for values of n that are not 0.5, if oxidizer flow rate is constant. This phenomena is known as the OF shift in hybrid rocket theory. During the OF shift, the surface area increase effect on fuel generation will be not equal the effect by the change in the local axial mass flux. The regression exponent n is reported to be 0.5 for N_2O/paraffin combinations (Paccagnella et al., 2019) so should exhibit no OF shift theoretically in this simplified representation.

The fuel internal diameter is constrained by the maximum allowable incoming mass flux of oxidizer. Studies have shown that there is an upper limit of mass flux permissible, before blow-off instabilities arise during combustion (Karabeyoglu et al., 2011). Experimental

values of maximum permissible mass fluxes for stable combustion can be found up to 500 $\frac{kg}{m^2 s}$ (Uddanti, 2015), for the present study this value will be used to constrain the fuel inner diameter.

Along with the port flux constraint, another constraint is added to the fuel initial port internal flow Mach number. To ensure the fuel port is not the choke point, the Mach number is kept below 1.0 initially. The Mach number constraint is achieved by taking the fuel ID to be the nozzle throat diameter, if it is originally smaller. The tight margins on the port flow Mach number constraint arise from assuming that the combustion products will react more completely in the aft chamber such that the combustion products in the fuel port will have a higher density and lower temperature.

The fuel outer diameter and length is determined through an iterative process. An axial-length-averaged, time-resolved numerical fuel regression simulation is used to solve for the fuel mass flow rate, by fuel regression (Eqn. 3.22), given a time-history or constant oxidizer mass flow rate. The numerical solver integration is accomplished by a Runge-Kutta 4th order scheme with a 0.01 s time step. Since the oxidizer mass flow rate history is defined by this stage of the conceptual design process, the required fuel outer diameter can be determined since the fuel regression in this analysis is independent of fuel axial length. The numerical simulation produces an OF history based on the ratio of mass flow rate histories. The numerical time-averaged OF is then converged to the input parameter OF_{av} by altering the length of the fuel grain using a numerical Newton's method.

The numerical results of a HRE fuel regression simulation are now generated for a defined test case. The relevant fuel and oxidizer parameters are taken from Table 3.1. The fuel geometry is taken from an operational N_2O/paraffin rocket (Messinger et al., 2019). The fuel inner diameter, outer diameter, and length were 3.81 cm, 9.525 cm, and 40.64 cm respectively. The oxidizer flow rate is taken to be a constant 1.2 kg/s and the simulations run until full fuel consumption. The results are presented in Fig. 3.6 and Fig. 3.7. The regression of paraffin with oxygen is relatively faster given the larger value of the a fuel

regression coefficient. The faster regression for the LOx case, for the same fuel grain, shows the OF history to be lower as the fuel mass flow rate is higher. The OF of the oxygen case also shifts over time as the regression exponent n is not equal to 0.5 as it is for N_2O. The design OF of the N_2O system is closer to optimal, near 6.0, as expected.
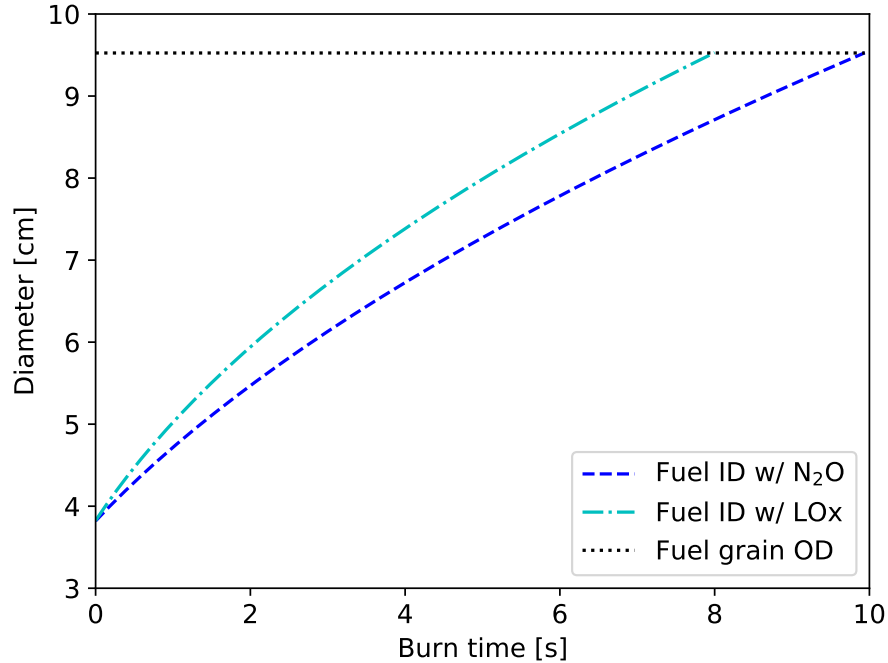
Figure 3.6: Fuel diameter history from hybrid regression simulation, for two different oxidizers, holding all else equal

The combustion chamber internal volume is not entirely defined by the fuel geometry. A pre-chamber section is added (a void volume upstream of the fuel surface within the combustion chamber) and is assumed to be 1.0 times the fuel outer diameter in length. The post chamber section (downstream of the fuel surface) is assumed to be 1.5 times the fuel outer diameter in length. Insulation encapsulates the fuel and pre/post sections. A constant 3.175 mm wall thickness is assumed for the insulation across scales.

The number of engines for a first/main stage can be between one and nine. Upper stage engines are limited to one in the current investigation as this is typically done for operational vehicles with relatively large, radiatively-cooled engine nozzle bells (?RocketLab, 2020a).
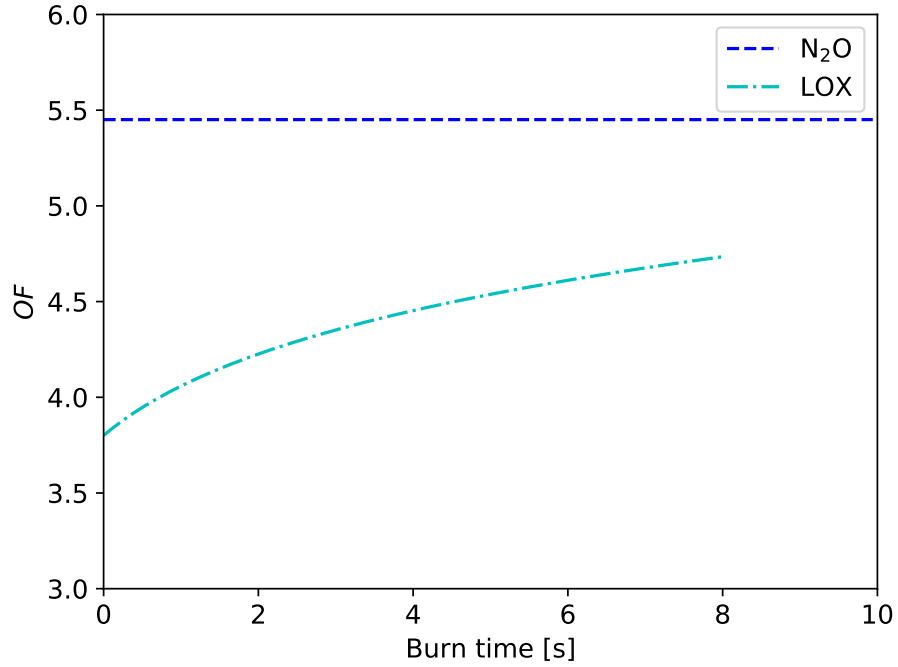
Figure 3.7: OF history from hybrid regression simulation, for two different oxidizers, holding all else equal

For multiple engines, the thrust, mean oxidizer flow, and fuel mass is split equally and the design propagates as usual, with all other aspects being equal. The optimal packing of equal circles in a circle (Graham et al., 1998) methodology was used for the engine placement and geometry formation. The optimal configurations, that minimize outer diameter, are presented in Fig. 3.8, and the major diameter values are presented in Table 3.2. The circle to pack is dictated by the maximum size of the engine or nozzle geometry with respective clearances.
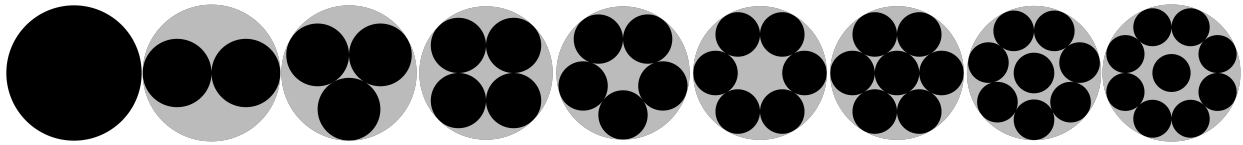
Figure 3.8: Optimal packing of circles within a circle, images from Wikimedia Commons (Koko90 and Patrick87, 2011).

Number of circles of diameter d	Major diameter, multiple of d
1	1
2	2
3	2.145
4	2.414
5	2.701
6	3
7	3
8	3.304
9	3.613

Table 3.2: Minimum outer diameter for packing various equal diameter circles

Generating Time-varying Propulsion System Properties

Given the time history of fuel and oxidizer mass flow rates are known, all relevant time-varying propulsion parameters can be determined. Since the nozzle throat has been defined from a time-averaged OF_{av} and fuel flow rate, the combustion pressure, and OF will change over the burn duration. The c^* and $I_{sp,vac}$ histories are quantified by taking into account the OF shift and change in combustion chamber pressure. The effect of chamber pressure on vacuum specific impulse, for varying area ratios, and characteristic velocity is observed to be small for moderate changes (± 10 %) of chamber pressure (Fig. 3.9). The effect of shifting OF had a relatively larger impact on specific impulse, for different area ratios, and characteristic velocity (Fig. 3.10). The nominal values of chamber pressure and OF are the same as the previous comparison of the different methodologies (Method 1-4) for consistency.

In the present formulation, since the change in chamber pressure is dependent on the change in mass flow rate and c^*, and c^* is a complex function of chamber pressure, an iterative process is required to determine the chamber pressure. The error of characteristic velocity calculated from Eqn. 3.5 with that of Eqn. 3.13 multiplied by the combustion efficiency (η_c) was minimized using numerical Newton's method. The change in OF and P_c was used to calculate the c^* and $I_{sp,vac}$ histories used for each instant of the burn duration. To increase computational speed, the effect of changing pressure may possibly be neglected, however this may not be the case for commanded oxidizer mass flow rate changes (throttling).
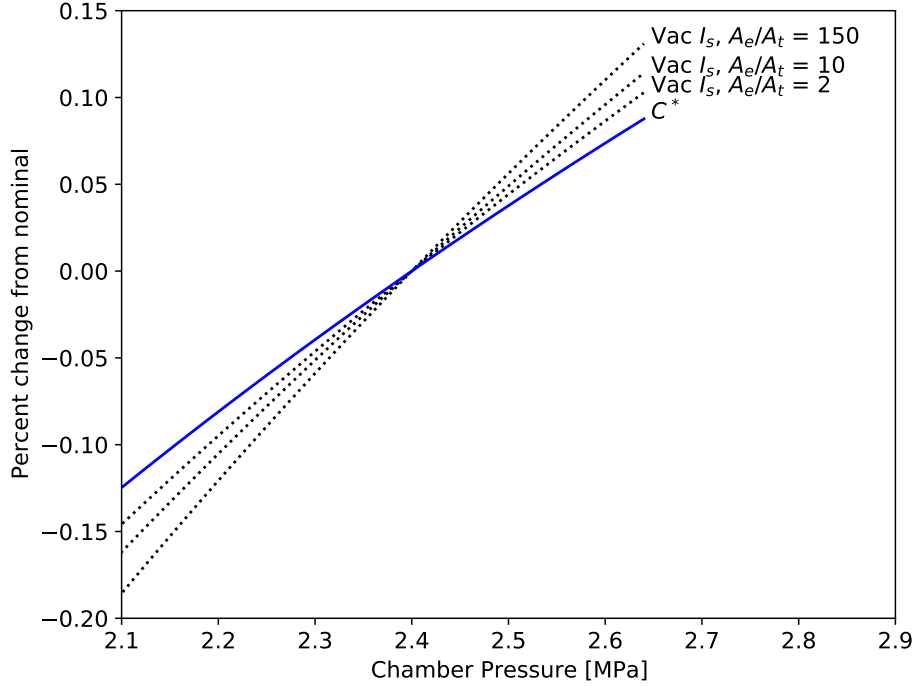
Figure 3.9: Percent variation from nominal, with shifting chamber pressure, for $LOx/$paraffin at $P_c = 1.0 MPa$ and constant $OF = 2.2$

3.1.2 Feed System Design and Scaling Parameters

The feed system types considered for the current conceptual design are pressure-fed and electric pump-fed systems. The pump-fed case requires a back-fill pressurant to maintain the required net positive suction pressure (NPSP). The pressure-fed configurations include either self-pressurizing or gas pressurant-fed.

Self-pressurizing Pressure-fed

Nitrous oxide is a commonly used self-pressurizing oxidizer due to its relative high density and high vapour pressure at standard conditions. An equilibrium model of depressurization has been used do predict the residual propellant percent required for a self-pressurizing feed system. The equilibrium model of self-pressurizing propellant tanks has been studied and a formulation and evaluation can be found in the work of Zimmerman et al. (2013). The
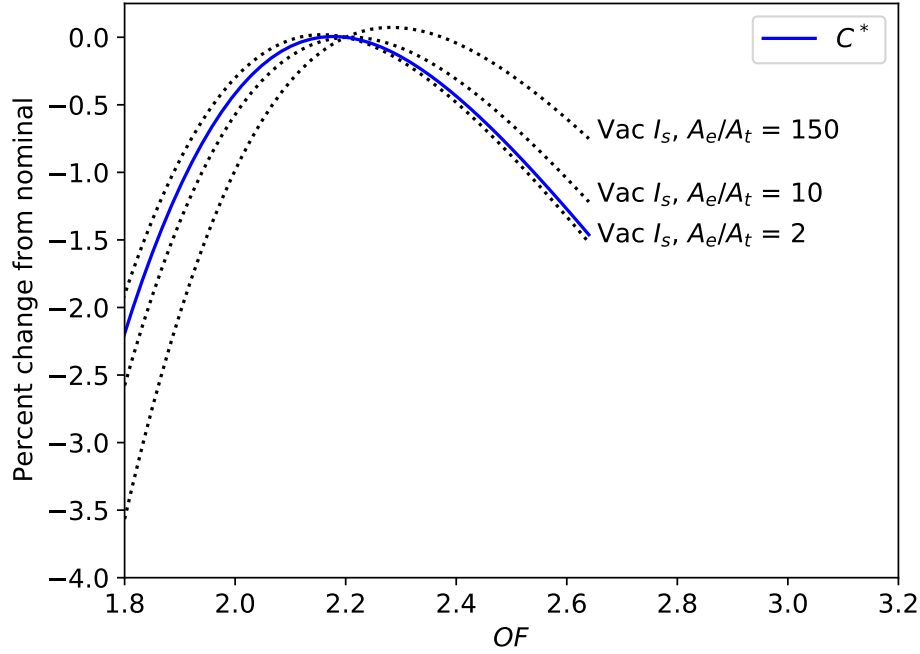
Figure 3.10: Percent variation from nominal, with shifting OF, for LOx/paraffin at $P_c = 1.0 MPa$ and constant $OF = 2.2$

model assumes an adiabatic fluid cell in constant thermodynamic equilibrium undergoing liquid mass depletion. Conservation of mass and energy differential equations are numerically integrated and the fluid properties are simultaneously calculated at each time step. A single-phase, incompressible flow model is used to predict the oxidizer flow rate characteristics based on upstream and downstream pressure. The choice of flow model is not important as only the characteristics of the equilibrium model are of use here. The oxidizer mass residual percent is insensitive to initial oxidizer mass or average mass flow rate, under the assumptions, but is found to be a sole function of the initial equilibrium temperature (Fig. 3.11). A fifth-order polynomial can be fit to the residual N_2O mass percent at 30 equally-spaced initial temperatures between 193 K and 303 K. The polynomial is presented in Eqn. 3.25, where T is the initial N_2O temperature. The relation provides percent of initial mass that is residual vapour as a function of initial equilibrium temperature in K. The relation is valid for temperatures between 193 K and 303 K with 0.02% maximum absolute error and 0.014

43

% mean absolute error.
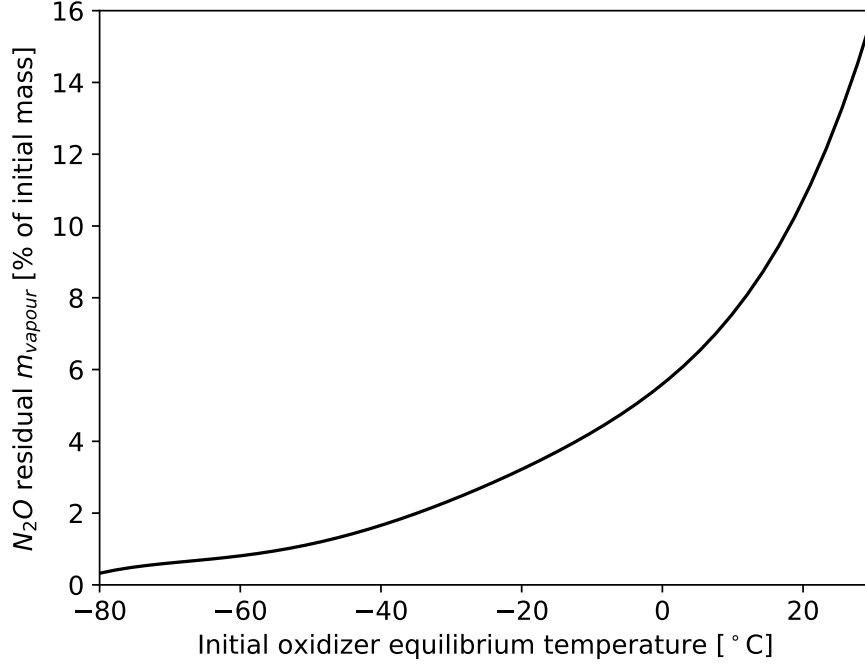
Figure 3.11: Residual vapour mass needed for self-pressurizing at different initial temperatures

$$m_{\%,res} = a_5 T^5 + a_4 T^4 + a_3 T^3 + a_2 T^2 + a_1 T^1 + a_0 \qquad (3.25)$$

For the above equation, note the following:

$a5 = 5.45433770 \times 10^{-9}$
$a4 = \text{-}6.42332250 \times 10^{-6}$
$a3 = 3.01920031 \times 10^{-3}$
$a2 = \text{-}7.07145384 \times 10^{-1}$
$a1 = 8.24886405 \times 10^{1}$
$a0 = \text{-}3.83304277 \times 10^{3}$

Back-fill Pressure-fed

For back-fill pressure-fed systems, the pressurant mass is determined assuming an adiabatic ideal gas expansion to the final tank volume and pressure from the initial pressurant tank

pressure and temperature. The pressurant mass is calculated from Eqn. 3.26 assuming ideal gas properties during depressurization (Castellini, 2012). The resulting mass is multiplied by a factor, c_{pg}, to provide a margin. A value of 1.2 is used for c_{pg} in this study, as was used by Castellini (2012).

$$m_{pg} = c_{pg} \frac{P_{ox}V_{ox}}{R_{pg}T_{1,pg}} \left(\frac{\gamma_{pg}}{1 - \frac{P_{ox}}{P_{1,pg}}} \right) \qquad (3.26)$$

The initial temperature and pressure of the pressurant gas are design parameters. The pressurant density is found by an equation of state in CoolProp (Bell et al., 2014). The volume requirements are calculated from the required mass.

Electric Pump-fed

The electric pump feed system is defined by the power requirements of the pump and batteries, and the energy requirements of the batteries, while taking into account pump efficiency. The pump instantaneous power is expressed in Eqn. 3.27 :

$$\mathcal{P}_{ep} = \frac{\dot{m}_{ox}\Delta P_{ep}}{\rho_{ox}\eta_{ep}} \qquad (3.27)$$

Where $\mathcal{P}_{ep}$ is the electric pump required power, η_{ep} is the electric pump efficiency, and ΔP_{ep} is the difference between the pump inlet and outlet pressure, or oxidizer tank and injector inlet.

The total energy is the temporal integral of the power used over the burn duration 3.28

$$E_{ep} = \int_0^{tb} \mathcal{P}_{ep}dt \qquad (3.28)$$

The battery mass (m_b) is determined from an empirical battery energy density (δ_{be}) and battery power density(δ_{bp}). The battery mass is determined from the maximum of the energy limited or power limited case, as per Eqn. 3.29:

$$m_b = max\left(\frac{\mathcal{P}_{ep,max}}{\delta_{bp}}, \frac{E_{ep}}{\delta_{be}}\right) \tag{3.29}$$

The pump mass is calculated based on a pump mass estimating relationship assuming a constant pump power density (δ_{ep}) across different engine sizes (power and flow rate requirements) (Eqn. 3.30). The pump power density parameter captures the pump housing, electric motor, and inverter which can all be taken as a a function of the power requirement (Kwak et al., 2018). Values adapted from (Kwak et al., 2018; Gegeoglu et al., 2019; Casalino et al., 2019b) are presented in Table 3.3 for use in this thesis.

$$m_{ep} = \frac{\mathcal{P}_{ep,max}}{\delta_{ep}} \tag{3.30}$$

The net positive suction pressure (NPSP) is the absolute pressure at the inlet eye of the centrifugal pump (Eqn. 3.31). The available NPSP ($NPSP_A$) is a function of pressurant gas pressure (P_{pg}), static pressure in the oxidizer tank, and the vapour pressure of the oxidizer ($P_{vap,ox}$). Where the static pressure in the oxidizer tank is equal to the following expression: $\rho_{ox}|\overrightarrow{a}|h_{ox}$, and where h_{ox} is the current liquid level height and $|\overrightarrow{a}|$ is the apparent acceleration.

$$NPSP_A = P_{pg} + \rho_{ox}|\overrightarrow{a}|h_{ox} - P_{vap,ox} \tag{3.31}$$

The available NPSP is required to be below a certain value to avoid cavitation during the operation of the electric pump in order to prevent significant mechanical wear to the impeller. The value of $NPSP_R$ is dictated by the detailed design of the impeller; a constant value is assumed based on existing literature values (Campbell and Farquhar, 1973).

$$NPSP_A \geq NPSP_R \tag{3.32}$$

Electric pump attribute (units)	Value
Pump assembly power density (δ_{ep})	3.9 kW/kg
Battery power density (δ_{bp})	3.0 kW/kg
Battery energy density (δ_{be})	324.0 kJ/kg
Pump efficiency (η_{ep})	66 %
Required NPSP	350 kPa
Battery mass density	1000 kg/m^3
Pump assembly mass density	500 kg/m^3

Table 3.3: Electric pump constants

3.2 Generating the Overall Structure and Geometry

General quantities of the vehicle and propulsion system have been defined thus far. This next section introduces some assumptions in order to begin to generate a more-detailed vehicle structural design.

To limit the design space, the vehicle configurations are limited to be one or two stages. The vehicle outer diameter is constant along the length, and can be chosen as an input variable, but is constrained to not be smaller than the outer diameter of the first/main stage combustion chamber(s) and nozzle(s), or second stage combustion chamber, all with a clearance. The assumption is made that there is no aft flare of converging tail fairing and the nosecone maximum diameter matches the body diameter. The vehicles looks similar to what is depicted in Fig. 3.12.

All load-bearing external surfaces that experience and transmit aerodynamic, inertial, internal pressure, and thrust forces are sized based on stressed-based methods. Each element's respective structural section is modeled as a thin cylinder with constant wall thickness. The analysis of grid-stiffened and/or reinforced structures, that are sometimes employed in flight vehicles (Bruhn, 1973), would require more complicated structural analysis, and is not incorporated in the present study.

The rocket vehicles under study in this thesis are comprised by several base elements. The elements that can comprise a vehicle are:

47

Nosecone - conic or ogive section housing the payload.

Upper-tank - above oxidizer tanks, houses valves and internal pressurant tanks.

Inter-tank - houses feed system components and thrust structure.

Oxidizer tank - external oxidizer tank.

Engine - houses the first stage engine(s) and holds the weight of the rocket vehicle while on pad.

Inter-stage - houses second stage engine, feed system, and thrust structure.
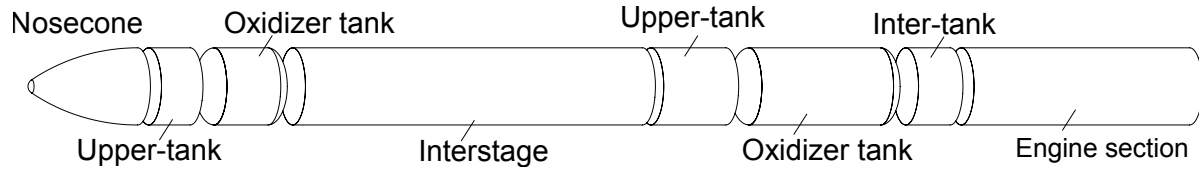
Figure 3.12: Conceptual layout of rocket elements

Each element has properties of mass, mass-moment of inertia, and center of mass. All elements are assumed axi-symmetric in relation to geometry and mass distribution. All components masses are assumed to be distributed uniformly in each section in order to calculate each respective moment of inertia. The nosecone is assumed to be a hollow cone in order to calculate center of gravity and moment of inertia, with payload point mass at the cone's center of mass. All cylindrical elements are assumed to be homogeneous uniform-mass cylinders for moment of inertia calculations.

3.2.1 Nosecone

The nosecone outer geometry is defined by the body diameter OD, nosecone fineness ratio f_n (length/diameter), bluntness ratio BR_n (nose radius/diameter), and nosecone type. The nosecone types investigated here are limited to ogive or conic. The nosecone shell thickness is sized from stress-based analysis, which will be the topic of future sections. The nosecone mass is comprised of payload mass, and shell (fairing) mass. The faring separation from the nosecone can be included in flight simulations, and is performed at specific altitude and speed conditions. The fairing is separated as early as possible to improve performance. The

separation altitude of 110 km is used in the present analyses as it is consistent with Rocket Lab and SpaceX typical fairing separation altitudes for their respective missions (SpaceX, 2020; RocketLab, 2020a).

3.2.2   Upper-tank

The upper-tank element, is a thin-walled, circular cylindrical element, always placed forward of an oxidizer tank element. The element is rigidly attached to the cylindrical body of the oxidizer tank. The element length is sized based on volume requirements of the components, length of pressurant-gas tank, rocket body diameter, and end cap type of the oxidizer tank. The volume around the end cap, extending from the cylindrical section of the oxidizer tank to the apex of the dome, is assumed to be unusable. The upper-tank components consist of avionics, pressure transducers, and valves, along with the pressurant tank (if needed). The pressurant tank is amused spherical. If a spherical vessel does not fit within the prescribed body diameter an internal cylindrical vessel with hemispherical ends is used.

The avionics and pressure transducers are assumed to be constant regardless of vehicle size at 3.5 kg and 0.5 kg respectively, per stage. The constant mass values are from an operational sounding rocket (Messinger et al., 2019). Each upper tank section has two valves sized for oxidizer tank venting and pressurant gas injection. The valve mass is calculated based on a semi-empirical relation from Tizón and Roman (2017) (Eqn. 3.33). The relation is based on a existing values of a valve with reference properties, denoted by the subscript 0. The reference properties for a ball valve and solenoid valve are provided in Table 3.4. The reference ball valve is an Assured Automation 26 series stainless steel ball valve with N_2O-compatible PTFE seals and PD008 actuator. The reference solenoid valve is Gems Sensors A2011-V-VO-C203. Both of the referenced valves were used in previous work (Messinger et al., 2019). Each engine required a single ball valve, sized with the same valve material properties but with different flow properties from the present vehicle design. Each oxidizer tank possessed a dump valve that relieved the entire tank contents in 30 minutes, and an

49

Valve type	$m_{valve,0}$	ΔP_0	$\dot{m}_0$	ρ_{fluid0}	$\rho_{valve},0$	σ_{allow0}	$MEOP_0$
Solenoid valve	0.3 kg	6.9 MPa	0.1 kg/s	800 kg/m^3	7850 kg/m^3	200	6.9 MPa
Ball Valve	1 kg	6.9 MPa	1.2 kg/s	800 kg/m^3	7850 kg/m^3	200	6.9 MPa

Table 3.4: Initial valve scaling constants used

identical valve used as the vent, and a third identical valve used as the pressurant inlet valve. No sensitivity analysis or validation is carried out for the valve mass scaling as the impact on performance is assumed small.

$$\frac{m_{valve}}{m_{valve,0}} = \left(\frac{\Delta P}{\Delta P_0}\right)^{0.3} \left(\frac{\dot{m}}{\dot{m}_0}\right)^{0.625} \left(\frac{\rho_{fluid}}{\rho_{fluid0}}\right)^{-0.625} \left(\frac{\rho_{valve}}{\rho_{valve0}}\right)^{1} \left(\frac{\sigma_{allow}}{\sigma_{allow0}}\right)^{1} \left(\frac{MEOP}{MEOP_0}\right)^{1} \quad (3.33)$$

3.2.3 Oxidizer tank

The oxidizer tank element consists of the cylinder structure, end caps, and fluid. The tank structure geometry, material density, fluid volumes, and fluid densities are used to calculate mass, center of gravity, and mass-moment of inertia. The end cap types that are implemented are elliptical and flat plate. Spherical is a special case of elliptical, and is the most mass-efficient but requires the longest coupling section. The flat end cap type has the smallest coupling distance but has the largest mass. The pressure vessel structural design and scaling will be discussed more in the propellant tanks stress-based sizing section.

3.2.4 Inter-tank

The inter-tank element is between an oxidizer tank element and engine element. The element consists of a structural shell coupling attached to the aft of the oxidizer tank cylindrical section and includes a thrust structure to transmit loads from the engine(s). The inter-tank also houses all feed system components. The feed system components are: valve(s), feed lines, electric pump(s), and batteries. The length is sized based on the volume constraints,

given the mass and density of internal components, and the body diameter. The mass is comprised of the components mass and structural shell mass. The thrust structure cross-sectional area is sized per engine assuming simple axial compression and the thrust structure length spans the length housing the feed system components. It's assumed that the thrust structure section properties can be designed in such a way that material yield, and not buckling, will be the failure mode. The feed system line flow area is sized based on a limit design velocity and oxidizer volumetric flow per engine. The flow area, line pressure, and inter-tank length provides the feed line mass per thin-walled pressure vessel theory, which will be discussed in the structural analysis section.

3.2.5 Engine

The engine component consists of combustion chamber(s), fuel, nozzle(s), and a structural shell that extends from the end of the inter-tank to the start of the nozzle(s). The engine shell is sized to withstand the static load of the vehicle on the pad as well as the dynamic flight loads. The overall element length is determined from the combustion chamber and nozzle length.

The nozzle geometry is generated using the bell (parabolic) formulation outlined in Sutton and Biblarz (2001). Given the throat diameter, exit diameter, and combustion chamber outer diameter the nozzle contour can be fully defined. A straight 45° half angle converging section is used that is tangent to the throat fillet and is coincident with the combustion chamber outer diameter. Per the Sutton formulation, a 80% bell contour with an 8.5° exit half angle is used. The throat fillet to parabola transition angle is 30°. The throat aft and fore fillets are 1.5 and 0.4 throat radii respectively. The non-zero nozzle exit angle contributes a 0.995 nozzle correction factor applied to the momentum thrust term in the thrust coefficient. A nozzle contour with an area ratio of four, and inlet diameter of eight throat radii (r_t), is shown in Fig. 3.13.

The nozzle mass is determined from the addition of a nozzle MER from Miranda (2015)

51

and from a stress-based method. For the stress-based method, thin-walled pressure vessel theory is used to size the wall thickness given pressure, geometry, and material. The converging section internal pressure is assumed constant at the nominal chamber pressure, while the entire divergent section is assumed to be at the choked-flow (nozzle throat) static pressure. The thickness and contour can define the volume, and the material mass density can be used to determine mass. The additional nozzle MER is presented in Eqn. 3.34; it is based on existing designs and is solely a function of vacuum thrust in kN, and provides mass, in kg. To account for the influence of the geometry, and not just thrust magnitude, the stress-based method is added to the existing MER (Eqn. 3.35). The additional mass for the pressure vessel aspect accounts for the larger divergent section needed for higher expansion ratio nozzles, since most of the database used to generate the used nozzle MER is from first stages/boosters data.
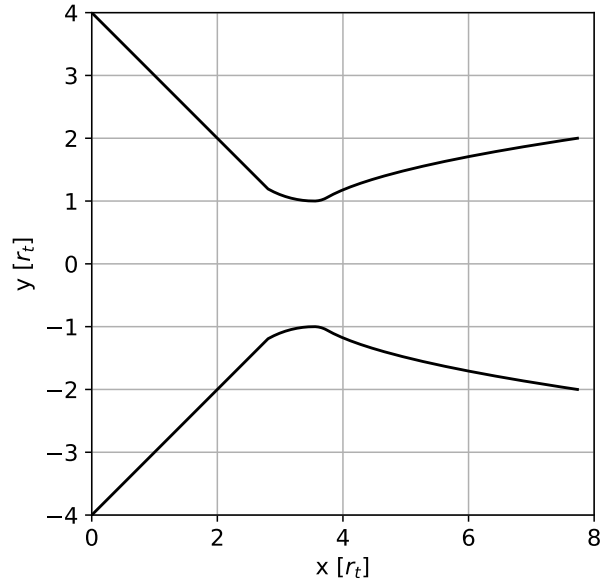
Figure 3.13: First stage nozzle contour with inlet meeting combustion chamber

$$
m_{nozzle,0} = \begin{cases} 0.0006(T_{vac})^2 - 0.3214(T_{vac}) + 263.82, & T_{vac} > 200kN, +TVC \\ -0.0018(T_{vac})^2 + 1.004(T_{vac}) - 1.942, & T_{vac} \leq 200kN, +TVC \\ 0.1605(T_{vac})^{1.2466} & T_{vac} \leq 200kN \end{cases} \tag{3.34}
$$

$$
m_{nozzle} = m_{nozzle,0} + m_{nozzle,pv} \tag{3.35}
$$

3.2.6 Interstage

The interstage is connected to the lower stage upper-tank and connects to the upper stage oxidizer tank. The interstage element inherits all attributes from the inter-tank element, but only holds the components pertaining to the second stage. Interstages are only used when more than one stage is simulated. The combustion chamber(s) and nozzle(s) mass and length are incorporated in the element, along with all quantities that are contained in the inter-tank element. The structural shell is jettisoned when staging occurs (i.e remains with the first stage).

3.3 Aerodynamics

The aerodynamic forces on the vehicle, axial force (drag) and normal force (lift), are computed for each element. The normal force distribution over the entire vehicle is used to determine vehicle loads, stresses, and ultimately size vehicle components under assumed structural failure criteria. The magnitude and resultant of the normal force is used to calculate the required thrust vector to ensure static control can be obtained. The drag is used to determine the axial force distribution and in the numerical flight simulation equations of motion. This type of component-buildup method is used in other programs (Hammond, 2001), and is used for its computational speed over lattice/panel methods or computational

fluid dynamic (CFD) methods. The increase in computational speed comes with reduced accuracy, but is necessary for large parametric or optimization studies.

This investigation incorporates the 1997 version of Missile Datcom (Blake, 1998). The Missile Datcom source code was made publicly available in the supplementary material of Design Methodologies for Space Transportation Systems by Hammond (2001). The aerodynamic quantities used in this study are: the zero angle of attack drag coefficient (C_{D_0}), the normal force derivative with angle of attack, at zero angle of attack (C_{N_α}), and the center of pressure x_{cp} at zero angle of attack.

The definition of the drag coefficient is presented here in Eqn. 3.36 and 3.37. Where ρ is the local air density, U is the local airspeed magnitude, and A_{ref} is the reference area based on the diameter of the nosecone base-circle. The diameter will be constant along the axial length of the vehicle in this investigation,

$$C_D = \frac{D}{\frac{1}{2}\rho U^2 A_{ref}} \tag{3.36}$$

$$C_{D_0} = \frac{D|_{(\alpha=0)}}{\frac{1}{2}\rho U^2 A_{ref}} \tag{3.37}$$

where q is the dynamic pressure:

$$q = \frac{1}{2}\rho U^2 \tag{3.38}$$

For the geometry of the vehicles assumed in this study, the drag will only be comprised of wave, friction and base (pressure) components (Eqn. 3.39):

$$C_D = C_{D_w} + C_{D_f} + C_{D_{base}} \tag{3.39}$$

In this study the normal force will be determined, in the small angle of attack regime, as a linear function of angle of attack, from Eqns. 3.40, 3.41, 3.42:

$$C_N = \frac{N}{\frac{1}{2}\rho U^2 A_{ref}} \tag{3.40}$$

$$C_N \approx \left.\frac{\partial C_N}{\partial \alpha}\right|_{(\alpha=0)} \alpha \tag{3.41}$$

$$C_{N_\alpha} = \frac{\partial C_N}{\partial \alpha} \tag{3.42}$$

The center of pressure is defined by the following:

$$x_{cp} = \frac{\int x \cdot P(x)dx}{\int P(x)dx} \tag{3.43}$$

The center of pressure will be calculated using exclusively the normal forces since angle of attack is assumed to be small. The center of pressure due to the finite discrete normal forces is calculated with the following:

$$x_{cp} = \frac{\sum_i^n x_{cp,i} \cdot C_{N_\alpha,i}}{\sum_i^n C_{N_\alpha,i}} \tag{3.44}$$

3.3.1   Nosecone: Wave Drag, Normal Force, and Center of Pressure

The nosecone aerodynamic quantities are calculated using the methods contained in 1997 Missile Datcom. The methods use: The Second Order Shock Expansion (SOSE) theory, Van Dyke Hybrid theory, and the Modified Newtonian theory (Blake, 1998). All three methods are called directly from the compiled Datcom code. The SOSE method assumes an attached oblique shock at the tip of the nosecone and subsequent expansions along the length assuming each local change is conical. SOSE has been shown to have up to 20% error for low supersonic flight Mach numbers (M $\leq$ 2.0), It is in this region Van Dyke Hybrid theory is used (Blake, 1998). The SOSE method is used between Mach 2.0 and 6.0; beyond

Mach 6.0, the Modified Newtonian Theroy is used. Datcom uses a semi-empirical transonic (Mach = 0.8 to Mach 1.2) method based on experimental data for ogive and conic noses and nose-body combinations. The Datcom transonic method uses data from experiments by Messerschmitt-Boelkow-Blohm (Messerchmitt-Boelkow-Blohm, 1970).

In this investigation, for a given nosecone type and geometry (fineness ratio, bluntness ratio, and base diameter), a lookup table of aerodynamic coefficients is generated using Datcom, to be linearly interpolated as required. The coefficients generated are center of pressure (x_{cp}), zero-angle-of-attack normal force derivative (C_{N_α}), and wave drag (C_{D_w}) at flight Mach numbers from 0 to 20. The skin friction drag and base drag methods of Datcom were not used, but similar methods are incorporated as needed. Datcom was not called exclusively because it does not export the pressure distribution along the body (or element C_{N_α} and x_{cp}), information which is necessary to calculate more accurate loads and stresses. Datcom instead only returns the center of pressure and coefficients for forces/moments acting at the center of pressure. Calling Datcom at every required time step during flight simulations would be too slow for large parametric/optimization studies. The method used in this investigation appeared to be a good compromise between speed, accuracy, and development time.

3.3.2   Skin Friction Drag

The method of determining skin friction drag for the nose and cylindrical sections was from Niskanen (2009) as adapted from Barrowman (1967). These methods are semi-empirical and based on experimental data for the turbulent flow regime. The incompressible skin friction coefficient, C_f, is dependent on the Reynolds number (Eqn. 3.45) and flow regime (dictated by Reynolds number), above the critical reynolds number is dependent on the relative roughness height ($\frac{\epsilon}{L}$) where ϵ is the roughness height and L is the vehicle length. Roughness heights in the range of 100-200 μm will be used in this investigation and correspond to unpolished metallic surfaces (Niskanen, 2009). The critical Reynolds number used by Niskanen

is presented in Eqn. 3.46. The skin friction coefficient is found by the expression in Eqn. 3.47.

$$Re = \frac{\rho U L}{\mu} \tag{3.45}$$

$$R_{e,crit} = 51 \left(\frac{\epsilon}{L} \right)^{-1.039} \tag{3.46}$$

$$C_f = \begin{cases} 1.48E - 2 & Re < 1 \times 10^4 \\ (1.50 \ln Re - 5.6)^{-2} & 1 \times 10^4 \leq Re < R_{e,crit} \\ 0.032(\frac{\epsilon}{L})^{0.2} & Re \geq R_{e,crit} \end{cases} \tag{3.47}$$

The compressibility-corrected skin friction coefficient, $C_{f,c}$, is a function of both flight Mach number and Reynolds number flow regimes and is determined from Eqn. 3.48.

$$C_{f,c} = \begin{cases} C_f(1 - 0.1M^2) & M \leq 1 \\ \frac{C_f}{(1+0.15M^2)^{0.58}} & M > 1, 1E4 \leq Re < Re_{crit} \\ max(\frac{C_f}{(1+0.15M^2)^{0.58}}, \frac{C_f}{1+0.18M^2}) & M > 1, Re \geq R_{e,crit} \end{cases} \tag{3.48}$$

The friction drag coefficient expression from Niskanen (2009) is used (see Eqn. 3.49). The expression changes the reference area from wetted area to the area of the nose base circle. The term is corrected using the vehicle aspect ratio (AR).

$$C_{D_f} = C_{f,c} \frac{(1 + \frac{1}{2AR}) A_{wet,body}}{A_{ref}} \tag{3.49}$$

3.3.3 Base Drag

The rocket experiences base drag given by the relation by Fleeman (2006). When the engines are firing, base drag is assumed to be zero. The base drag force is applied to the nosecone

element since the nosecone has the projected area necessary to transmit the drag force. Using this relation, the calculated base drag agrees with Datcom, as will be seen in the verification section.

$$C_{D_{base}} = 0.12 + 0.13M^2, M \leq 1 \tag{3.50}$$

$$C_{D_{base}} = 0.25/M, M > 1 \tag{3.51}$$

3.3.4 Cylindrical Section Normal Force

The cylindrical body C_{N_α} method is adapted from the method of Galejs (2018) (Eqn. 3.52). The method needed to be linearized in the region of application, to determine the response to small angles of attack away from the zero angle of attack reference point (otherwise C_N will be zero). A linear relationship is assumed between 0 and 0.025 radians, or approximately 1.4 degrees. The linearized relation is also corrected for compressibility using the Prandtl–Glauert transformation presented by Niskanen (2009) (Eqns. 3.52 and 3.54). To remedy the singularity in Eqn. 3.53, if the flight Mach number M is between 0.8 and 1.2, the value of 0.8 is used. A value of 1.05 for K in Eqn. 3.52 and a minimum value of α of 0.025 radians to linearize C_N leads to a good agreement with subsonic/transonic values for nose/cylinder combinations from Messerchmitt-Boelkow-Blohm (1970) in Datcom. Beyond Mach 2.0 the cylindrical body contribution is small compared to the nose.

$$C_{N_{\alpha,M=0}} = 2K\frac{A_{plan}}{A_{ref}}\alpha \tag{3.52}$$

$$C_{N_\alpha} = \frac{C_{N_{\alpha,M=0}}}{\beta} \tag{3.53}$$

$$\beta = \sqrt{|1 - M^2|} \tag{3.54}$$

3.3.5 Verification and Validation

The verification and validation is carried out in two major steps. The first step includes verifying and validating 1997 Datcom to an existing set of sounding rocket aerodynamic data. The lighter-weight method used in this investigation (outlined previously) is then verified against 1997 Datcom.

The data compared to Datcom alone were CFD results, zero-angle-of-attack normal force coefficient derivative with angle of attack C_{N_α}, center of pressure x_{cp}, and drag C_{D_0}, for the Maxus sounding rocket (Hammargren, 2018). The CFD results are generated by Harmmargren. The experimental results for the same coefficients are reported by Elvemar (1990). The vehicle geometry can be found in the appendix of Harmagren's thesis (Fig. 3.14).
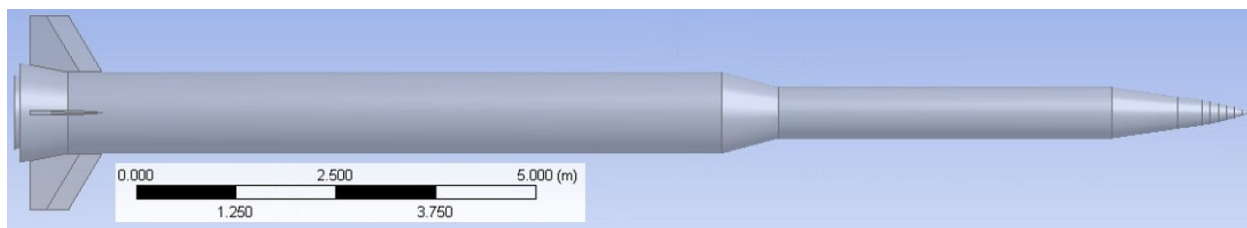
Figure 3.14: Maxus sounding rocket model adapted from Hammargren (2018)

The C_{D_0}, C_{N_α}, and x_{cp} Datcom predictions and comparison are presented in Fig. 3.15, 3.16, and 3.17 respectively. The results generated from Datcom are within the 20% margin stated by the software user guide (Blake, 1998). The largest discrepancies appear to be in the transonic regime for all aerodynamic coefficients and the center of pressure beyond Mach 6.0, which is when the calculation transitions to modified Newtonian theory.

The simplified routines used in this thesis were verified against Datcom. A verification study was conducted using a rocket with a body aspect ratio of 20, an ogive nose of fineness ratio 2.0, and 100 μm roughness height. The large aspect ratio was chosen to present the largest error. Error is reduced for lower aspect ratios as the vehicle is a larger portion nosecone and thus the two methods converge since the noscone aerodynamics are identical. The results using the simplified method and using Datcom directly are displayed in Fig 3.18,
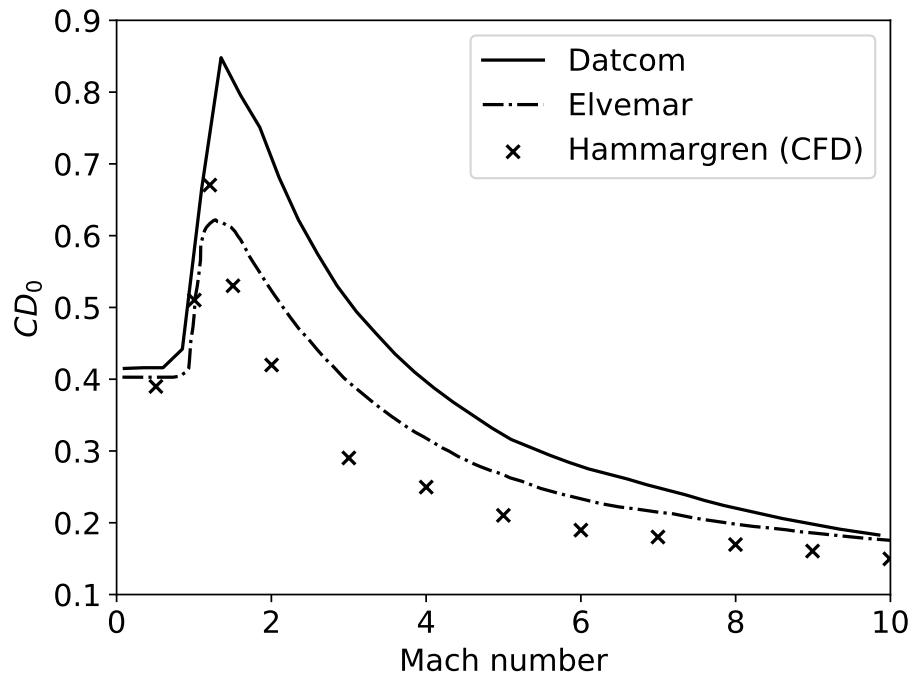
Figure 3.15: Maxus zero angle of attack drag coefficient
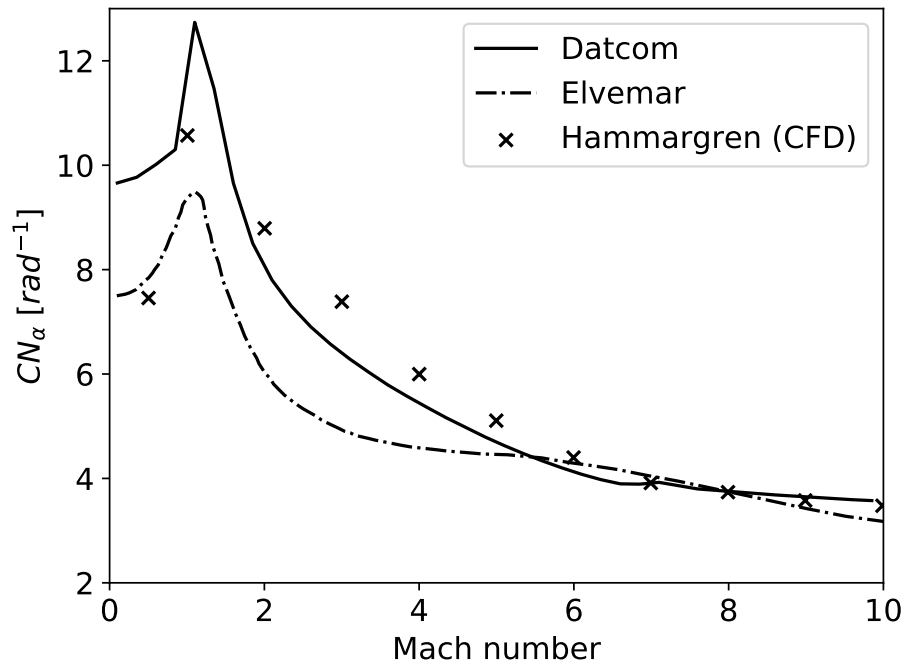
Figure 3.16: Maxus zero angle of attack normal force coefficient derivative
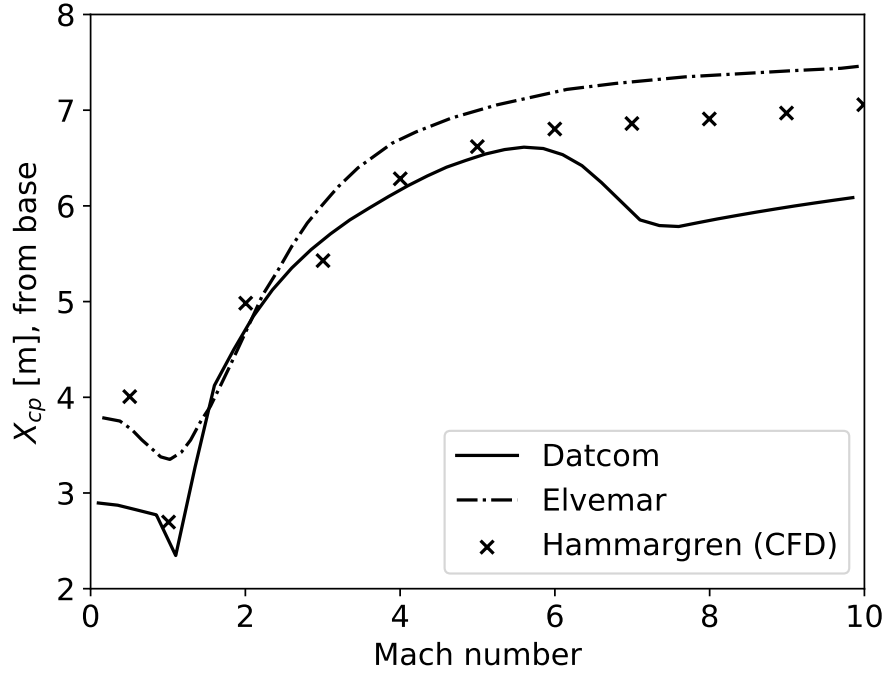
Figure 3.17: Maxus zero angle of attack center of pressure

3.19, and 3.20. The aspect ratio of 20 was selected as a representative upper-bound, based on the commercial launcher data assembled by Woodward (2017).

The error in the results, for all values, of the verification study with Datcom become smaller as flight Mach number increases. This is expected as the majority of the aerodynamic normal force is from the nosecone in this regime, and the nosecone methods are identical to within the error caused by linear interpolation. The drag error also reduces as flight Mach number increases as the wave drag becomes a larger fraction of total drag.

3.4 Flight Simulation

The flight simulation of a launch vehicle is usually performed by means of two or more reference frames, typically one with origin at the center of the Earth and the other one moving with the vehicle. To model the translational motion, the vehicle can be treated as a particle, ignoring the size and mass distribution. In modeling the rotational motion,
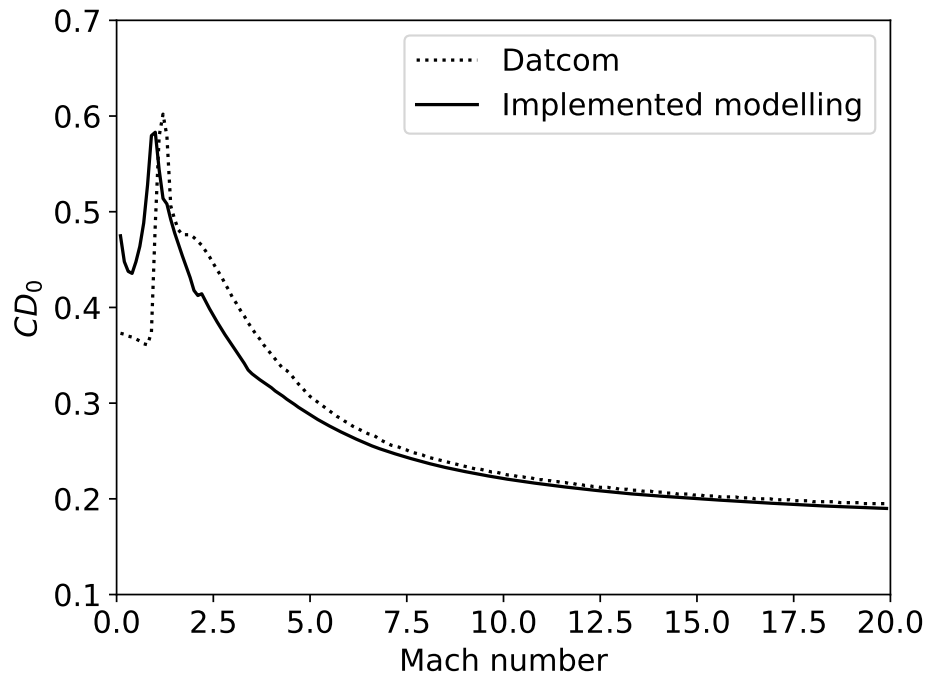
Figure 3.18: Verification zero angle of attack drag coefficient
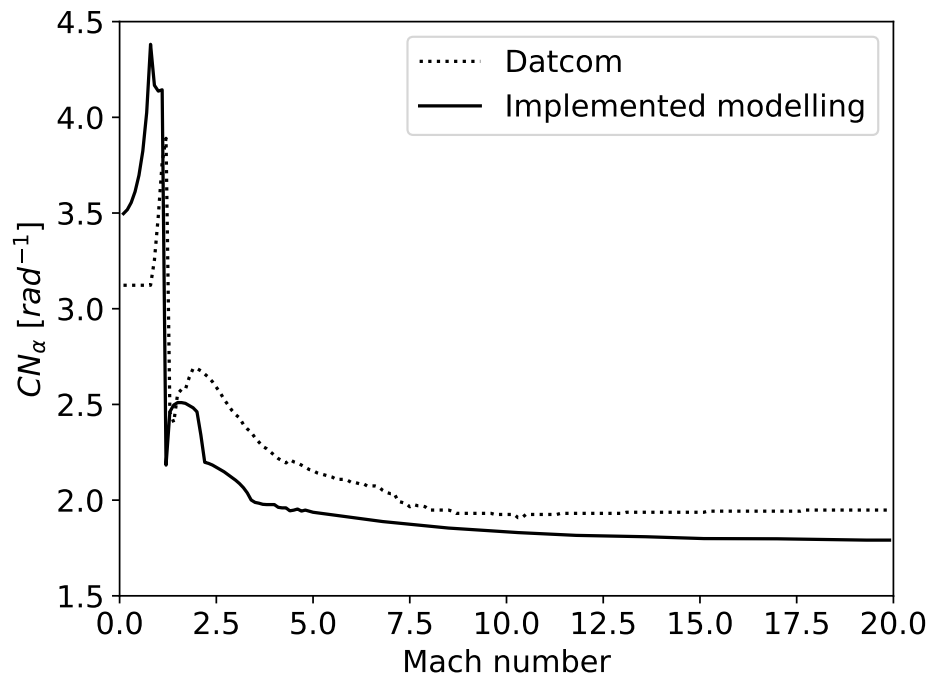
Figure 3.19: Verification zero angle of attack normal force coefficient derivative
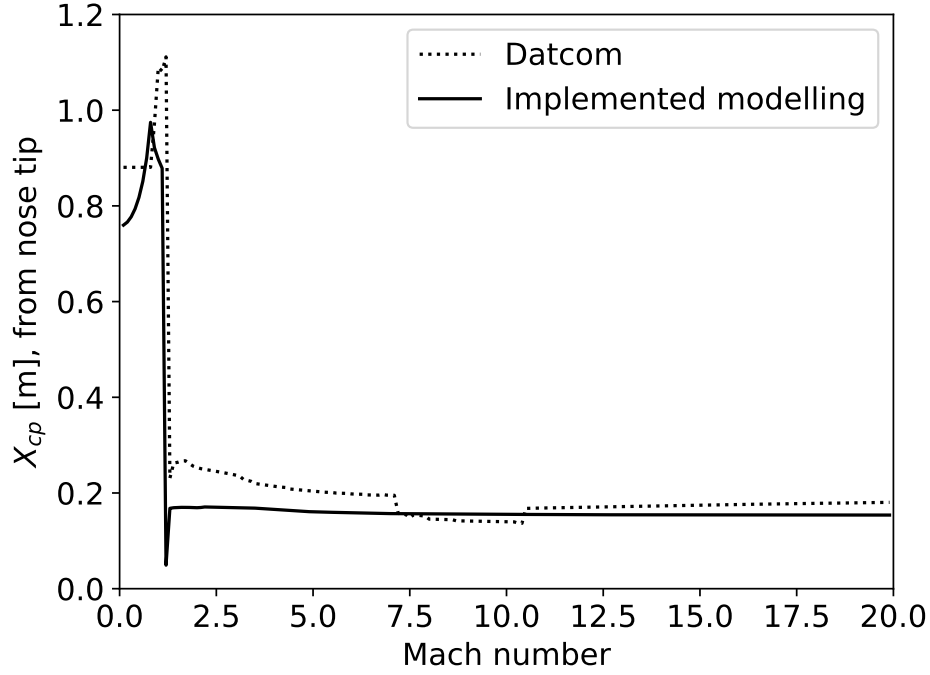
Figure 3.20: Verification zero angle of attack center of pressure

the vehicle can be considered a rigid body. In this investigation, modeling the translational motion will be sufficient for the preliminary design and analysis of vehicle trajectories as is done in similar works (Mota, 2015; Castellini, 2012). In the vehicle frame, a Cartesian, 3DOF formulation is used in determining flight loads and angular acceleration - which is assumed in the orbital/flight plane.

3.4.1 Equations of Motion

The equations of motion, adapted from Tewari (2007), are presented below. These equations describe the motion of a body (local horizontal reference frame) moving in a rotating reference frame. Both reference frames are non-inertial.

$$\dot{r} = v \sin \gamma \tag{3.55}$$
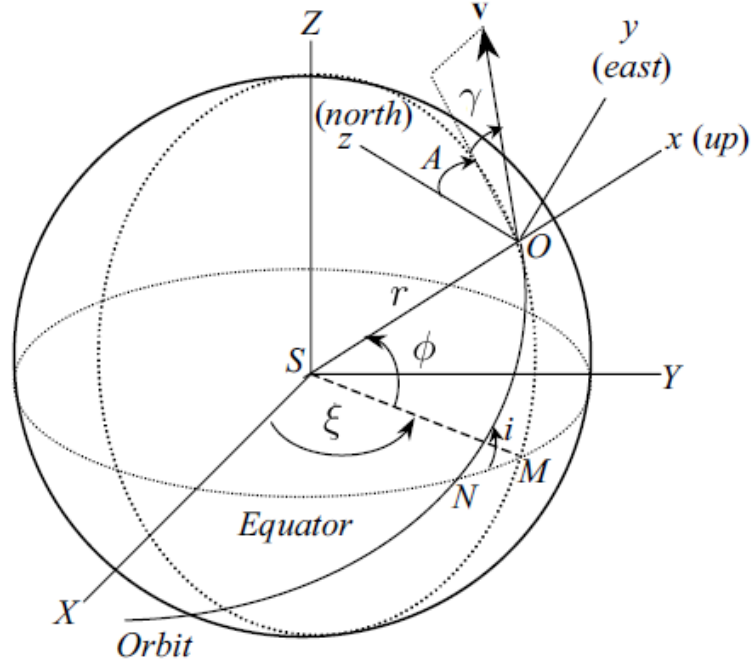
Figure 3.21: Earth centered and local horizontal reference frames, adapted from Tewari (2007).

$$\dot{\xi} = \frac{v \cos \gamma \cos \zeta}{r \cos \phi} \tag{3.56}$$

$$\dot{\phi} = \frac{v \cos \gamma \sin \zeta}{r} \tag{3.57}$$

$$\dot{\gamma} = \frac{\mathcal{T} \sin \beta_T + N}{mv} + \left(\frac{v}{r} - \frac{g(r)}{v}\right) \cos \gamma + \cos \phi \left[2\omega_E \cos \zeta + \frac{\omega_E^2 r}{v}(\cos \phi \cos \gamma + \sin \phi \sin \gamma \sin \zeta)\right] \tag{3.58}$$

$$\dot{v} = \frac{\mathcal{T} \cos \beta_T - D}{m} - g(r) \sin \gamma + \omega_E^2 r \cos \phi (\cos \phi \sin \gamma - \sin \phi \cos \gamma \sin \zeta) \tag{3.59}$$

$$\dot{\zeta} = -\frac{v}{r}\tan\phi\cos\gamma\cos\zeta + 2\omega_E(\cos\phi\tan\gamma\sin\zeta - \sin\phi) - \frac{\omega_E^2 r}{v\cos\gamma}\sin\phi\cos\phi\cos\zeta \quad (3.60)$$

where the mentioned variables are:

$\mathcal{T}$ - thrust $[N]$
D - drag $[N]$
N - normal force (lift) $[N]$
g - Earth's local gravitational acceleration $[\text{m/s}^2]$
ω_E - Earth's angular velocity $[rad/s]$
β_T - angle of thrust vector wrt. velocity vector, constrained to orbital plane $[rad]$
ϕ - latitude $[rad]$
ξ - longitude $[rad]$
A - azimuth $[rad]$
ζ - heading angle $(= \frac{\pi}{2} - A)$ $[rad]$
γ - flight path angle $[rad]$

3.4.2 Environment Modeling

Gravitational Model

The gravity is taken as function of planet radius. For Earth Eqn. 3.61 is used, with $\mu_E = 3.986004418 \times 10^{14}$ m^3 s^{-2} (Luzum et al., 2011).

$$g = \frac{\mu_E}{r^2} \quad (3.61)$$

Atmospheric Properties

The atmospheric properties: pressure and density, are taken from a quadratic interpolation of properties determined at an equal spacing of 100 m from -0.5 km to 86 km above sea level (ASL) (Fig. 3.22) of the 1976 US Standard Atmosphere (NOAA, 1976). The temperature is taken as linear interpolation at the same spacing. Linear interpolation for temperature was
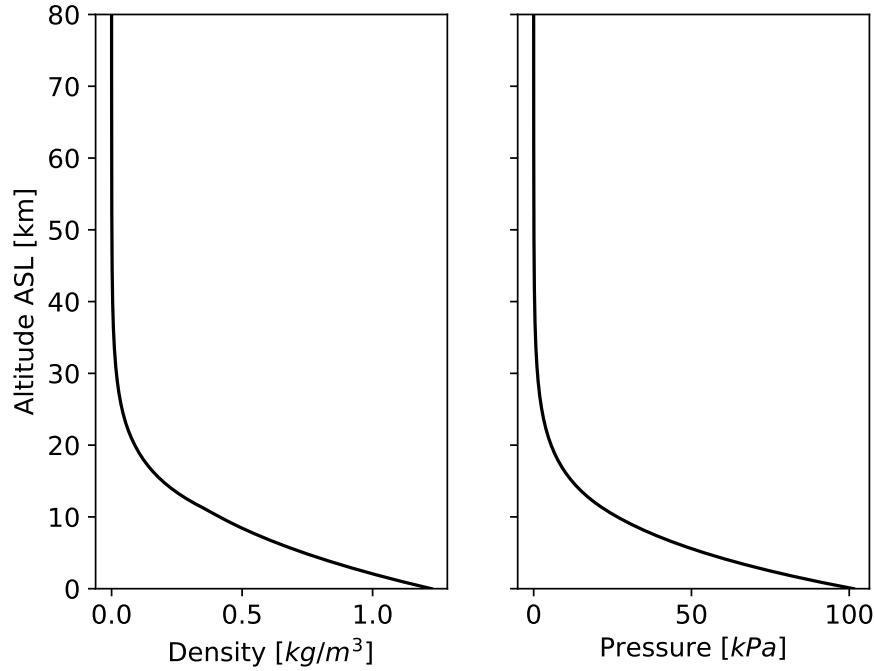
Figure 3.22: Air density and pressure at different altitudes above sea level

chosen due sharp cusps present in the temperature vs altitude relation. Dynamic viscosity is also taken as a linear interpolation since it is a strong function of temperature (Fig. 3.23).

Wind

The scalar wind profile envelope, synthetic wind profiles, and gust magnitude are determined using methodology outlined by Johnson and Vaughan (2000). The 99% scalar wind speed steady-state envelope is used from table 2-53 in (Johnson and Vaughan, 2000) for a representation of a generic launch site. To model a generic launch site, the envelope incorporated wind data from four common launch cites: Kennedy Space Center, Vandenberg Air Force Base, Edwards Air Force Base, and White Sands Missile Range. The envelope covers a potential worst-case steady-state wind speed. The wind gust variance is included and modeled as a discrete 9 m/s wind gust, possible at all altitudes. The gust is modeled to always increase angle of attack.
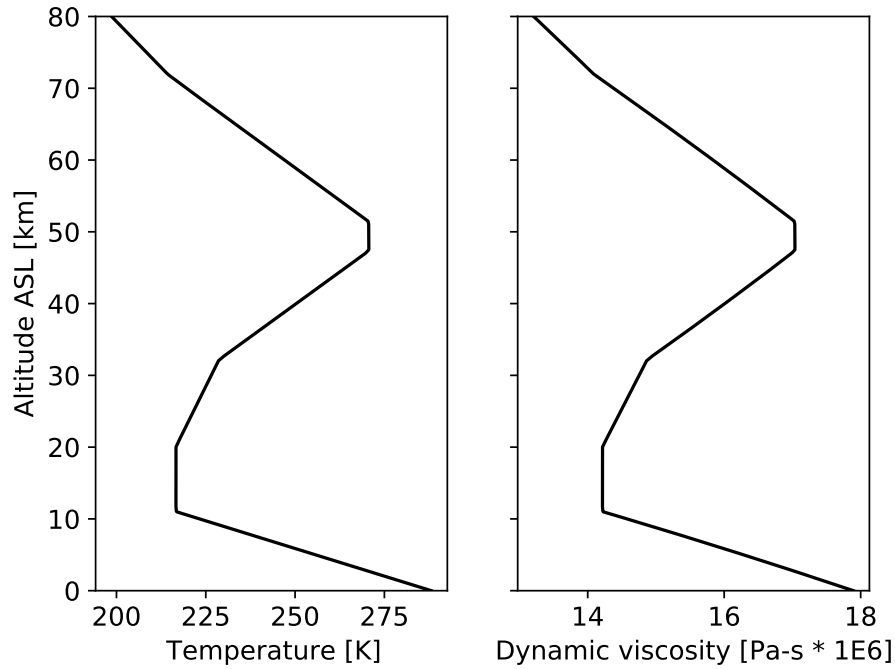
Figure 3.23: Air temperature and dynamic viscosity at different altitudes above sea level

The steady-state profile is not representative of an actual worst-case wind profile, but rather defines the maximum an actual wind profile could be at any given altitude. For a given flight simulation, a synthetic wind profile is constructed. The synthetic profile has two maximum wind locations defined from reference altitudes, with "build-up" and "back-off" profiles described by tabulated empirical data from Johnson and Vaughan (2000). The build-up and back-off profiles are wind speed rates of change with altitude which are a function of maximum wind speed. Table 2-72 and 2-73 from (Johnson and Vaughan, 2000) are used to construct the build-up and back-off of the synthetic wind profile for a given wind-speed at a reference altitude. Worst case reference altitudes of 12 km and 50 km are conservatively assumed as they would lead to largest winds. The steady-state wind profile and the chosen synthetic wind profile that the simulated rockets will experience are illustrated in Fig. 3.24.
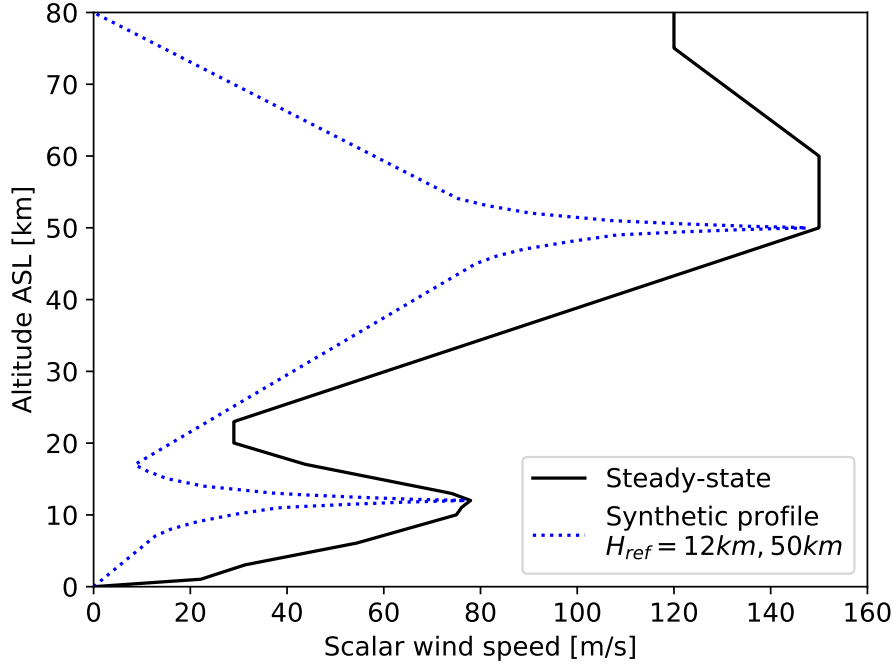
Figure 3.24: Scalar wind steady-state envelope with synthetic wind profile

3.4.3 Verification

The rotating spherical-Earth formulation, numerical integration, gravity, and atmospheric density have all been verified using data from Murri et al. (2015). The specific verification case used was a dropped sphere of constant drag coefficient above a rotating spherical Earth (Case 5). Sim number 02, 04, 05, and 06 data was available for comparison. The results of error in current altitude vs time is presented for all cases in Fig. 3.25. The error at 0.01 s time step is presented as it was used in all simulations. The final error is 0.25 m after the approximately 4000 m or 30 s simulation when compared to sims 04, 05 & 06. Simulation 02 appears to be outlying from the others and is not used for further comparison.

The atmospheric density, gravity, altitude, and longitude of the verification case are presented against sim 04 as sims 04, 05 & 06 were virtually identical. The local air density and gravity are shown to agree in Fig. 3.26. The simulated altitude history and longitude history show agreement with NASA sim-04 in Fig. 3.27.
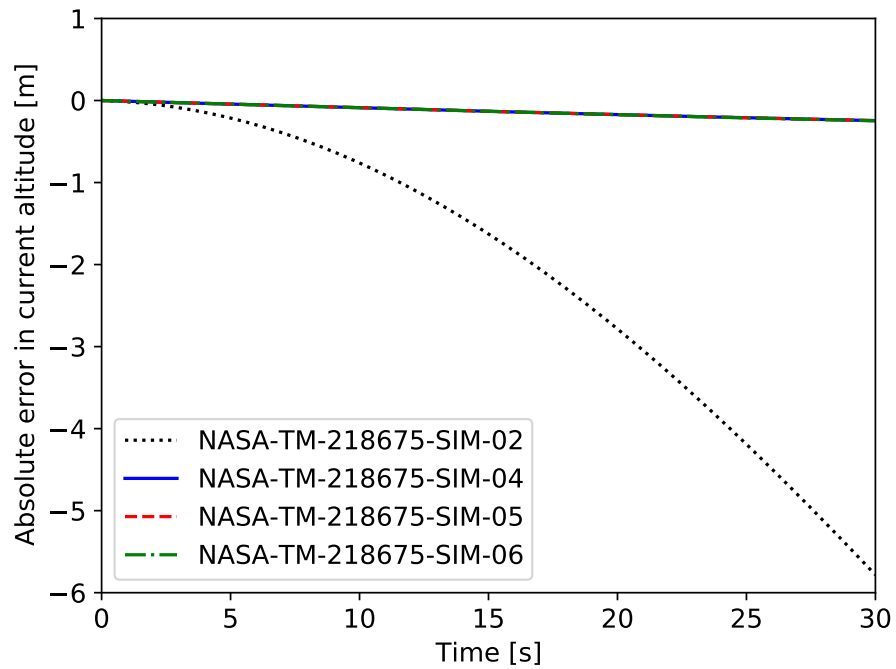
Figure 3.25: Absolute error in altitude for different flight test cases
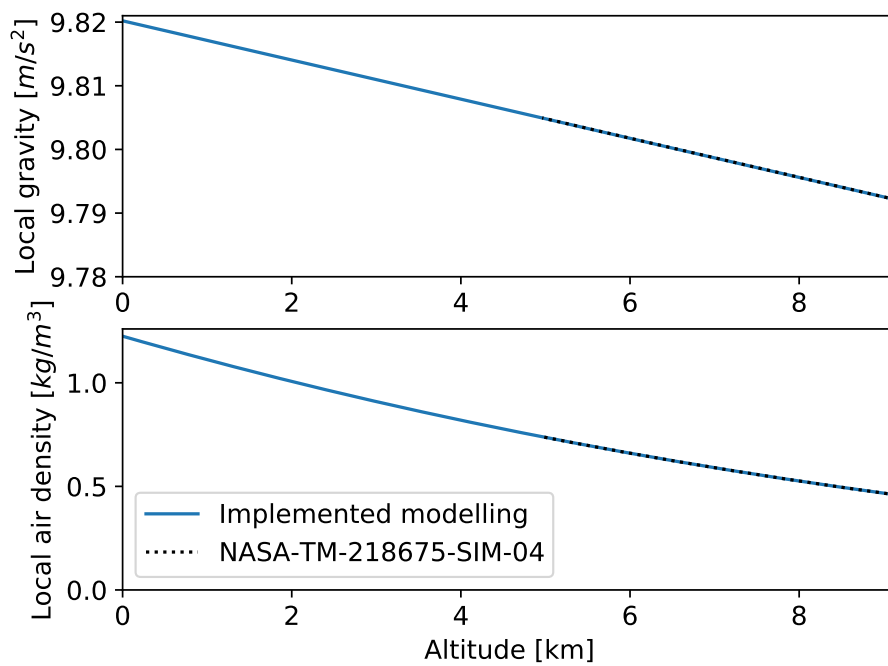
Figure 3.26: Local air density and gravitational acceleration comparison with NASA Sim-04
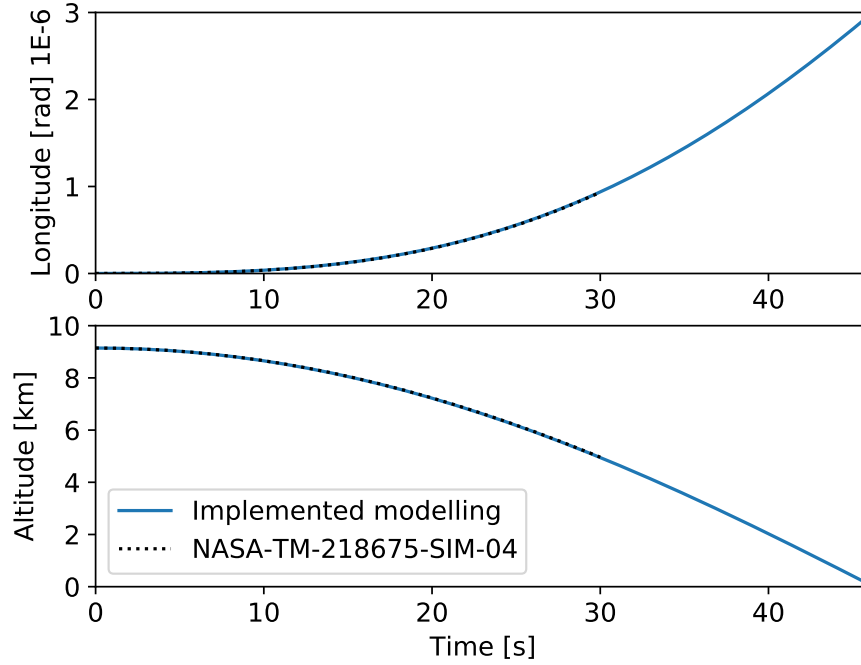
Figure 3.27: Simulated altitude and longitude comparison with NASA Sim-04

3.4.4 Trajectory

The trajectory is defined by an initial launch angle for sub-orbital sounding rockets. For two-stage rockets' orbital insertion and trajectory design and optimization, the trajectory consists of distinct phases: vertical liftoff, pitch over, gravity turn, bilinear tangent steering law, and a second-stage coast and re-light to circularize.

Once a simulated launch vehicle clears the tower (reaches a pre-defined altitude), it starts a pitch-over maneuver, down-range, to a specified pitch-over angle (γ_{po}). The pitch-over maneuver occurs before aerodynamic forces are large, and with a constant pitch rate. The vehicle then undergoes a gravity turn, where the only force altering the trajectory is due to Earth's gravity, and no maneuvers are performed that would induce an angle of attack and subsequent loads. Once staging occurs, typically outside of the denser portion of the atmosphere, a direct steering program is implemented for the upper stage: the bilinear tangent steering law. The bilinear tangent steering law dictates the flight path angle (γ) as

70

a function of time into the burn and can be found from Eqn. 3.62, adapted from Castellini (2012). The The flight path heading rate of change can also be determined at this stage and used as set points for a controller. The controller would apply torques to the vehicle to impart angular acceleration/velocity either using gas thrusters or TVC. Defining the flight path heading at time into the flight, or burn, with some tune-able parameters or control points is done in most works surveyed (Castellini, 2012; Mota, 2015; Miranda, 2015; Woodward, 2017). The control system for controlling flight path heading (i.e solving equations of motion in vehicle frame with lateral thrust imparting error corrections) was neglected in this thesis to increase computational speed, Castellini (2012) found that very small steering losses were found when including the upper stage steering control into the simulation. Neglecting the steering control modeling is typically done in other works (Miranda, 2015; Woodward, 2017). Steering is however incorporated into the simulation of the first stage ascent to determine loads and first stage steering losses.

$$
\gamma = \begin{cases} \tan^{-1}\left(\frac{c^{\chi}\tan\gamma_i + (\tan\gamma_f - c^{\chi}\tan\gamma_i)\frac{\tau_b}{b}}{c^{\chi} + (1 - c^{\chi})\frac{\tau_b}{b}} \right) & 0 \leq \tau_b \leq b \\ \gamma_f & \tau_b > b \end{cases}
\tag{3.62}
$$

where,

γ - flight path angle $[rad]$
γ_i - initial flight path angle at beginning of control $[rad]$
γ_f - final flight path angle (typically 0, tangent to Earth's surface) $[rad]$
c - fitting parameter to control trajectory shape, $10 \leq c \leq 100$
χ - fitting parameter exponent to control trajectory shape, $-1.0 \leq \chi \leq 1.0$
τ_b - normalized burn time, $0.0 \leq \tau_b \leq 1.0$
b - normalized burn time truncation parameter, $0 < b \leq 1.0$

The current flight path angle (γ), in the flight path plane, is controlled to match that defined by Eqn. 3.62 at each instant of the burn time. The parameter τ_b is the normalized burn time, c and χ are constants defining the shape of the trajectory. The γ_i and γ_f variables are the initial and final flight path angles respectively. The initial flight path angle of the

second stage is determined by the flight profile of the first stage. The final flight path angle is 0 rad (tangent to the Earth's surface).

During the first stage burn, before Second-Engine Cut-off, number one (SECO-1), the resulting orbit (if the engine was to be cut-off) is continuously calculated at each time step. When the calculated orbit apogee reaches the target apogee at the current altitude (perigee), the burn is truncated. The Python module orbitalpy (McLean, 2020) is used to calculate the orbital elements from the state vector (position and velocity in 3D space). The six arguments of a position and velocity vector are translated into six Keplerian elements that define the orbit geometry in space (Vallado, 2010) where the apogee and perigee can be extracted. The initial orbit at SECO-1 is elliptical, the final circular orbit is accomplished by a circularization burn on the opposite side of the Earth. However, the actual time marching does not persist around the Earth in the simulation to increase computational speed. The required propellant mass at the average remaining deliverable I_{sp} is calculated using the rocket equation (Eqn. 3.1) since the equation's assumptions are valid in this case. An impulsive-thrust orbit transfer is assumed for the in-orbit revenuers which is valid for typical chemical rockets since the burn times are small fractions of total orbit times (Vallado, 2010). The required propellant is checked with the available propellant mass. The ΔV residual is converged to zero in the global optimizer. The ΔV residual is also allowed to go negative and be converged to zero or positive by the global optimizer to provide a better gradient in the solution space.

Trajectory Optimization and Convergence

The required position (radius) and velocity vector of the vehicle in an inertial reference frame, at SECO-1, is prescribed by the desired orbit (Vallado, 2010). The trajectory design consists of two parts: meeting required orbit parameters and minimizing the propellant usage. The trajectory design is multi-objective and consists of solving a boundary-value problem, where the trajectory parameters are adjusted such that the final solution matches

that desired, while also minimizing propellant usage. The trajectory design and optimization is accomplished through numerous flight simulations. If the trajectory design was to be coupled with the structural design the number of required flight simulations would greatly increase. The trajectory was desired to be decoupled from the structural analysis of the vehicle to reduce the run time of complete design iterations. The solution decouples the trajectory designs of the stages. The first-stage ascent trajectory is completely defined by a pitch-over/gravity turn (γ_{po}), the structures can be converged to their optimal values, through least squares, including the upper stage since maximum loading occurs during first-stage ascent. The structures of the upper stage are then assumed independent of the upper stage trajectory, which is a reasonable assumption as staging is typically done near negligible dynamic pressure. A more detailed description of the structural design is completed in the structural design section. The upper stage trajectory flight segment can then be optimized, at a local level, by altering the available parameters that define its trajectory (c, χ, and b).

The cost function that was used to optimize upper stage trajectories is the error of the SECO-1 altitude from the target, minus the ΔV of the remaining propellant residual on board after circularization. The optimizer seeks to minimize the cost function. The ΔV is calculated using Eqn. 3.1, the remaining average vacuum specific impulse, and known remaining propellant and inert masses.

The algorithm that was found to quickly and reliably converge on optimal upper stage trajectories is the L-BFGS-B algorithm in the Scipy Optimize module minimize function (Virtanen et al., 2020). The L-BFGS-B algorithm is chosen as this problem is non-linear. The limited memory (L-), bounded (-B) BFGS algorithm is in the class of quasi-Newton's method and is found to quickly converge to optimal trajectory parameters compared to other non-linear methods available in the Optimize module. The good performance is attributed to the smoothness of the objective function, and short bounds on the parameters. The algorithm has a narrow search space and only three dimensions and finds optimal solutions reliably and quickly.

3.5   Structural Design

3.5.1   Propellant Tanks

The design of the propellant tanks (oxidizer tank and combustion chamber) is an important aspect to consider as the launch vehicle's performance is sensitive to inert mass, and the propellant tanks naturally contribute are a large portion of inert mass. The specification of a pressure vessel is accomplished given tank material, pressure, outer diameter, and volume requirements, with the use of thin-walled pressure vessel theory (Young et al., 2011). In this study, the oxidizer tank outer diameter is equal to the vehicle outer diameter. The choice of a single structure is made to avoid redundant structures and increase mass-efficiency.

In thin-walled theory, the stress variation across the thickness of the vessel is neglected, for vessels with $r/t < 10$, this manifests to less than 5% error in the final state of stress (Young et al., 2011). The hoop and axial stresses are presented in Eqn. 3.63 and 3.64. The stress derivation assumes a thin circular-cylindrical section, subject to internal pressure, in static equilibrium.

$$\sigma_{hoop} = \frac{Pr}{t} \tag{3.63}$$

$$\sigma_{axial} = \frac{Pr}{2t} \tag{3.64}$$

Theses two stresses represent principal stresses in the material. With the knowledge of the material and its failure mode, a failure criteria can be chosen. Common failure criterion for ductile materials include Tresca or von Mises (Young et al., 2011).

The von Mises criteria is defined by Eqn. 3.65 with principal stress values:

$$\sqrt{\frac{(\sigma_1 - \sigma_2)^2 + (\sigma_2 - \sigma_3)^2 + (\sigma_3 - \sigma_1)^2}{2}} = \sigma_y \tag{3.65}$$

The failure criteria for thin-walled pressure vessels using von Mises criteria is presented

in Eqn. 3.66:

$$\sqrt{\frac{(\frac{Pr}{t} - \frac{Pr}{2t})^2 + (\frac{Pr}{2t} - 0)^2 + (0 - \frac{Pr}{t})^2}{2}} = \frac{\sqrt{3}}{2}\frac{Pr}{t} = \sigma_y \tag{3.66}$$

The predicted failure stress given by von Mises stress will be used here and must be re-evaluated if different materials used have different failure mechanisms/criteria.

Flat plates, semi-ellipsoids, and semi-spheres were investigated as potential end caps of the pressure vessels. Flat end caps are length efficient and useful for small scales. Hemispheres have the best mass-efficiency but are the least length efficient since the attachment point of adjacent sections is typically at the cylindrical section of the vessel. Longer inter-tank structural sections may result in global reduction in mass-efficiency. Ellipses are typically employed on most launch vehicles as there can be a trade between end cap mass and coupling section mass/length.

For spherical end cap walls, both principal stresses are equal and the von Mises critera becomes Eqn. 3.67:

$$\frac{Pr}{2t} = \sigma_y \tag{3.67}$$

For flat plates, with clamped edge boundary conditions, the maximum stress occurs in the radial direction at the edge of the plate (Young et al., 2011). This stress is equated to tensile yield for a failure criteria (Eqn. 3.68).

$$\frac{3P}{4}\left(\frac{r}{t}\right)^2 = \sigma_y \tag{3.68}$$

The derivation of the von-Mises stress for a general ellipsoid head can be found in (Wildvank, 2018). The result is presented in Eqns. 3.69 - 3.73. The coordinate system and elliptical parameters a and b are shown graphically in Fig. 3.28.

$$\frac{P}{t}\sqrt{A^2 - AB + B^2} = \sigma_y \tag{3.69}$$
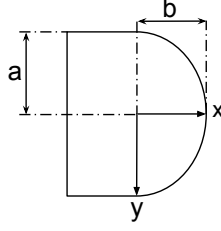
Figure 3.28: Elliptical pressure vessel head coordinates

$$A = \frac{R_1}{2} \tag{3.70}$$

$$B = R_1(1 - \frac{R_1}{2R_2}) \tag{3.71}$$

$$R_1 = \frac{\sqrt{a^4x^2 + b^4y^2}}{b^2} \tag{3.72}$$

$$R_2 = \frac{(a^4x^2 + b^4y^2)^{3/2}}{a^4b^4} \tag{3.73}$$

Propellant-tank-to-fluid Mass Ratio

The propellant tanks, as discussed, constitute a large portion of volume/mass of the entire structure. The large contribution to the vehicle dry mass makes it worthwhile to have a digression to investigate the tank-alone mass scaling, specifically the tank-to-propellant mass ratio. The mass ratio of the entire vehicle is a common parameter to quantify structural efficiency; it is famously shown in the Tsiolkovsky rocket equation (Eqn. 3.1).

Neglecting the mass of the tank end caps, the propellant-tank-to-fluid mass ratio is calculated with Eqn. 3.74. The method assumes the biaxial stress state from thin-walled pressure vessel theory.

$$\frac{m_{fluid}}{m_{tank}} = \frac{\rho_{fluid}V_{fluid}}{\rho_{tank,material}V_{tank,material}} \approx \frac{\rho_{fluid}\pi r^2 L}{\rho_{material}2\pi r t L} = \frac{\rho_{fluid}\pi r^2 L}{\rho_{material}\sqrt{3}\pi r \frac{Pr}{\sigma_{allow}}L} = \frac{\rho_{fluid}\sigma_{allow}}{\sqrt{3}\rho_{material}P}$$

$$(3.74)$$

Equation 3.74 shows, with the previously stated assumptions, that the mass ratio can only be altered by the density of the fluid contained, the pressure it's stored at, and the strength-to-weight ratio of tank material. The propellant-to-tank mass ratio is not a function of geometry (scale).

The theoretical scaling mass ratio is compared to a design of a spherical-capped oxidizer tank for different internal volumes. The vessel outer diameter was 1.0 m and the volume was ranged from 0.6 m^3 to 80 m^3. The internal pressure and fluid density was 300 kPa and 1000 kg/m^3 respectively. The material density and allowable stress was 2700 kg/m^3 and 120 MPa respectively. The design and theoretical scaling mass ratios are presented in Fig. 3.29. The minor discrepancy observed, at the largest aspect ratios, is attributed to assuming the tank cross-sectional area is the circumference multiplied by thickness in the theoretical scaling estimate.

3.5.2 Combined Loading

In general, for a rocket cylindrical section considered here, loading can occur in the forms of: axial force, bending moment, and internal pressure (Fig. 3.30). The vehicle weight, in addition to thrust which is reacted by inertial loads, and drag, provide the net axial force (F_{ax}). The pure axial stress is expressed with the net axial force: $\sigma_{ax} = \frac{F_{ax}}{A}$. Bending loads arise from lateral forces due to the vehicle response to angle of attack, lateral components of body forces, and thrust vectoring. The maximum/minimum bending loads occur on opposite sides of the neutral axis: $\sigma_b = \pm\frac{Mr}{I}$. The parameter I is the sectional area moment of inertia; values are from Young et al. (2011). Variable A is cross-sectional area of the thin cylindrical section. Stress from internal pressure are expressed by Eqns. 3.63 and 3.64.
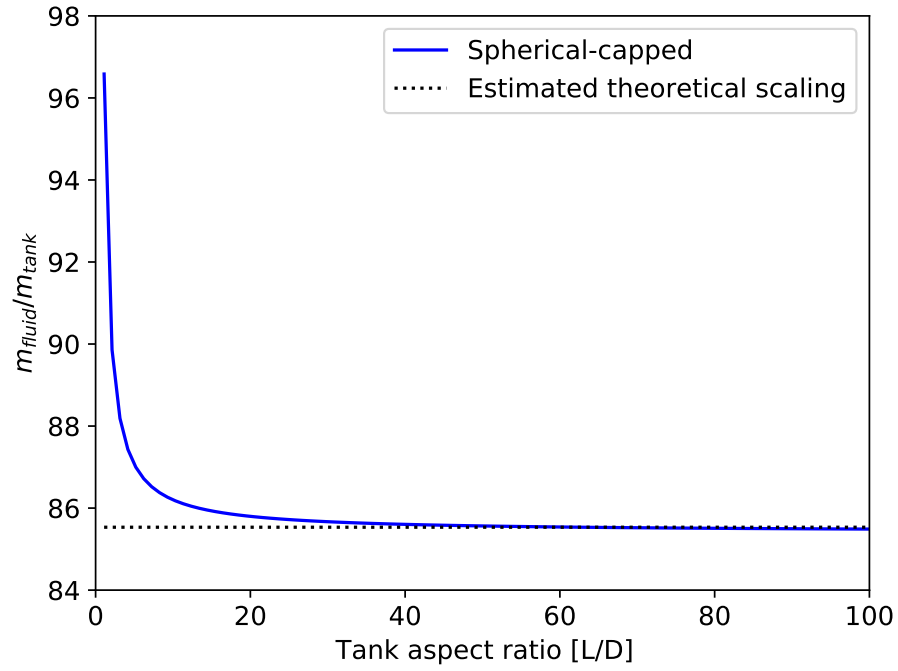
Figure 3.29: Comparison of oxidizer tank design mass to theoretical scaling estimate
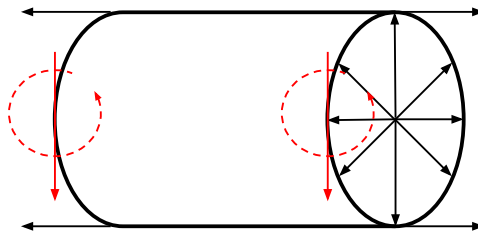
Figure 3.30: Axial, lateral, bending moment, and internal pressure loads on a generic rocket element cylinder

The combined von-Mises stress can be calculated using Eqn. 3.65 for two 2-D stress elements at the maximum and minimum bending stress locations. The first principal stress is the sum of the axial, bending, and axial internal pressure stress (see Eqn. 3.75). The second principal stress is the hoop stress due to internal pressure (Eqn. 3.76).

$$\sigma_1 = \frac{F_{ax}}{A} \pm \frac{Mr}{I} + \frac{Pr}{2t} \tag{3.75}$$

$$\sigma_2 = \frac{Pr}{t} \tag{3.76}$$

3.5.3 Buckling of Thin-walled Cylinders

This section will analyze all of the combined loads and link to buckling failure of thin cylindrical shells. The thin isotropic circular cylinder failure criterion under axial compression, bending, and internal pressure is used from NASA TR-SP-8007 (Peterson et al., 1968). Isotropic circular cylinders are assumed for each rocket component. Buckling and collapse coincide for circular cylinders under both axial compression and bending (Peterson et al., 1968).

The critical axial stress for a thin cylinder buckling failure is represented by Eqn. 3.77. Note that respectively variables t and r are cylinder thickness and radius. E and μ are the material Youngs Modulus and Poisson ratio. The variable γ_x is the empirical correlation factor to account for differences between the theory and predicted instability loads, specifically for axial compression. The variable γ_x is determined from Eqns. 3.78 - 3.79:

$$\sigma_{x,crit} = \frac{(\gamma_x + \Delta\gamma)E}{\sqrt{3(1-\mu^2)}} \frac{t}{r} + \frac{Pr}{2t} \tag{3.77}$$

where $\Delta\gamma$ ranges between 0.02 and 0.2, is a function of pressure, and is taken from figure 6 in (Peterson et al., 1968). As well, note the following:

$$\gamma_x = 1 - 0.901(1 - e^{-\Phi}) \tag{3.78}$$

$$\Phi = \frac{1}{16}\sqrt{\frac{r}{t}}, \left(\frac{r}{t}\right) < 1500 \tag{3.79}$$

Peterson et al. (1968) warn that predictions of critical load past length-radius ratios greater than 5.0 have not been validated by experiments. Critical loads for bending are given by a different correlation factor, γ_b, Eqn. 3.80. The bending correlation factor can be used similarly in Eqn. 3.81 to obtain the critical maximum stress in bending. An 80 % factor is applied to the collapse resistance theoretically supplied by internal pressure as per NASA TR-SP-8007.

$$\gamma_b = 1 - 0.731(1 - e^{-\Phi}) \tag{3.80}$$

$$\sigma_{b,crit} = \frac{(\gamma_b + \Delta\gamma)E}{\sqrt{3(1 - \mu^2)}}\frac{t}{r} + 0.8\frac{Pr}{t} \tag{3.81}$$

The interaction of the two stresses for predicting failure is given in Eqn. 3.82. The ratio, R_x, is the ratio of the axial stress in a cylinder subjected to more than one type of loading to the allowable stress in the cylinder subjected to only axial compression. R_b is ratio of stress due to bending in the combined scenario to the allowable bending-alone stress.

$$R_x + R_b = \frac{\sigma_x}{\sigma_{x,allow}} + \frac{\sigma_b}{\sigma_{b,allow}} \leq 1 \tag{3.82}$$

3.5.4 Flight Loads

The axial and transverse loads that the rocket experiences in flight are generally caused by: body forces (inertial and gravitational), aerodynamic forces (lift and drag), and thrust forces (axial from the principal thrust delivery system, and transverse from thrust vector control

(TVC)). The considered loads are combined into resultants at element center of mass and pressure. The forces are then decomposed into axial forces, lateral shear forces, and bending moments at the element interfaces (nodes) along the axial length of the rocket.

At each instant in flight, the loads are calculated assuming the current wind is the highest possible as outlined by the steady-state 99 % envelope, in the environmental modeling section, in addition to a discrete sharp-edged gust. The first-stage engine(s) lateral thrust from the available TVC is used to trim the vehicle against the aerodynamic loads, to create a zero moment about the center of mass. The act of trimming can potentially create a large bending stress on the vehicle. The additional gust is assumed to occur over a short time and creates a worst-case dynamic response and loading situation for the vehicle. The actual synthetic wind profile used in flight simulations is not the same one used to determine maximum possible loads, and is defined in the environmental modeling section. The synthetic profile is used mainly in quantifying the steering losses and effect of wind on the trajectory.

During the dynamic response, angular acceleration and lateral acceleration contribute to inertial loads and relief, however aerodynamic plunge and pitch damping are neglected. The axial, shear, and bending moment equations have been derived with the nosecone tip as the origin. Bending moment, shear, and axial loads vanish at the free ends, if none are prescribed there, and the successive loads can be determined by marching in space down the length of the rocket vehicle.

The shear force, S, acting on the face of a rocket element can be determined using Newton's 2nd law in the lateral (y) direction (Eqn. 3.83):

$$S_{i+1} = S_i + m_i(a_y - (x_{cg} - x_{cg,i})\frac{d^2\gamma}{dt^2}) + qA_{ref}C_{N\alpha,i}\alpha \qquad (3.83)$$

where q is the dynamic pressure.

The x_{cg} is the axial location of the center of gravity, measured from the nosecone tip (Eqn. 3.84). The subscript i denotes element quantities. Element center of mass/gravity $x_{cg,i}$ is measured from the element front:
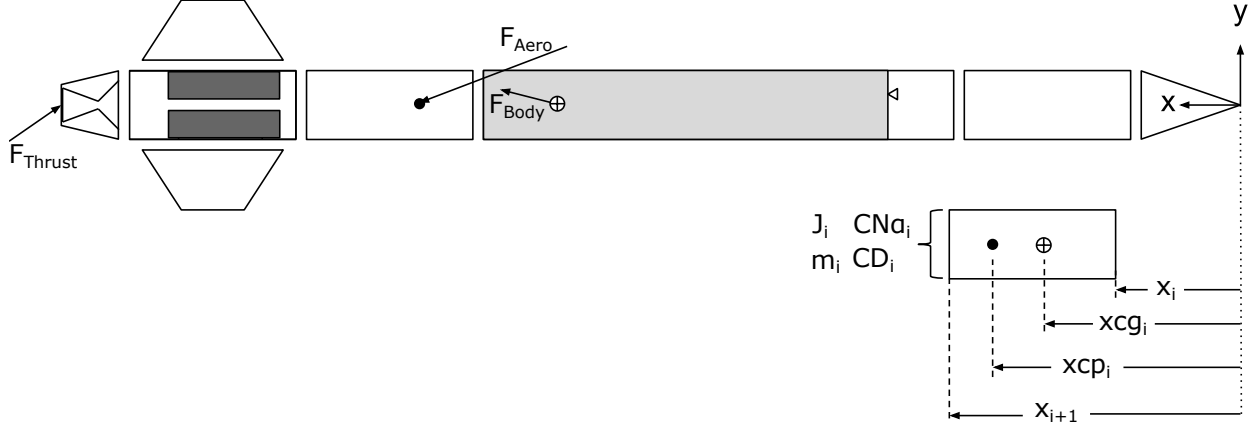
Figure 3.31: Rocket element-by-element load formulation

$$x_{cg} = \frac{\Sigma m_i x_{cg,i}}{\Sigma m_i} \tag{3.84}$$

The acceleration in the lateral direction and angular acceleration can be determined for the rigid-body using Eqn. 3.85 and Eqn. 3.86:

$$a_y = \frac{-qA_{ref}\alpha\Sigma C_{N\alpha,i} + \mathcal{T}\sin\beta_T}{\Sigma m_i} + g\cos\gamma \tag{3.85}$$

$$I_L\frac{d^2\gamma}{dt^2} = qA_{ref}\alpha\Sigma[C_{N\alpha,i}(x_{cg} - x_{cp,i})] - \mathcal{T}\sin\beta_T(x_{cg} - x_{TVC}) \tag{3.86}$$

I_L is the longitudinal moment of inertia (Eqn. 3.87):

$$I_L = \Sigma[J_i + m_i(x_{cg} - x_{cg,i})^2] \tag{3.87}$$

The bending moments at the boundaries of the elements can be determined from a moment balance at $x_{cg,i}$ of each element (Eqn. 3.88):

$$M_{i+1} = M_i + S_i(x_{cg,i} - x_i) + S_{i+1}(x_{i+1} - x_{cg,i}) + qA_{ref}C_{N\alpha,i}\alpha(x_{cg,i} - x_{cp,i}) - J_i\frac{d^2\gamma}{dt^2} \tag{3.88}$$
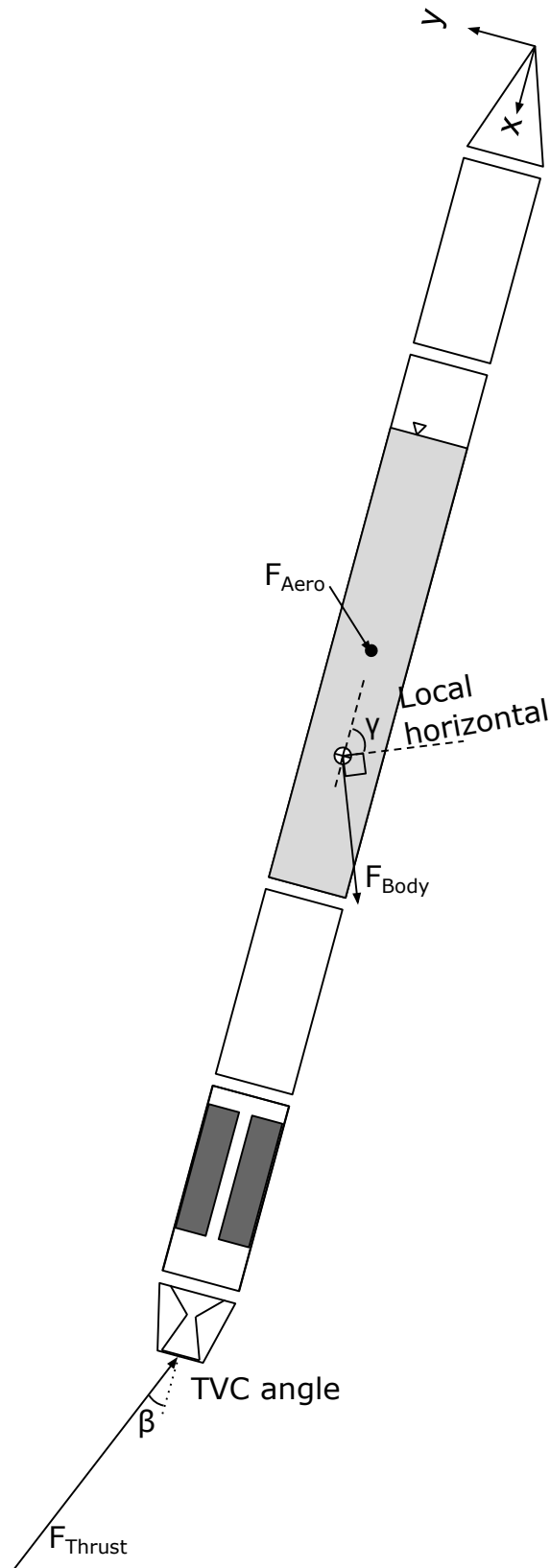
Figure 3.32: Rocket global free-body diagram

The axial loads can be determined from applying Newton's 2nd law in the longitudinal (x) direction (Eqn. 3.89):

$$F_{i+1} = F_i + m_i a_x + q A_{ref} C_{D,i} \tag{3.89}$$

where a_x is the longitudinal (x) acceleration (Eqn. 3.90):

$$a_x = \frac{(\mathcal{T} \cos \beta_T - q A_{ref} \Sigma C_{Di})}{\Sigma m_i} - g \sin \gamma \tag{3.90}$$

The boundary conditions are prescribed by Eqn. 3.91:

$$S_0 = 0, M_0 = 0, F_0 = 0, S_n = \mathcal{T} \cos \beta_T, F_n = \mathcal{T} \sin \beta_T \tag{3.91}$$

3.5.5   Special Load Cases

A few special load cases are added to size various elements:

- **Loss of pressure on-pad**

    The load case of a depressurized vehicle on the pad is analyzed. This is employed after realizing that the optimizer was exploiting pressure-stabilized structures that could not support their own weight if pressure was lost. All masses onboard are the starting values (full propellant loading, worst case), but all propellant tanks have zero pressure. This load case ensures the buckling margins of the oxidizer tanks are sufficient for a zero thrust, on-pad case. The loss of pressure in-flight may have insufficient margins if thrust can still occur when the tanks are not pressurized.

- **Aft engine section skirt axial compression from vehicle weight on-pad**

    This load case checks the aft section around the main engines while bearing the total vehicle weight in compression, statically on the launch pad. This is in addition to all flight loads.

- **Upper stage flight loads**

  The lateral loads on the second stage are neglected during the flight of the second stage. It is assumed that all contributing factors to lateral loads are small for the upper stage's flight. The upper stage's lateral loads are still calculated during the first-stage ascent, when both stages are connected. This assumption requires validation once the full mission simulation is performed or can be maintained with a minimum staging altitude constraint. The assumption of negligible lateral loads results in being able to determine the upper stage flight loads outside of the upper stage flight loop, which drastically reduces computational time. The maximum axial loads and maximum fluid static pressure are calculated for upper stages assuming zero back pressure for the propulsion system, and aligned velocity and gravity vectors (worst case).

3.5.6 Modal Analysis

The displacement/stiffness constraints are another important aspect of the launch vehicle's structural design. The stiffness requirements are based on a modal (frequency domain) analysis of a finite-beam-element model of a rocket. The rocket model is divided into discrete elements, the same elements as previously discussed, each with geometric, mass, and material properties. The stiffness constraints are the lowest allowable bending and axial mode fundamental vibrational frequencies. The fundamental modes increase in frequency value as overall rigidity is increased. The values of lower bounds are 25 Hz and 10 Hz for axial and bending modes respectively, taken from launch vehicle design criteria and based on previous existing launchers from Larson and Wetrz (1999). The rigidity constraints are important for maintaining control stability and avoiding any aeroelastic instabilities, that could lead to high fatigue loading or divergence.

In the modal analysis formulation, each rocket element is modeled as a cylinder with uniform mass distribution. The mass and stiffness matrices are determined for each element based on Bernoulli-Euler beam theory (Gavin, 2018). A single element mass matrix and
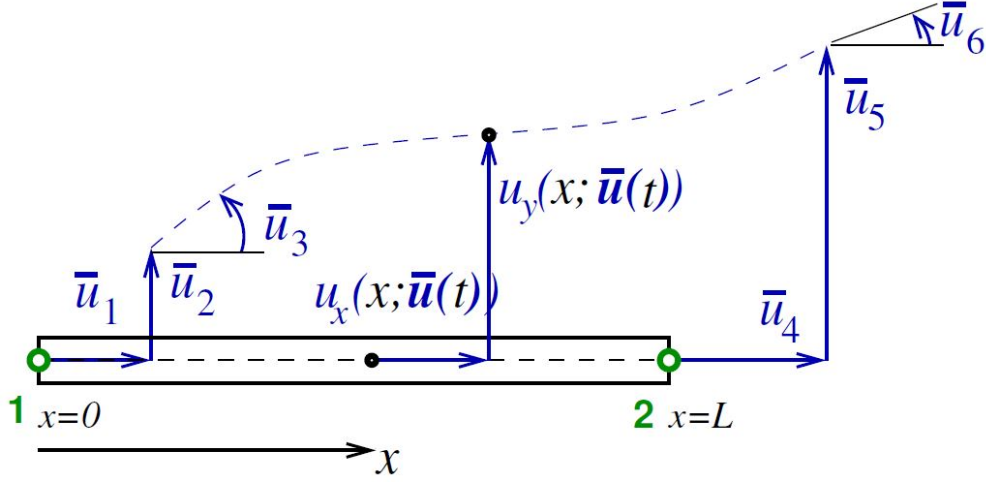
Figure 3.33: Beam element coordinates, from Gavin (2018)

stiffness matrix are shown in Eqn. A.1 and Eqn. A.2 respectively in the appendix. The row/column number in the mass and stiffness matrices correspond to a left or right node with one of the three degrees of freedom as outlined in Table 3.5. The corresponding coordinate system and degrees of freedom for a single beam element is shown in Fig. 3.33. The section properties, area-moment of inertia (I) and cross-sectional area (A), are easily calculated for the thin cylindrical circular sections. The global stiffness and mass matrices are constructed from all local element matrices. The non-trivial solutions of the eigenequation for the finite element model of the rocket can be solved, and fundamental modes can be quantified, when the condition of Eqn. 3.92 is met, where $[\mathbf{K}]$ is the global stiffness matrix and $[\mathbf{M}]$ is the global mass matrix.

$$det([\mathbf{K}] - \omega^{\mathbf{2}}[\mathbf{M}]) = \mathbf{0} \tag{3.92}$$

The axial and bending modes were considered separately and the two eigenvalue problems were separately solved, one with longitudinal stiffness matrix and one with lateral stiffness matrix. The decoupled methodology was used such that the calculated modes could be easily compared to the existing criteria. A 0.0 Hz mode was present for the longitudinal and lateral directions, which implies rigid body motion, this was due to the free-free boundary

Row/column index	Node	Direction
0	left	axial
1	left	lateral
2	left	angular
3	right	axial
4	right	lateral
5	right	angular

Table 3.5: Element matrix information

conditions imposed. The lowest non-zero values were used as the first fundamental modes of vibration.

The outlined method of calculating the fundamental modes using Bernoulli-Euler beam theory was verified using a fixed-free (cantilever) beam fundamental mode prediction equations from Roark's Formulas for Stress and Strain (Young et al., 2011). The equation from Roark's was for a beam with uniform mass distribution. The derivation of the equation in Roark's handbook could not be found. A constant relative error of 10.3 % was found for the axial vibration fundamental mode, and the error did not change when any of the beams properties were altered. The lateral fundamental frequency relative error was a constant 0.40 % and was constant for any variation in beam properties. The methodology is consistent despite the constant relative error; the root cause of the error is not apparent.

3.5.7 Materials

The majority of the structural elements (body elements/oxidizer tanks) used a high strength-to-weight aluminum alloy: 2024-T6. The 2024-T6 alloy is used in aerospace applications and is similar in strength-to-weight ratios to other high-performing aluminum alloys (Moser, 2003). Material properties for 2024-T6 are taken from Genevois et al. (2006). Pressurant tanks and combustion chambers are modeled to have Ti-6Al-4V material properties. The Ti-6Al-4V titanium alloy is also found in Moser (2003) as a higher-cost but very high strength-to-weight ratio material. Material properties for Ti-6Al-4V are taken from Karolewska and Ligaj (2019). The nozzle converging-diverging structure was modeled as iridium-coated

rhenium (Ir/Re) (Reed et al., 1997) which was investigated for radiatively-cooled rocket nozzles and had readily available material property data. All used material property data, from the mentioned references, is provided in Table 3.6.

Name	ρ [kg/m^3]	σ_y [MPa]	E [GPa]
2024-T6	2780	345	73.1
Ti-6Al-4V	4429	880	96.9
Ir/Re	21 000	300	N/A

Table 3.6: Material properties of rocket structures

3.5.8 Structural Analysis Program Sub-routine

During the simulations, the structure wall thicknesses are sized incorporating the stresses incurred mid-flight along with all internal stresses. However, since the flight performance is affected by the dry mass, determining the structure thicknesses requires an iterative process. Fortunately, for the structural design problem of only several wall thickness optimization variables, a linear least squares optimization is found to converge on optimal (minimal) structures relatively quickly using gradient-based methods.

An overview of the structural design sub-routine is presented in Fig. 3.34. During the structural analysis, the buckling/yield safety margins are first converged to the target margins by altering all section wall thicknesses through flight simulation iterations using a linear least-squares error minimization. The flight simulations performed in the structural design loop are modified, where the time step in the numerical simulation is 0.5 s. The time step was reduced until error in any vehicle safety factors changed by less than 1 %. The linear least squares error minimization uses the numerical derivative of the cost (error) function with respect to each thickness variable using a Trust Region Reflective algorithm which was analyzed as the most robust/fastest method available in the Scipy Optimize Python module *least_squares* function (Virtanen et al., 2020).

After the buckling/yield requirements are met, the fundamental mode constraints are assessed. If the fundamental vibration mode constraints are violated, the thickness of each

section are modified in another local-level optimization. The thickness lower bounds for the modal analysis are taken from the output of the strength-based structural analysis. The local level optimization minimizes structure mass while adjusting all section thicknesses to meet the desired rigidity criteria. The cost function for the local level optimization has scalar value, but since the problem is multi-objective the cost function weights are adjusted until adequate vibrational mode convergence is met ($< 1\%$). The cost function for the modal analysis, after trial and error, is the dry mass plus 10 times the error for each respective vibrational mode from the target, if the respective constraint is violated (Eqn. 3.93). The algorithm of choice is the L-BFGS-B algorithm in the Scipy Optimize module minimize function (Virtanen et al., 2020). The L-BFGS-B algorithm was chosen as the problem was non-linear and the solutions may not exist at the extremes and have local optima. The limited memory, bounded BFGS algorithm is in the class of quasi-Newton's method and was found to quickly converge on thickness values for a modal analysis compared to other non-linear methods available in the Scipy Optimize module. The good performance is attributed to the smoothness of the objective function and the algorithm's ability to handle many variables. The modal analysis and sizing is relatively fast as no flight simulations are needed and all required sub-processes are analytic.

$$Cost_{modal} = m_{dry} + 10[f_{axial,calc.} - f_{axial,desired}] + 10[f_{bending,calc.} - f_{bending,desired}] \qquad (3.93)$$

Typically, thin sections, such as the engine skirt or upper stage portions that have low strength requirements are the thinnest and offer the greatest rigidity increase for additional inert mass, so are found to be the altered members. Once the modal constraints are met, while inert mass is minimized, the thickness generated are assumed a lower bound for a strength-based structural analysis. The strength-based analysis is re-done ensuring margins are at or above the desired safety factors. The two structural sub-routines are, in general,

89

continuously called until all criteria is met. Typically after a modal constraint update, the required strength does not change. There is however, certain situations that lead to infeasible designs, where neither constraint can be met either until the maximum number of iterations is met or the initial thrust to weight ratio becomes less than one. The author speculates that this is occurring for certain configurations of high-aspect ratio vehicles.

3.6   Global Optimization

Particle swarm optimization (PSO) and genetic algorithms (GA) were identified as useful after the literature search was conducted for launch vehicle MDO presented earlier. Particle swarm optimization was selected for this study since other authors reported the success of PSO and potential superiority over GA, for launch vehicle design space (Miranda, 2015; Castellini and Lavagna, 2012; Castellini, 2012; Casalino et al., 2019a).

The Python module Pyswarms (Miranda, 2018) is used. Pyswarms has a user-friendly, tested, and maintained implementation of the algorithm. Evolutionary-based algorithms are of top consideration compared to the derivative-based methods used in inner-loops since the design space may not be sufficiently smooth.

In PSO, a swarm of $\mathcal{N}$ particles is placed randomly over n-dimensional space, where n is the number of design dimensions. The particles start with random initial velocity. The velocity of a single particle is then changed depending on what the individual perceives as the best locally, and what the consensus of the best is for the nearest k particles perceives. If a given particle is aware of the entire population's consensus of the optimal then the PSO is "fully informed". The individual and social "forces" are then weighted by constants c_1 and c_2 respectively. The particle may have inertia from mass parameter w to resist instantaneous direction changes.

The PSO parameters presented in Table 3.7, are initially used after a preliminary single-stage dry mass minimization study. The used PSO parameters are nearly identical to the

90
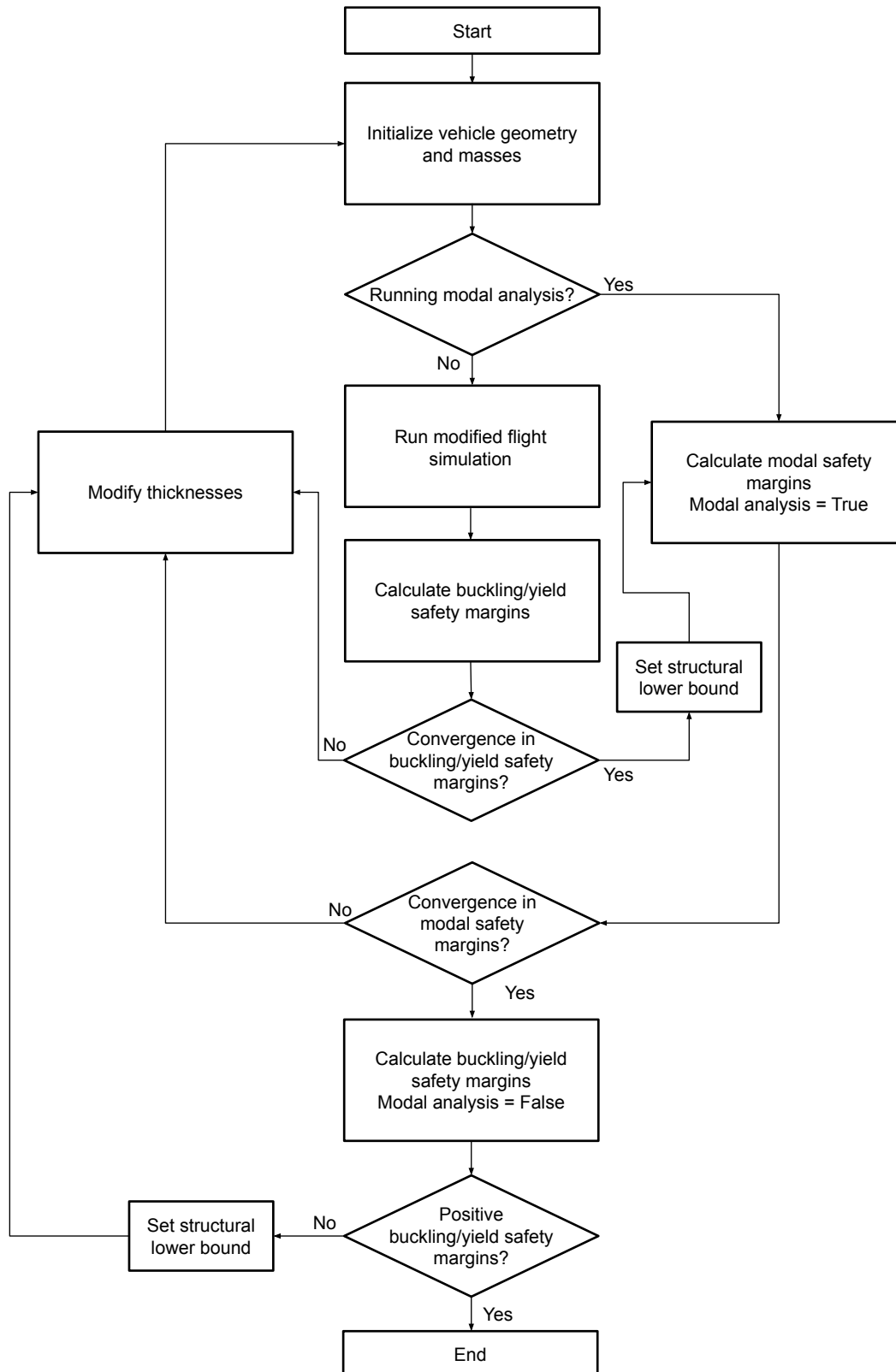
Figure 3.34: Structural optimization program schematic

default values provided by the Pyswarms python module (default is 0.5 for c_1, c_2, and w). The parameters used by Miranda were not available. High cognitive and social weights, used by other researchers (Casalino et al., 2019a), produced large accelerations and sporadic behavior that initially did not repeatedly find the best of the solution space. The number of particles per dimension required to ensure convergence is found to depend on how close the placed bounds are to the optimal values. In the absence of large parallel computing resources, the strategy is to start with a large amount of particles (10 per dimension), observe what feasible design configurations emerge, then reduce the bounds accordingly (5 per dimension).

The position (Eqn. 3.94) and velocity (Eqn. 3.95) are updated after each particle completes their respective evaluation. Population-based optimization schemes naturally make efficient use of parallel computing. Parallel computing is employed in this thesis to greatly improve global optimization speed.

$$x_i(t+1) = x_i(t) + v_i(t+1) \tag{3.94}$$

$$v_{ij}(t+1) = w * v_{ij}(t) + c_1 r_{1j}(t)[y_{ij}(t) - x_{ij}(t)] + c_2 r_{2j}(t)[\hat{y}_j(t) - x_{ij}(t)] \tag{3.95}$$

PSO parameter	Value
c_1	0.5
c_2	0.6
w	0.6
k	$\mathcal{N}$-1 (fully informed)
$\mathcal{N}$	5 to 10 (per dimension)

Table 3.7: Particle swarm optimization parameters used

The global optimization is placed at the output of the entire conceptual design process (Fig. 3.35). The structures and propulsion designs are optimized/converged at the local level for each conceptual design iteration, resulting in feasibility for those disciplines.

The desired cost was centered around rocket dry mass. The cost function that is found to
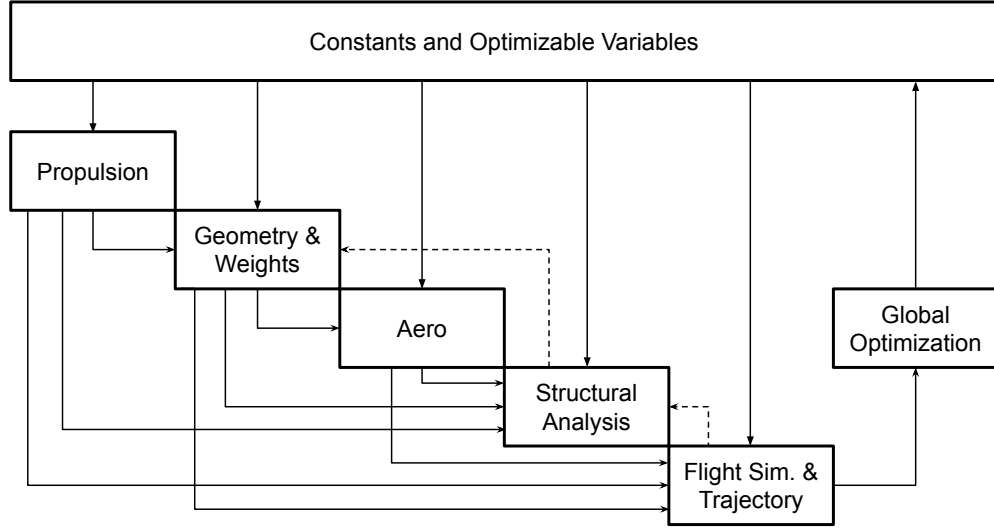
Figure 3.35: Global program schematic

produce feasible and optimal designs of minimum dry mass is presented in Eqns. 3.96. The cost function maintains some feasibility of the design, so the process is part Inter-Disciplinary Feasible (IDF) (Cramer et al., 1992). The positive propellant residual, minimum staging altitude, and initial altitude constraints are enforced by the global optimizer by means of penalizing weighs introduced if the conditions are violated.

$$
Cost = \begin{cases} C_0 \cdot m_{dry} + C_1 \Delta V_{res} + C_2 \Delta_{H,stage} + C_3 \Delta_{H,SECO,1}, & \text{If mission succeeds} \\ 1 \times 10^7, & \text{If mission fails} \end{cases} \tag{3.96}
$$

The weights (C_0, C_1, C_2, C_3) of the terms in the cost function are scaled with dry mass and are determined using Eqns. 3.97 to 3.102. The weights were determined manually after observing the vehicle masses resulting from the optimization runs and applying sufficient weighting to the constraint errors such that solutions never violated them. The variable ΔV_{res} is in units of m/s. The relatively large 15 km allowable error on the SECO-1 altitude $(H_{SECO,1})$ is implemented to speed up the local-level trajectory convergence. Having a smaller tolerance resulted in very long computational run times. The accuracy of the final

orbit is unaffected by the inaccurate initial altitude. The initial burn to reach the orbit apogee and the circularization burn can accurately provide the required orbit since they are accomplished by truncating burn times. The staging altitude constraint (Eqn. 3.100) is first implemented such that the upper stage flight is outside of the allowed maximum dynamic pressure ranges, and the load formulation and trajectory formulation assumptions are kept valid. A 30 km staging altitude ($H_{staging}$) constraint was implemented as it was observed to typically be after the maximum dynamic pressure point of the vehicle's flight. Staging altitudes are later observed, for optimal configurations, to be beyond 50 km above ground level. The encountered staging altitudes are driven by dry mass minimization rather than enforced constraints, so the constraint is ultimately unused. At 50 km altitude, the dynamic pressure is far below the maximum, for the encountered speeds at staging of 2-3 km/s.

$$C_0 = 100 \tag{3.97}$$

$$C_1 = \begin{cases} 100 \cdot m_{dry}, & \Delta V_{res} < 0 \\ -0.1, & \Delta V_{res} \geq 0 \end{cases} \tag{3.98}$$

$$C_2 = \begin{cases} \frac{m_{dry}}{100}, & \Delta_{H,stage} < 0 \\ 0, & \Delta_{H,stage} \geq 0 \end{cases} \tag{3.99}$$

$$\Delta_{H,staging} = H_{staging} - H_{staging,minimum} \text{ [m]} \tag{3.100}$$

$$C_3 = \begin{cases} \frac{m_{dry}}{100}\left(\frac{|\Delta_{H,SECO,1}|}{15000} - 1\right), & |\Delta_{H,SECO,1}| \geq 15000 \\ 0, & |\Delta_{H,SECO,1}| < 15000 \end{cases} \tag{3.101}$$

$$\Delta_{H,SECO,1} = H_{SECO,1} - H_{SECO,1,target} \text{ [m]} \tag{3.102}$$

Chapter 4

Results

4.1 Single-stage Parametric Studies

Parametric studies of single-stage, sub-orbital rocket vehicle configurations are described in this chapter. The goals of the studies are to identify design trends, observe if the optima exist at the extremes, and identify physical bounds for use within the computationally-intensive multi-stage global optimization studies. Back-fill-pressure-fed and electric pump-fed systems are investigated for LOx/paraffin and N_2O/paraffin HREs to be used in these assessments. Additionally, a self-pressurizing feed system is investigated for N_2O/paraffin HRE configurations. Helium is used for the pressurant gas when required as it resits dissolving in the oxidizers, compared to other inert gases (Zucker et al., 1989). Helium also has a low specific heat ratio and molecular weight relative to other common pressurant gases resulting in less inert mass and higher performance. The parametric studies are conducted holding all other design variables constant, except the burn time. All parametric studies are conducted with a range of burn times and the final results are presented with the optimal burn time for each parameter value. Simulating over a range of burn times is done to remove its influence on the results, as it was found to interact with different design variables, especially if the vehicle scale changed drastically through parameter sweeps.

The default outer diameter, in this parametric study, is set to the minimum possible given vehicle geometry constraints (nozzles and combustion chambers). The minimum diameter is used after initial results showed it is likely the most optimal and will lead to better comparison across different scales (dry mass values). For all other design variables, when they are not being varied, are taken as the value in Table 4.1. The OF_{av} and P_{up} values in Table 4.1 are used as they are conjectured to be optimal or near optimal. For a reasonable physical upper bound, the pressurant initial pressure is 18 MPa, as this is a common gas storage pressure found in gas cylinders and is a typical service pressure for standard fittings and piping (Hermsen and Zandbergen, 2017). The pressurant initial temperature is chosen to correspond to standard conditions (15° C). The nozzle exit pressure of 50 kPa is used as it is desired to be minimized, while still meeting the Summerfield criteria (Stark, 2005). The 10 kPa margin is used to ensure variations in mass flow, caused by OF shift, did not reduce the chamber pressure and subsequently nozzle exit pressure below the 40 % of standard sea level ambient pressure. Perhaps for a smaller total impulse scale vehicle, the optimal expansion may be a higher exit pressure, but this is not the case for the very high-flying rockets being considered here. The initial oxidizer temperature, when the feed system is either back-fill or pump-fed, is presumed to be the oxidizer normal boiling point. The normal boiling point temperature is selected for practical purposes as the temperature can be easily controlled, if heating occurs, by allowing the oxidizer to boil off as required to remove energy supplied by the ambient environment. The self-pressurizing N_2O initial temperature value is arbitrarily chosen. All other constants are taken from Tables B.1, B.2, and B.3 listed in the appendix.

The parametric studies being done here use the vehicle's ΔV from final altitude and velocity to quantify performance. The ΔV in these parametric studies (Delivered ΔV) is calculated from an energy balance using the vehicle final altitude (ΔH), which occurs at zero velocity due to the vertical, non-perturbed flight. The delivered ΔV is calculate from the following: $\Delta V = \sqrt{2\mu_E(\frac{1}{r_E} - \frac{1}{r_E+\Delta H})}$, and r_E is the Earth radius. The rocket speed, immediately post-burn, is not used as the change in velocity (ΔV), in order to account

Variable name (symbol)	Value
Total impulse (I_t)	1000 kN·s
Burn time (t_b)	Optimal (floating)
Outer diameter (OD)	Minimal (floating)
Number of first stage engines	1
Payload mass	10 kg
Launch angle	$\frac{\pi}{2}$ rad
Nominal OF ratio for N$_2$O/paraffin (OF_{av})	6.0
Nominal OF ratio for LOx/paraffin (OF_{av})	2.2
Back-fill regulated pressure or electric pump discharge pressure (P_{up})	1.8×10^6 Pa
Pressurant initial pressure ($P_{1,pg}$)	1.8×10^7 Pa
Nozzle exit pressure (P_e)	50×10^3 Pa
Pressurant initial temperature ($T_{1,pg}$)	288 K
N$_2$O initial temperature for back-fill and electric pump-fed ($T_{ox,1}$)	185 K
N$_2$O initial temperature for self-pressurizing ($T_{ox,1}$)	273 K
LOx initial temperature for back-fill and electric pump-fed ($T_{ox,1}$)	91 K

Table 4.1: Parameter nominal values

for possible drag losses in the coast phase. The expression used most accurately captures the delivered ΔV, however one must note that its value is less than the theoretical value predicted by Eqn.3.1 since it accounts for all present losses.

4.1.1 Upstream Pressure

The upstream pressure (P_{up}) is the oxidizer fluid pressure immediately upstream of the injector, and is determined differently for each feed system configuration as specified. For pump-fed systems, P_{up} is the pump discharge pressure, for pressure-fed systems it is equal to the oxidizer tank pressure. The upstream pressure was varied from 0.2 MPa to 1.5 MPa and the resulting chamber pressure's effect on performance (delivered ΔV) is presented in Fig. 4.1. Note the presented chamber pressure can be converted into upstream pressure by multiplication of a factor, in the present study, this factor is 1.55.

An optimal chamber pressure value is found for each feed system considered. The trade-off of propellant mass percentage and specific impulse (Fig. 4.2) results in an optimal chamber pressure that maximizes performance. Specific impulse increases as chamber pressure is
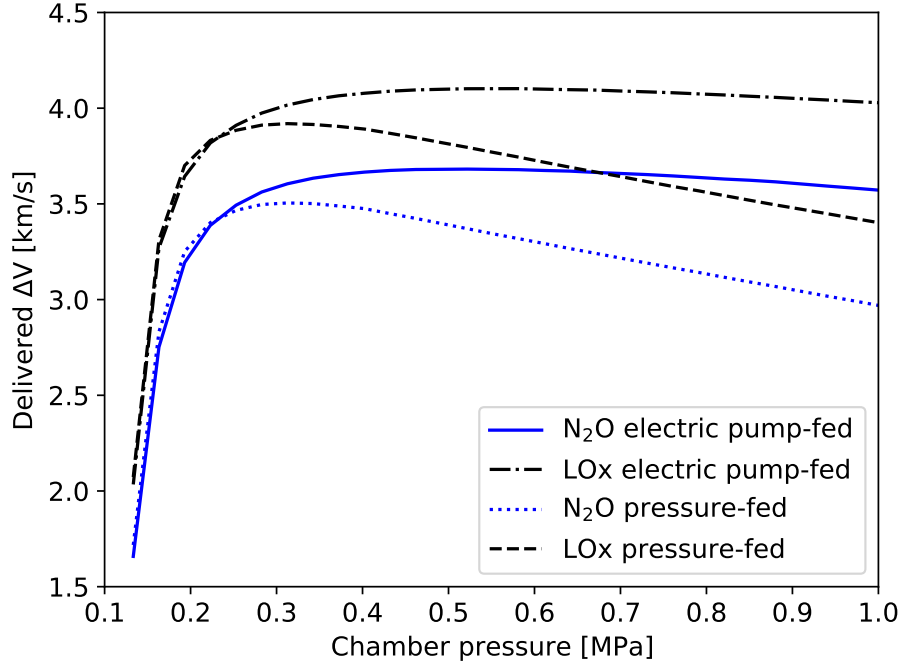
Figure 4.1: Vehicle performance (delivered ΔV) vs chamber pressure

increased, seen in Fig. 4.2. The lower performance for higher chamber pressures is due to the larger inert mass via pressure vessel walls and feed systems. The vehicle propellant mass percentage ($\frac{m_{prop}}{m_{total}} \cdot 100\%$) is shown in the subplot of Fig. 4.2. The mass margins are the best for smallest chamber pressures as expected. At the extremely small chamber pressures, some structural failure modes become independent of pressure so the propellant mass percentage peaks, and becomes lower. The non-smooth nature of the some of the curves, as seen in Fig. 4.2, is from the granularity available in the data as a result of the discretization of the burn times, since all plots are presented at optimal burn times.

Pump-fed systems exhibit a flat plateau across chamber pressures once past the initial drop-off, as only the combustion chamber and pump/battery mass is increasing while the oxidizer tank only withstands the NPSP and all other necessary loads. For the pressure-fed-back-fill case, the oxidizer tank mass increases quickly relative to increasing specific impulse and relatively small value optimal chamber pressure is the result. The optimal chamber
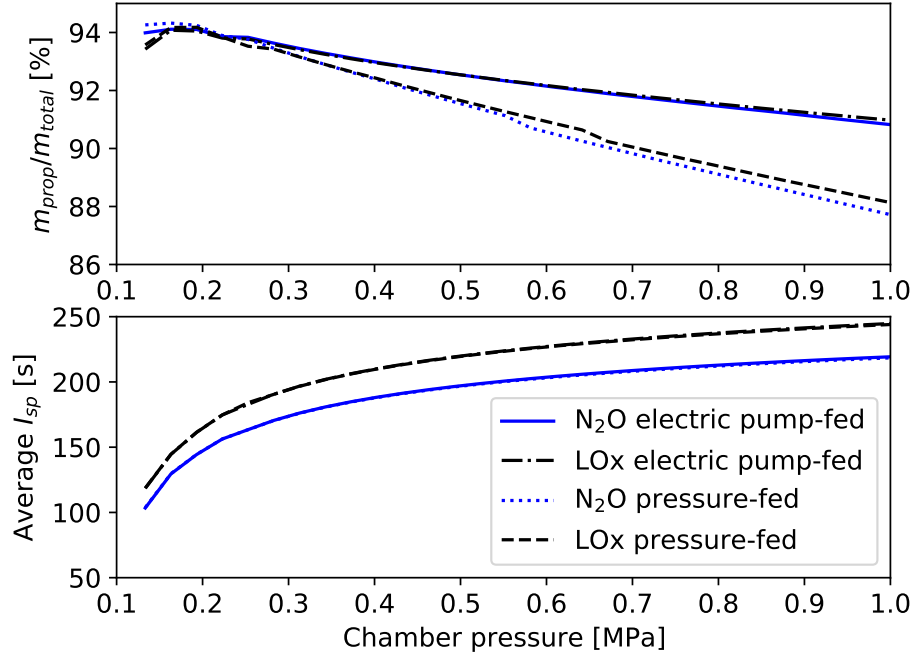
Figure 4.2: Vehicle delivered specific impulse and propellant mass percentage vs chamber pressure

pressure is 521 kPa and 582 kPa for N_2O pump-fed and LOx pump-fed respectively. The optimal chamber pressure for both back-fill cases is 312 kPa. The identical optimal pressure-fed chamber pressure values are attributed to the step size used in the parametric study.

The specific impulse (I_{sp}) is observed to vary the most at smaller chamber pressures (Fig. 4.2), then flatten out for larger pressure values. The very small I_{sp} discrepancies between the configurations, using the same propellants, arise from slight variations in back pressure resulting from non-identical altitude-time histories of the flights.

4.1.2   Body Outer Diameter

The body diameter input was ranged between 0.2 m and 1.0 m. For the investigated configurations, the body outer diameter is desired to be minimized, given constraints, in order to maximize performance (Fig. 4.3). The structure, at a larger diameter, for the same mission was found to be less mass-efficient. The additional structure mass and additional
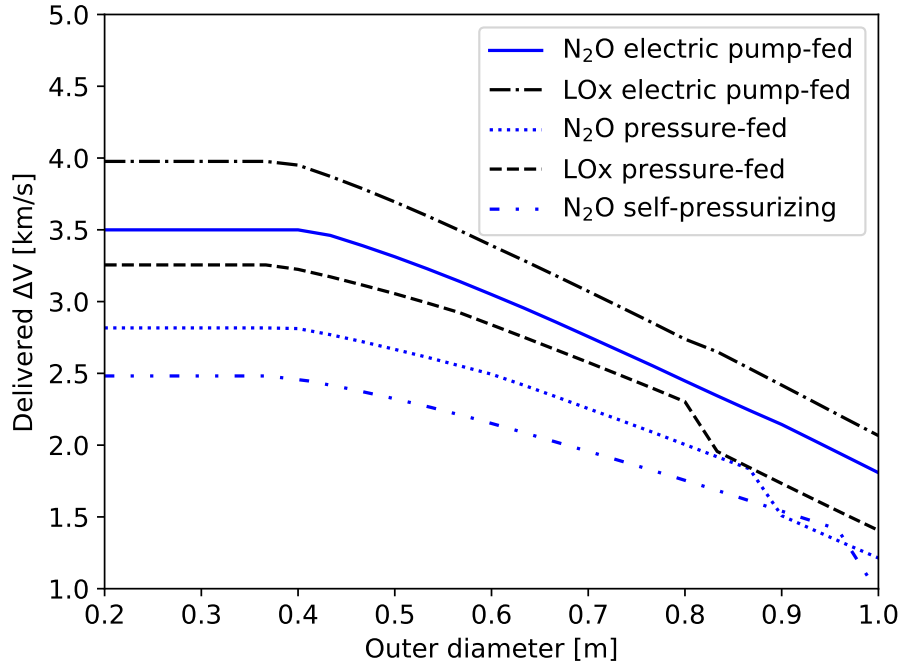
Figure 4.3: Vehicle performance (delivered ΔV) vs outer diameter

drag reduces the performance of larger diameter rockets. The zero-slope regions in Fig. 4.3 are from the code setting the diameter to the lowest allowable, which is slightly different between configurations.

The specific impulse is marginally decreased due to the larger portion of the flight in a higher back pressure environment, shown in Fig. 4.4. The added larger geometry also creates higher aerodynamic loading that leads to more inert mass. The decrease in propellant mass-percentage, for increasing diameter, is shown in Fig. 4.5.

There may be very high aspect ratio configurations, possibly for different propellants, where the optimal diameter is not minimal, given modal constraints. A mid-range optimal was not found here, even for single-engine configurations (highest available aspect ratio).
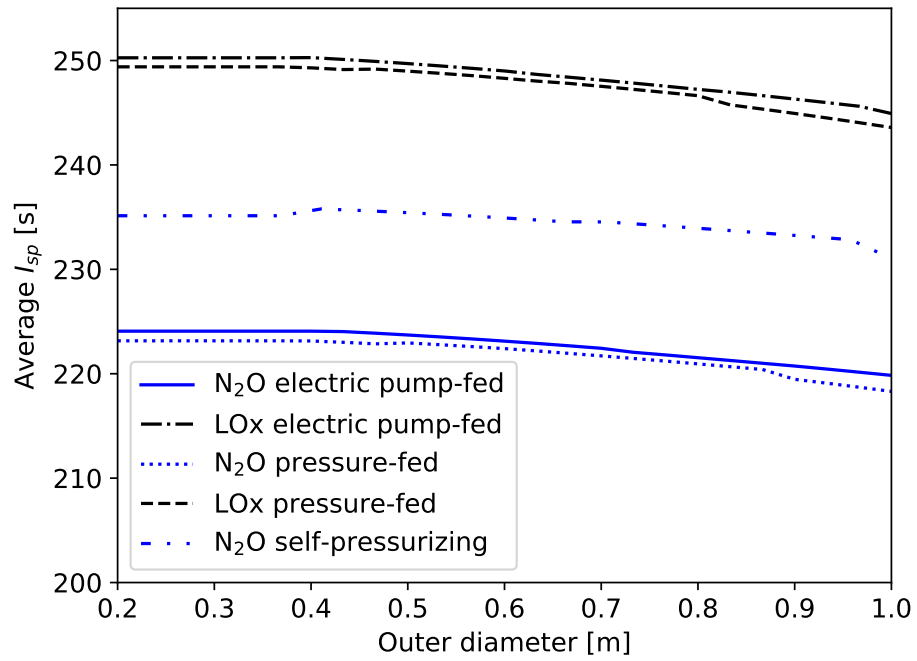
Figure 4.4: Vehicle delivered specific impulse vs outer diameter
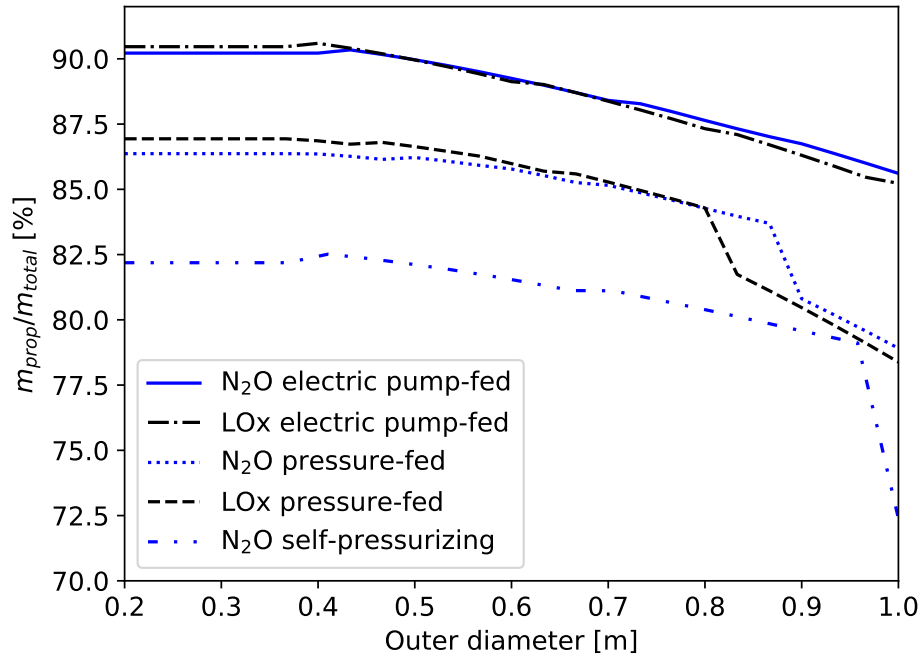
Figure 4.5: Propellant mass percentage vs outer diameter
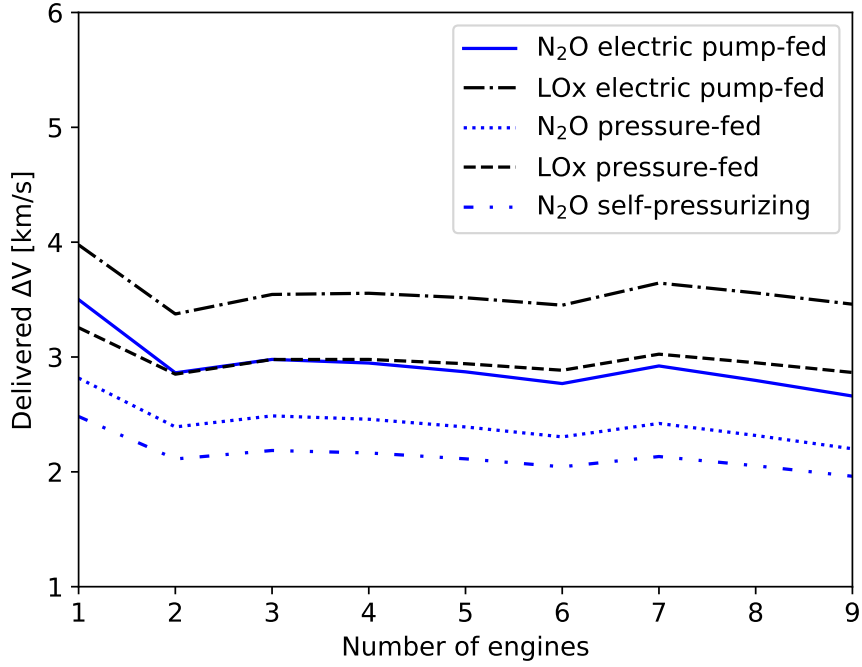
Figure 4.6: Vehicle performance (delivered ΔV) vs number of engines

4.1.3 Number of Engines

For all propellant/feed system configurations, the optimal number of engines is one (Fig. 4.6). The single-engine configuration's packing efficiency in the cylindrical rocket body reduces the drag, and structure mass (Fig. 4.7), by reducing the required body diameter.

The seven-engine configuration is a local optimal and is useful when multiple smaller engines are desired in order to reduce mass and thrust per-engine for manufacturing and testing purposes. Having more smaller engines is also more mass-efficient for the same fuel mass from the combustion chamber scaling point of view. The propellant-tank-to-fluid mass ratio for different engine numbers is not constant across scales because the injector (fore) end of the combustion chamber is modeled as a flat plate. The flat end-caps are more mass-efficient at smaller diameters (Eqn. 3.68). Because of the non-linear combustion chamber mass scaling, the three engine configuration is superior to seven in N_2O-based systems (Fig. 4.6), but that is not the case for LOx-based configurations due to the operation OF_{av} dif-
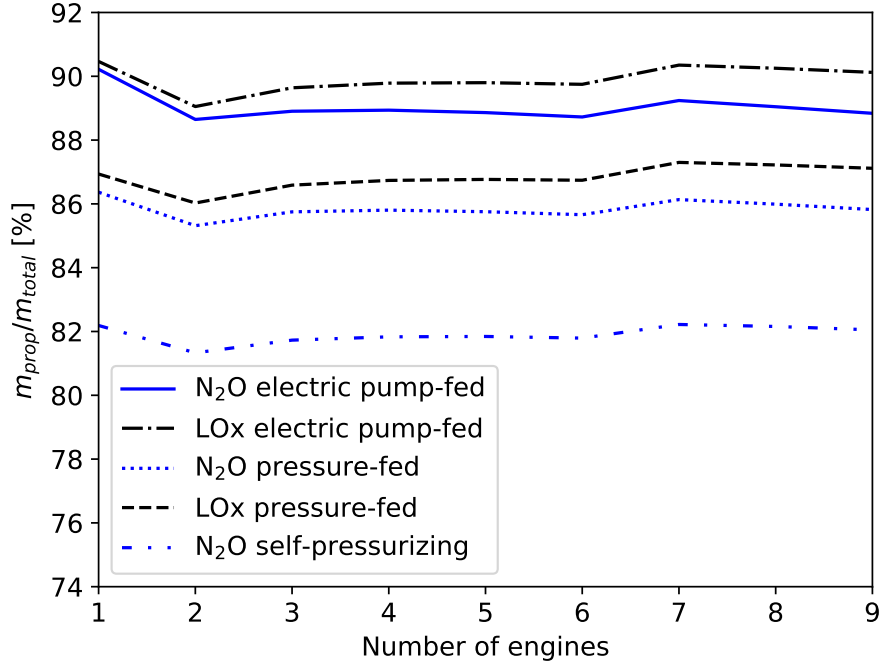
Figure 4.7: Propellant mass percentage vs number of engines

ference. The higher propellant mass fraction for the seven-engine configuration is overcome by the reduced drag losses from the smaller diameter of the three-engine configuration, for N_2O-based cases.

The specific impulse difference for the same engine number in Fig. 4.8 is attributed to the differing portions in higher back pressure due to the performance differences from the varying propellant mass percentages. The lower propellant mass fraction and added drag contribute to the small I_{sp} changes between different engine numbers for the same propulsion system configuration.

4.1.4 Total Impulse

The nominal-conditions total impulse (for initial back pressure) was varied between 100 kN·s and 1000 kN·s. It's worth noting that the prescribed total impulse differs from the actual delivered total impulse due to changes in P_{amb} as well as the changes in P_c and OF from
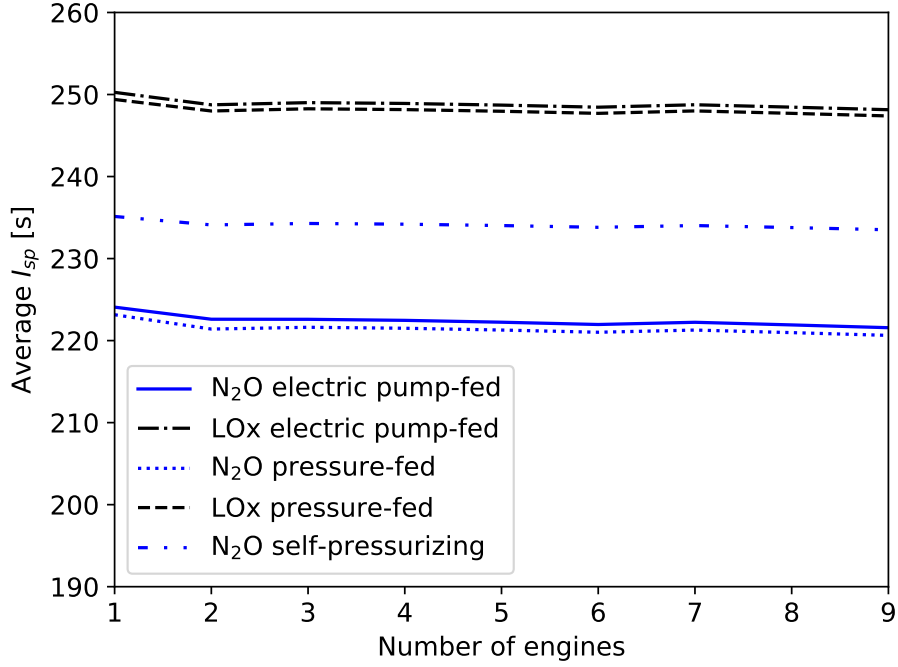
Figure 4.8: Vehicle delivered specific impulse vs number of engines

the OF shift. The performance was determined across the vehicles scales, while adjusted for optimal burn time. The gross takeoff mass is found to be linearly proportional to total impulse for all configurations considered (Fig. 4.9). Each configuration's slope is different as a result of the different mass-efficiencies.

The propellant mass percentage is observed to continually increase as vehicle total impulse is increased (Fig. 4.11). The increasing propellant mass percentage is due to the vehicle having smaller fractions of auxiliary and constant-mass components. The auxiliary components (everything that isn't propellants or pressure vessels) become a smaller portion of the vehicle mass as it scales up. The propellant mass percentage does appear to plateau for all configurations, as the vehicle propellant mass percentage is at least capped by Eqn. 3.74. The improved propellant mass percentage, and improved I_{sp} by favorable back pressure (Fig. 4.12), lead to improved overall performance (Fig. 4.10).
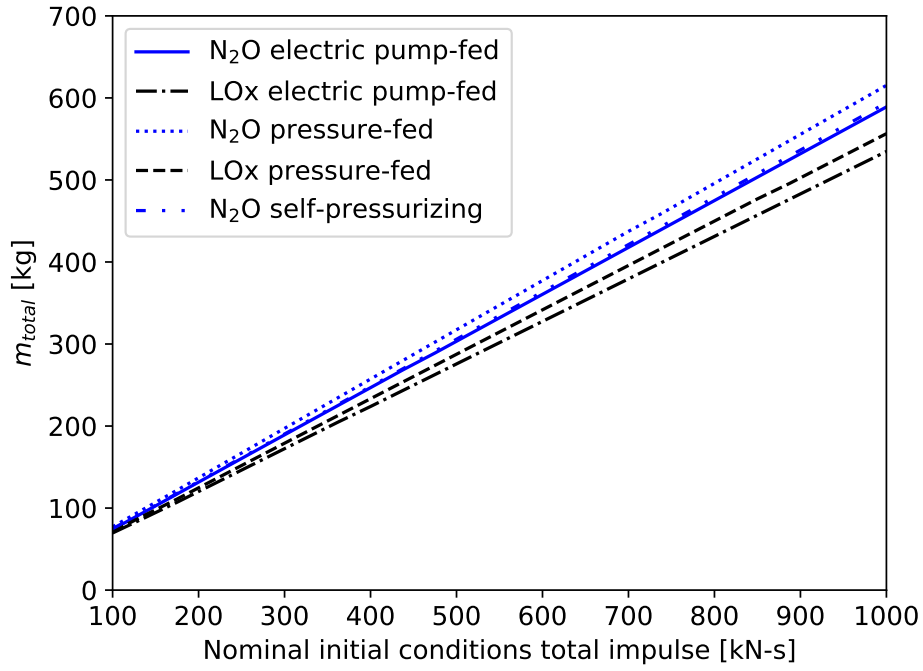
Figure 4.9: Vehicle total liftoff mass vs total impulse
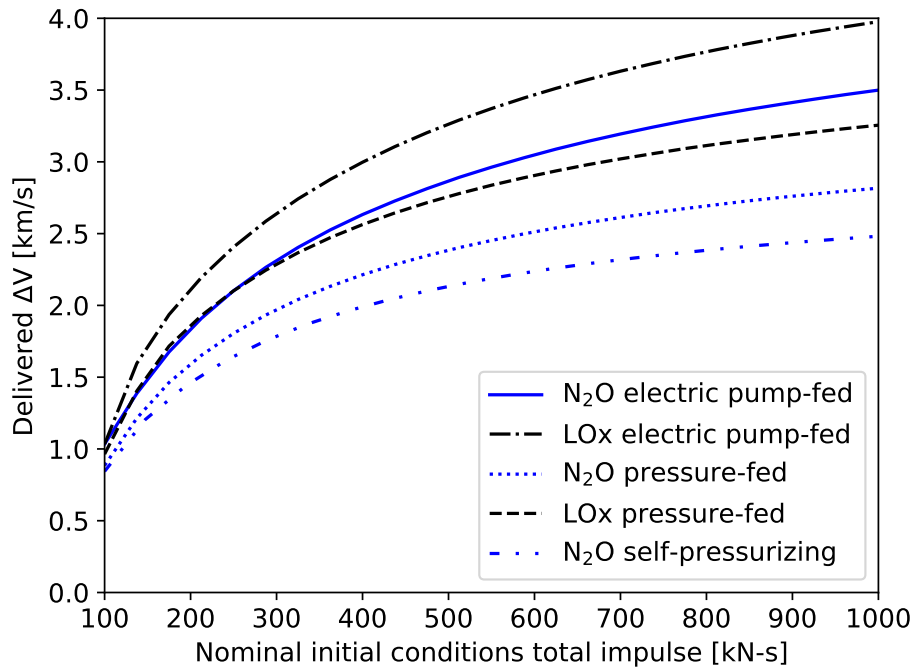
Figure 4.10: Vehicle performance (delivered ΔV) vs total impulse
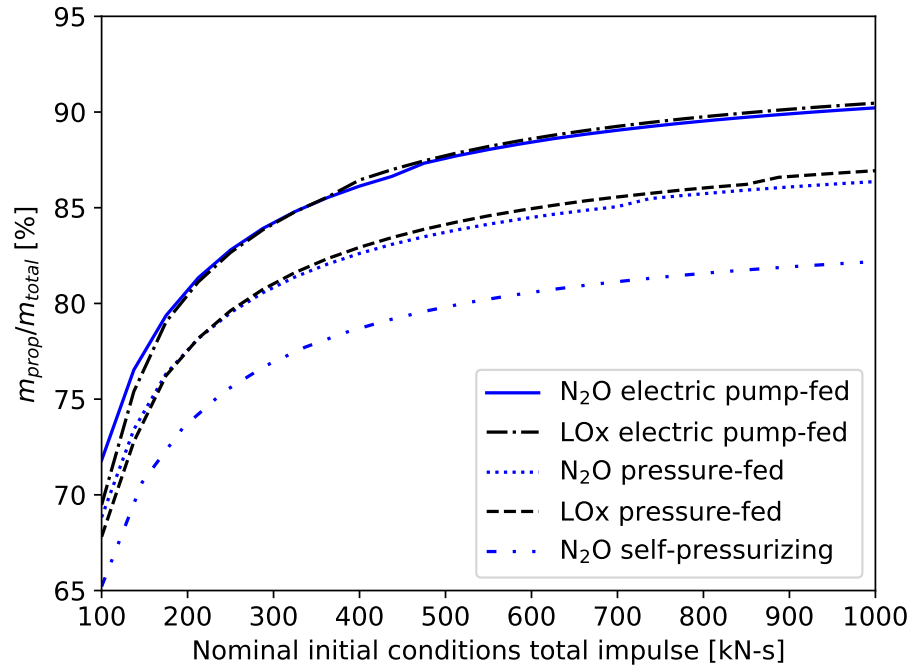
Figure 4.11: Propellant mass percentage vs total impulse
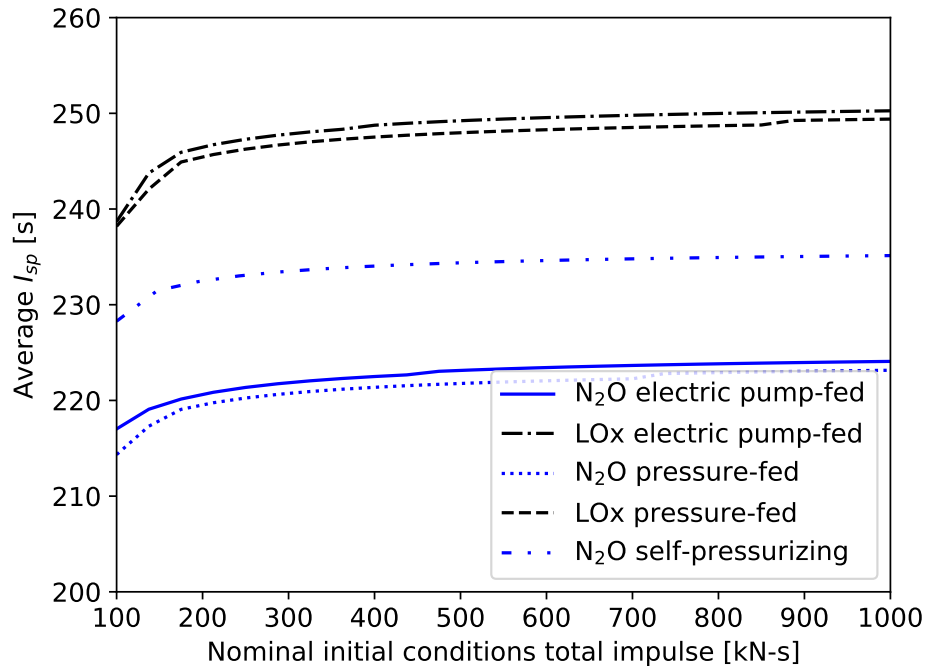
Figure 4.12: Vehicle delivered specific impulse vs total impulse
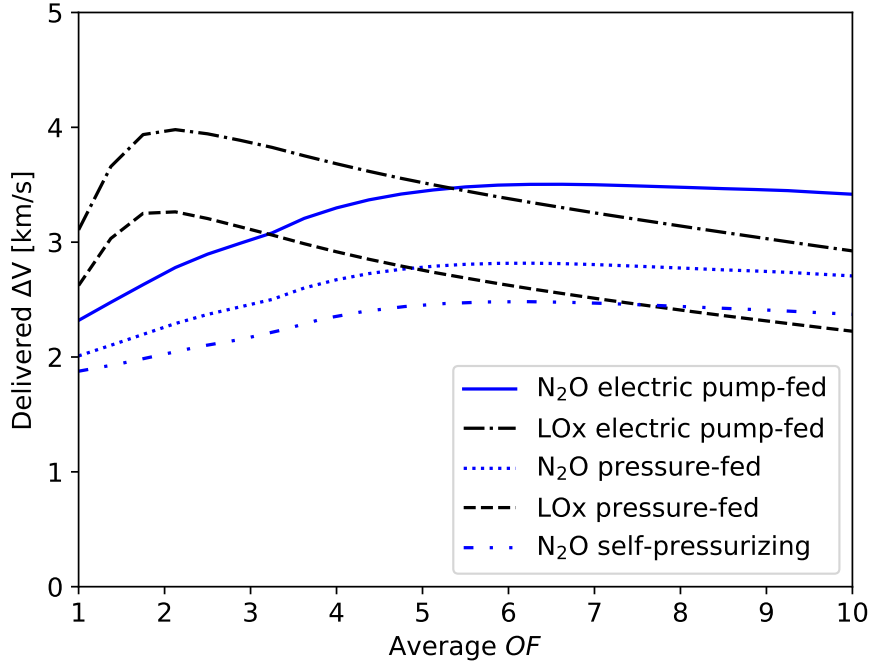
Figure 4.13: Vehicle performance (delivered ΔV) vs OF_{av}

4.1.5 Average Oxidizer-to-fuel Ratio

The vehicle performance was evaluated over a range of burn-time-averaged oxidizer-to-fuel ratios, on a mass basis (Fig. 4.13). The optimal OF_{av} that maximized performance are near the same values that maximizes average I_{sp} (Fig. 4.15). The optimal OF_{av} values are organized in Table 4.2. The The propellant-mass-ratio generally gets higher for lower OF_{av} values (Fig. 4.14) but the drop in I_{sp} is too detrimental and the net effect is poorer performance.

Configuration	Optimal OF_{av}
LOx electric pump-fed	2.125
LOx pressure-fed, back-fill	2.125
N_2O electric pump-fed	6.625
N_2O pressure-fed, back-fill	6.25
N_2O pressure-fed, self-pressurizing	6.21

Table 4.2: Optimal OF_{av} values for investigated single-stage configurations
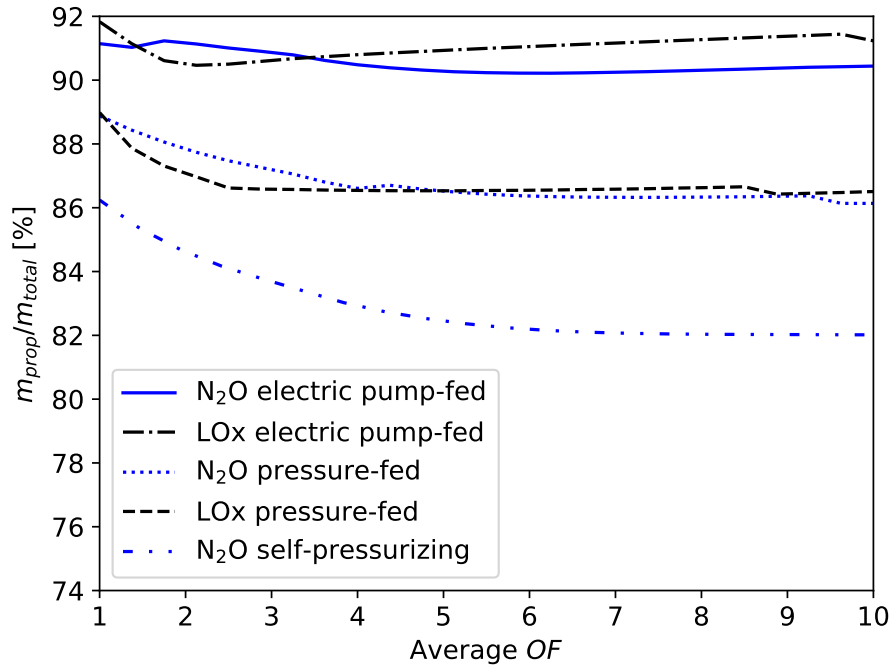
Figure 4.14: Propellant mass percentage vs OF_{av}
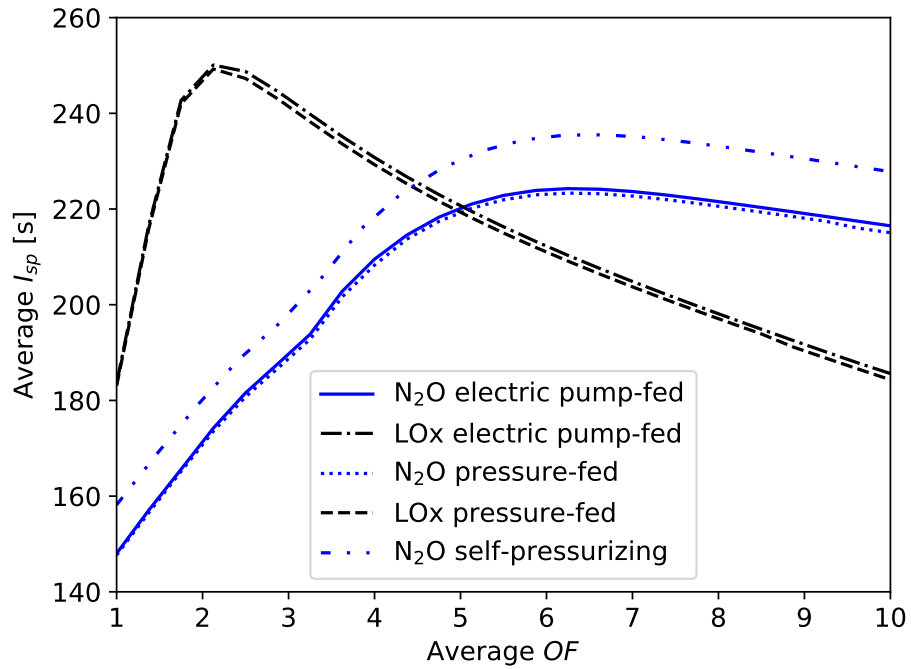
Figure 4.15: Vehicle delivered specific impulse vs OF_{av}
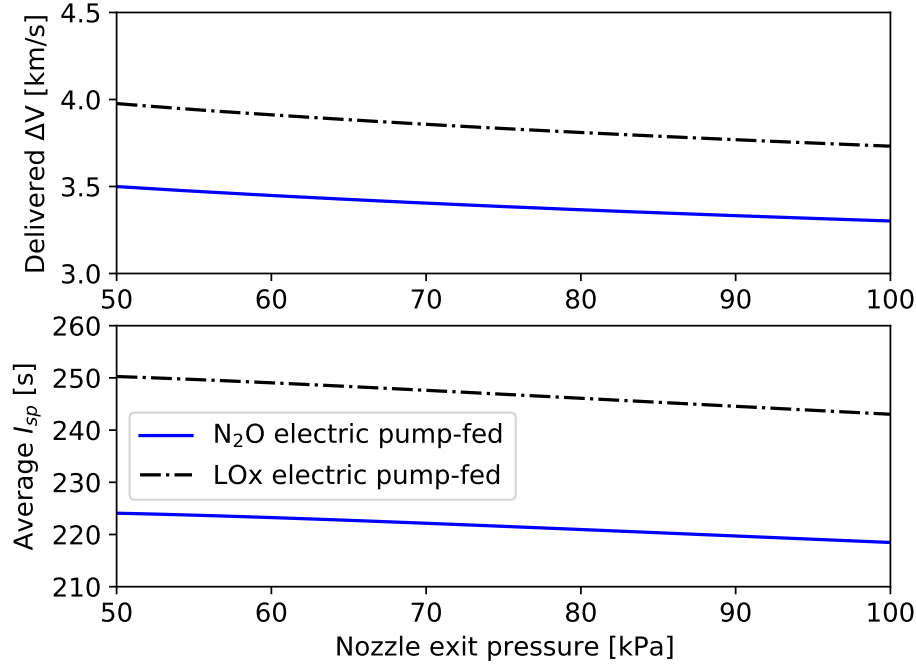
Figure 4.16: Vehicle performance (delivered ΔV) and I_{sp} vs nozzle exit pressure

4.1.6 Nozzle Exit Pressure

The nozzle exit pressure was only investigated for electric pump-fed configurations as it was expected to have the same behavior found in the pressure-fed configurations. The decrease in exit pressures lead to higher exhaust velocities that increased specific impulse directly (Fig. 4.16).

4.1.7 Pressurant Tank Initial Pressure

The pressurant tank initial pressure ($P_{1,pg}$) was varied between 6.8 MPa and 35 MPa. The pressure should theoretically have little influence on the required mass of pressurant gas, at high initial pressures relative to regulated pressure ($\frac{P_{ox}}{P_{1,pg}} << 1$), as seen in Eqn. 3.26. The pressurant gas density, assuming ideal gas, is proportional to pressure. Since the tank mass scaling is proportional to fluid density and inversely proportional to fluid pressure (Eqn. 3.74), the pressurant gas vessel mass is approximately constant. The vehicle
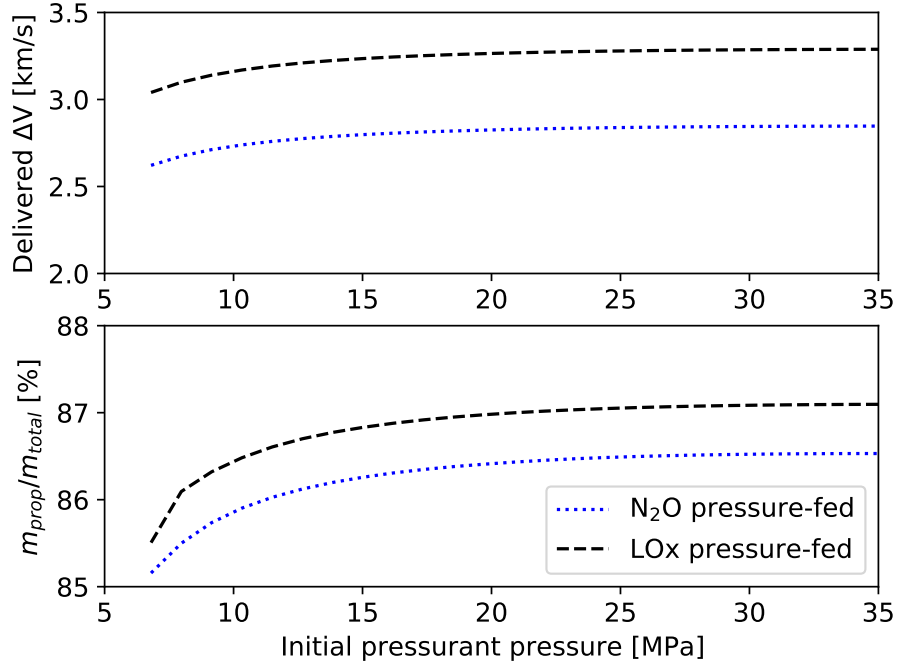
Figure 4.17: Vehicle performance (delivered ΔV) and propellant mass ratio vs pressurant initial pressure

total inert mass is found to reduce due to the smaller required volume of the rocket upper-tank section surrounding structure. As the pressurant pressure becomes large, the pressurant tank becomes a negligible volume in the rocket structure and the propellant mass percentage values flatten out (Fig. 4.17).

4.1.8 Initial Oxidizer Temperature

The delivered ΔV was determined over a range of initial oxidizer temperatures for LOx and N$_2$O self-pressurizing configurations (Fig. 4.18). The initial oxidizer temperature for the LOx cases ranged from the normal boiling point (90 K) to the temperature that Spacex chills their LOx to ($66K$) (Musk, 2015). The range of N$_2$O initial temperatures was chosen around the value of optimal equilibrium fluid conditions. The N$_2$O configurations were not investigated below the N$_2$O normal boiling point of 184 K, since it quickly transitions to a solid at 182 K. Back-fill or pump-fed N$_2$O configurations were not explored since there was
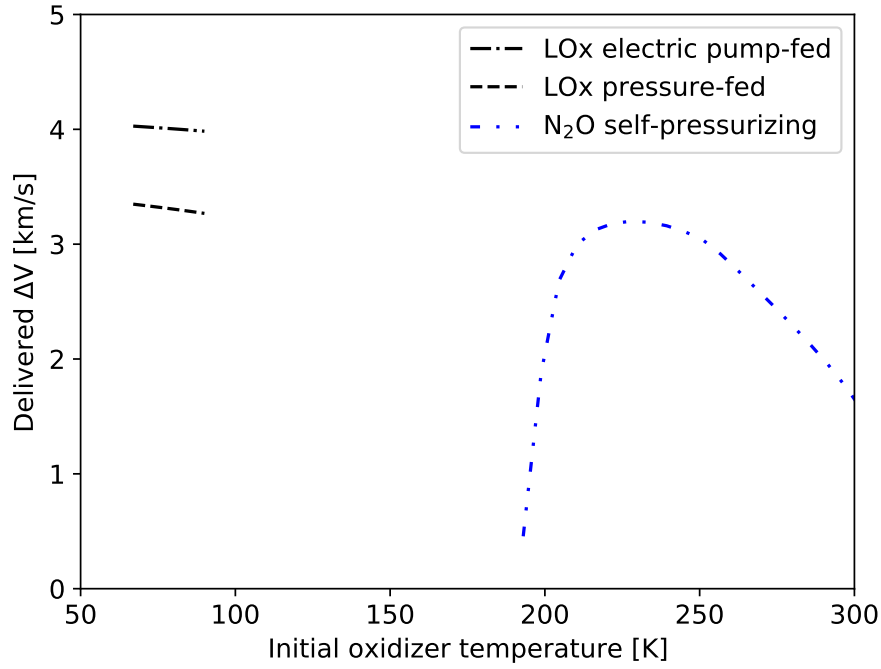
Figure 4.18: Propellant mass percentage vs oxidizer initial temperature

very little margin to improve density below the normal boiling point performance and would come with the risk of solid nitrous in the feed system. The large sensitivity to temperature for the N_2O case results from its influence on vapour pressure. The LOx electric pump-fed case delivered ΔV and the LOx pressure-fed cases varied marginally across the temperature range investigated. The improvement for the LOx cases is due to the density increase and reduced tank size as well as reduced vapour pressure. The reduced tank size has a larger influence on the pressure-fed case than the pump-fed case due to the oxidizer tank pressure difference.

The optimal N_2O self-pressurizing case results in 3.2 km/s delivered ΔV. The optimal N_2O self-pressurizing case is compared to the values from Fig. 4.1 for a relative comparison as the nominal upstream pressures in the parametric studies were off-optimal. The maximum performance found from all parametric studies is organized in Table 4.3.

Configuration	Maximum delivered ΔV [km/s]
LOx electric pump-fed	4.1
LOx pressure-fed, back-fill	3.9
N_2O electric pump-fed	3.7
N_2O pressure-fed, back-fill	3.5
N_2O pressure-fed, self-pressurizing	3.2

Table 4.3: Best performance found during parametric studies

4.2 Multi-stage Optimization Studies

The global optimization studies were conducted for 10 kg to 500 km Sun-Synchronous Orbit (SSO) and 150 kg to 500 km SSO. The specified low Earth orbit is in typical practical ranges and is a common standard orbit cited by launch providers (see Table 1.1). The orbit measures the launch vehicle performance more directly since the inclination is very close to 90 degrees (polar), so the launch vehicle gains no help or hindrance from the additional velocity due to Earth's rotation.

The two missions (10 kg and 150 kg) were chosen to observe the relative scales and optima of different configurations of propellants and feed systems. The 10 kg payload to 500 km SSO mission was taken as the minimum practical payload class given the surveyed HRE-based launchers in development (Table 1.1). Designing for smaller payloads requires a more detailed design as miscellaneous components (fasteners, plumbing, wire, etc.) could easily remove the payload capability since their estimated values are on the order of one kg. The 10 kg nominal payload was chosen to give a margin so the payload capability is less likely to be removed by miscellaneous unaccounted masses. Uncertainty in the conceptual design framework should reduce as scale is increased as only the largest mass components are accounted for in the modeling. The conceptual design framework aims to present a realistic mass budget that the detailed designer has to meet. When component masses creep beyond their budget for a given stage, the mass has to be removed from another area, particularly on the present stage. The 150 kg payload to 500 km SSO mission was chosen such that the performance of the conceptually designed rocket could be compared to many existing

rockets/designs. The 150 kg payload delivery to 500 km polar orbit/SSO is the maximum capability offered by Reaction Dynamics (Table 1.1), Rocket Lab (RocketLab, 2020b), and Astra (Astra, 2020).

The different vehicle configurations investigated in the global optimization studies used either LOx or N_2O oxidizers with either back-fill-pressure-fed or electric pump-fed feed systems for each stage. The test matrix is presented in Table 4.4. Initially, pressure-fed configurations were not expected to have sufficient mass efficiency to support two-stage-to-orbit launch capability, after Miranda (2015) found that was the case. The early parametric studies proved a possible design solution, with relatively low-pressure combustion that proved pressure-fed configurations had, although not as good, comparable performance to pump-fed systems.

Name	Payload (kg)	Oxidizer	First-stage feed system	Second-stage feed system
LBB10	10	LOx	Back-fill-pressure-fed	Back-fill-pressure-fed
LBE10	10	LOx	Back-fill-pressure-fed	Electric pump-fed
LEB10	10	LOx	Electric pump-fed	Back-fill-pressure-fed
LEE10	10	LOx	Electric pump-fed	Electric pump-fed
NBB10	10	N_2O	Back-fill-pressure-fed	Back-fill-pressure-fed
NBE10	10	N_2O	Back-fill-pressure-fed	Electric pump-fed
NEB10	10	N_2O	Electric pump-fed	Back-fill-pressure-fed
NEE10	10	N_2O	Electric pump-fed	Electric pump-fed
LBB150	150	LOx	Back-fill-pressure-fed	Back-fill-pressure-fed
LBE150	150	LOx	Back-fill-pressure-fed	Electric pump-fed
LEB150	150	LOx	Electric pump-fed	Back-fill-pressure-fed
LEE150	150	LOx	Electric pump-fed	Electric pump-fed
NBB150	150	N_2O	Back-fill-pressure-fed	Back-fill-pressure-fed
NBE150	150	N_2O	Back-fill-pressure-fed	Electric pump-fed
NEB150	150	N_2O	Electric pump-fed	Back-fill-pressure-fed
NEE150	150	N_2O	Electric pump-fed	Electric pump-fed

Table 4.4: Global optimization test matrix and definition of test cases

The global optimization variables that were investigated are organized in Table 4.5. The design variables are those which exhibited optima that were not at extremes, but at mid-ranged values. Total impulse is the main vehicle scaling parameter so is left to be converged for both stages. It was thought that outer diameter may not be desired to be minimized for

multi-stage rockets, so was left in. In addition to these global optimization variables there are additionally three optimization variables for the upper stage trajectory design that are optimized at a local level as previously discussed. There are also eight structural design thickness values converged/minimized at a local level for each design iteration. The engine configurations were one upper stage engine with seven first-stage engines. The pressurant gas was helium stored at 300 K and 41.4 MPa. The helium storage conditions correspond to ambient temperature and extremely high pressure. The pressurant initial storage pressure is desired to be maximized, as discovered previously from the parametric studies. The chosen pressure is assumed practical a upper-bound near what SpaceX is reported to fill their helium storage vessels to (Clark, 2016). The nozzle exit pressure was minimized, given the Summerfield flow separation criteria (Stark, 2005) and a 10 kPa margin, to 50 kPa. All other constants are taken from tables B.1, B.2, and B.3 listed in the appendix.

Symbol	Description
$I_{t,1}$	Total impulse of first stage
$I_{t,2}$	Total impulse of second stage
$t_{b,1}$	Burn time first stage
$t_{b,2}$	Burn time second stage
δ_{nozzle}	Nozzle clearance of second stage (controls area ratio)
$OF_{av,1}$	Burn-time-averaged oxidizer-to-fuel-ratio for first stage
$OF_{av,2}$	Burn-time-averaged oxidizer-to-fuel-ratio for second stage
$P_{up,1}$	Upstream pressure for first stage
$P_{up,2}$	Upstream pressure for second stage
γ_{po}	Initial pitch over angle for gravity turn
OD	Body outer diameter, if below minimum, set to minimum

Table 4.5: Global optimization variables

4.2.1 Initial Global Optimization Results

The first round of results were generated for only the 150 kg payload class. The goal of the 150 kg simulation batches were to conduct sensitivity/parametric tests on the resulting optimal configurations to see how the maximum deliverable payloads and payload fractions changed for one-at-a-time (parametric) and Monte Carlo sensitivity analyses. The 150 kg
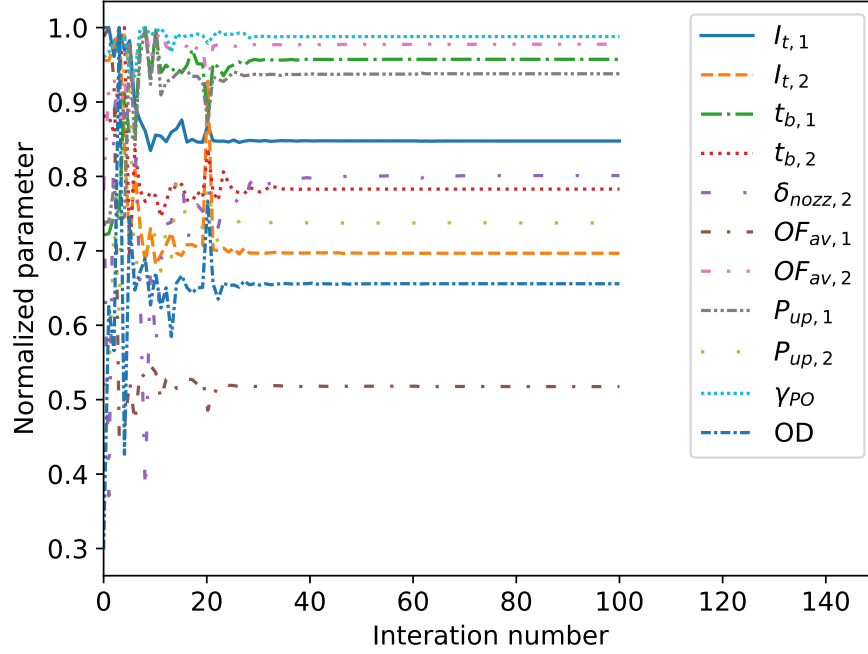
Figure 4.19: Convergence of global optimization optimization variables for LEB150 case

payload class was chosen over the 10 kg since the larger payload could be reduced by a greater amount when design variables negatively effected performance. The initial testing was also used to check if the global optimizations were converging on global optimal solutions.

The relative convergence for each design variable is presented in Fig. 4.19 for the chosen example case: LEB150. The convergence of each optimization parameter and global scalar cost function was typically reached at around 50 iterations, when 10 particles were used per design dimension. The values of each design variable were normalized by the maximum encountered, such that qualitative convergence can be presented on one figure. The global cost function convergence is shown in Fig. 4.20, with outliers near iteration number 60 attributed to variations in the optimization algorithm as it searches the solution space. One hundred iterations ensures convergence during a single global optimization.

The optimization variables that resulted in the best cost (lowest inert mass) are presented in Table 4.6. The NBB150 case did not present any viable rocket designs, which was later
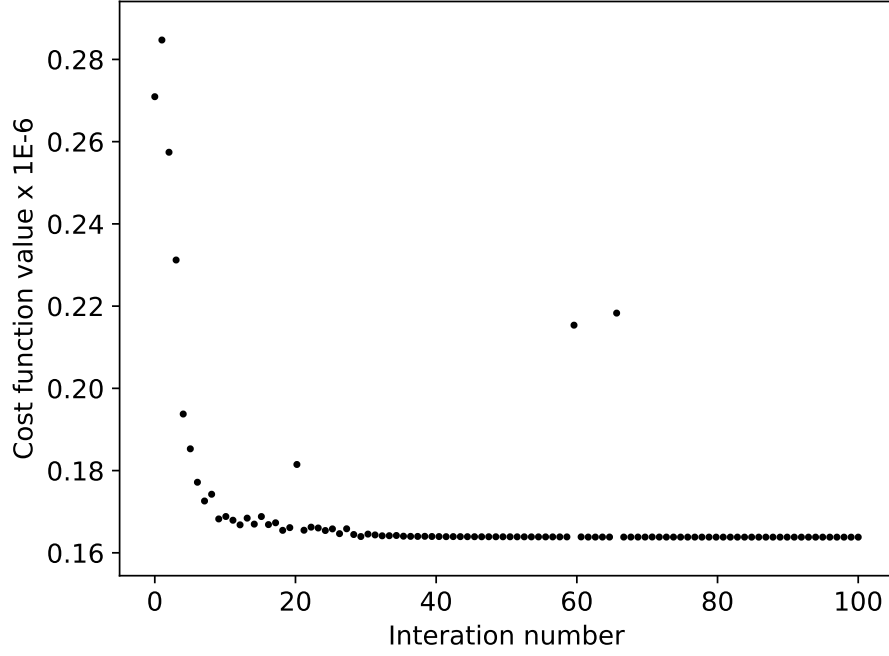
Figure 4.20: Convergence of global optimization cost function for LEB150 case

found to be due to the bounds on total impulse. All body diameters were minimized by the global optimizer. All first stage burn times are similar, within a 20 s window. The non-dimensional nozzle clearances (δ_{nozzle}) are all near 0.3. All OF_{av} values were near those that maximized I_{sp} but did not converge exactly to the optimal I_{sp} values. Optimal upstream pressure for pump-fed stages is typically greater than the values found for pressure-fed stages.

	LEE150	LEB150	LBE150	LBB150	NEE150	NEB150	NBE150	NBB150
$I_{t,1}$ (MN·s)	28.8	36.3	28.8	37.7	37.3	39.6	45.9	N/A
$I_{t,2}$ (MN·s)	6.7	7.9	9.6	11.9	7.14	9.20	9.251	N/A
$t_{b,1}$ (s)	97.7	110.0	99.7	95.6	102.7	91.6	89.6	N/A
$t_{b,2}$ (s)	273.6	379.3	359.7	382.2	374.3	328.1	233.1	N/A
δ_{nozzle}	0.341	0.310	0.379	0.296	0.301	0.281	0.303	N/A
$OF_{av,1}$	2.32	2.45	2.36	2.74	6.91	4.70	7.73	N/A
$OF_{av,2}$	2.93	3.03	2.87	3.23	6.34	5.93	6.96	N/A
$P_{up,1}$ (MPa)	1.00	1.552	1.20	1.18	1.12	1.46	0.989	N/A
$P_{up,2}$ (MPa)	1.42	1.05	1.50	0.861	0.627	0.701	1.359	N/A
γ_{po} (rad)	1.454	1.416	1.544	1.463	1.526	1.433	1.487	N/A
OD	Min.	Min.	Min.	Min.	Min.	Min.	Min.	N/A

Table 4.6: Initial global optimal values of optimization variables for 150 kg payload class

4.2.2 Sensitivity Analysis

Two types of sensitivity analyses were conducted on the initial results of the global optimization studies: parametric, and Monte Carlo. The parametric analysis explores the sensitivity of a single design parameter to the final performance (maximum payload to orbit or payload fraction) by varying it in a range around the converged value. The Monte Carlo analysis assigns normal distributions (mean and standard deviations) with physical bounds to the design variables, and within these distributions samples each design variable for given evaluations and determines the performance.

The sensitivity analysis was reduced to focusing on configurations with a single oxidizer (LOx) with the same feed system for both stages (LEE150 and LBB150). Only conducting the study on two configurations required fewer simulation batches but still assessed the respective feed systems. Liquid oxygen (LOx) was selected as the oxidizer given its higher performance, and N_2O did not present any viable pressure-fed vehicle designs initially.

During the studies, the entire vehicle design was constantly adjusted to meet all other input variables. When one input parameter was changed, the entire vehicle design was changed to meet the constraints of the other unchanged design variables and constants. For example, when combustion efficiency was changed, the total impulse and thrust were held constant, so the vehicle design physically changed. Similarly, the structures and trajectory are always

optimized/converged at a local level. The constantly changing space better isolates the influence of one parameter at a time, but is in contrast to studying static configurations of "as-built" launch vehicles.

Parametric

The impact of the upstream pressure on performance (% payload) was assessed for the first and second stages. The first and second stage chamber pressure against payload percent of gross mass is presented in Fig. 4.21 and Fig. 4.22 respectively. The upstream pressure for the pump-fed systems is the electric-pump discharge pressure, and for pressure-fed systems is the oxidizer tank pressure. The upstream pressure dictates the combustion chamber pressure, through Eqn. 3.3 and 3.4, when the equations are taken as the equality cases. The upstream pressure values are all scaled to the chamber pressure values by multiplication of a constant 1.55 factor, as described from the design methodology.
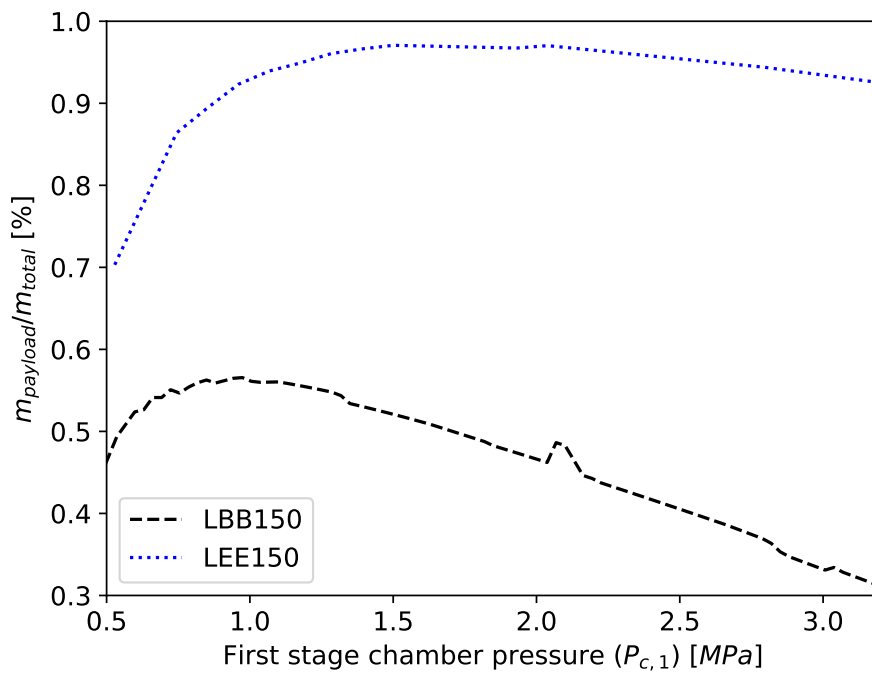
Figure 4.21: Multi-stage payload fraction sensitivity to first stage upstream pressure
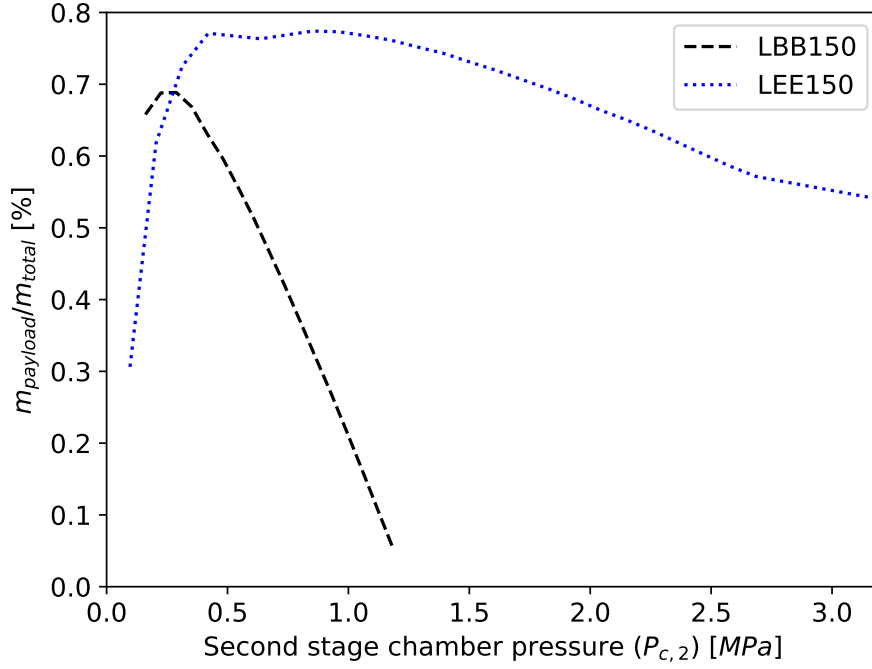
Figure 4.22: Multi-stage payload fraction sensitivity to second stage upstream pressure

The pump-fed configuration has a lower sensitivity to changing chamber pressures when compared to the back-fill system, for both stages. Changing the first stage pressures has a relatively low influence on the performance when compared to the upper stage pressures, for both feed system types. The payload fraction is highly sensitive to the upstream pressure of the second stage, and can only exist in a narrow range of upstream pressures between approximately 0.15 MPa and 1.5 MPa. The upper stage upstream optimal pressure operates near the limits of feasibility as lower pressures resulted in failure to reach the desired initial 200 km SECO-1 altitude with tolerance. For missions that require higher SECO-1 altitudes the design needs to be assessed to ensure that the vehicle can achieve the required higher altitudes, or at least can reach the desired altitude by orbital maneuvers.

The nominal payload fractions for the electric pump and back-fill cases were 0.78 and 0.55 respectively, given the design solution output by the global optimization. After reviewing the resulting performance while varying upstream pressure, it's apparent that these solutions are
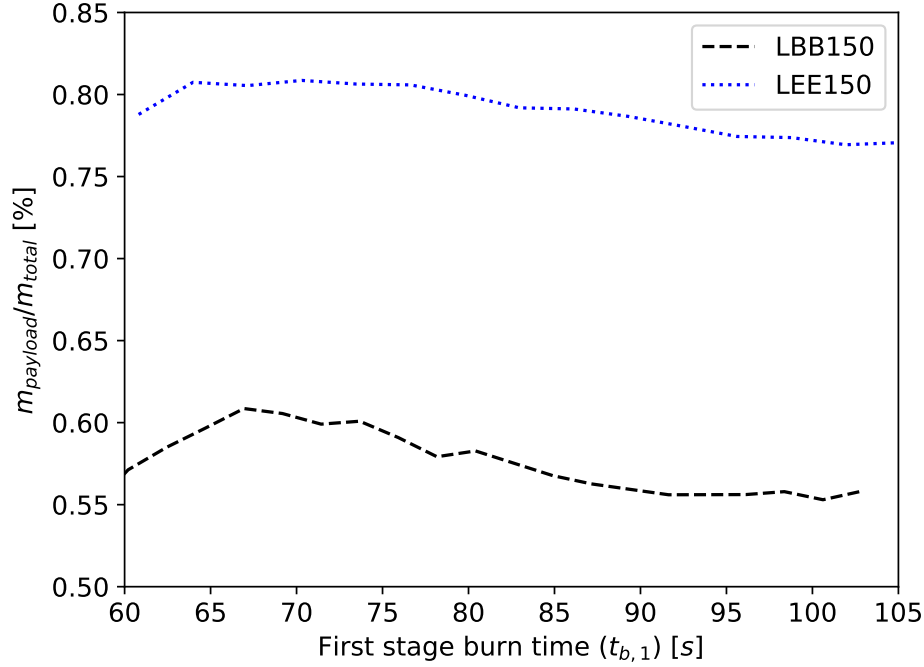
Figure 4.23: Multi-stage payload fraction sensitivity to first stage burn time

not the global optima. The global optimization scheme requires re-work, more iterations, or further PSO parameter tuning to attempt to reveal global optima. The sensitivity analysis is still conducted with the local optimal solutions of LEE150 and LBB150.

The sensitivity of payload fraction to first stage and second stage burn times for the investigated vehicle configurations is presented in Fig. 4.23 and 4.24 respectively. There is an optimal first stage burn time found around 65-70 s for both configurations, however the payload fraction was relatively insensitive to first stage burn time when compared to other investigated parameters. The burn time at a fixed total impulse mainly affects the thrust and thrust-to-weight ratio of the launch vehicles. For second stage burn times, the burn time is desired to be maximized. The constraint for the upper bound of the upper stage burn time is the failure to reach the desired SECO-1 altitude due to insufficient thrust. The lowest possible SECO-1 altitudes are desired to increase performance. Failure to reach 200 km ±15 km SECO-1 altitude occurs past 400 s for the investigated vehicles.
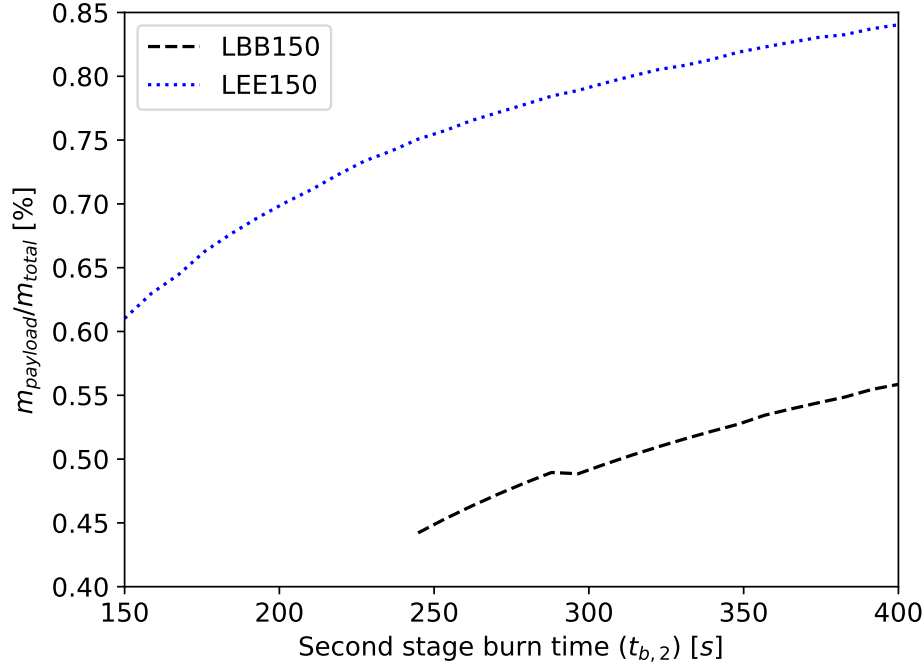
Figure 4.24: Multi-stage payload fraction sensitivity to second stage burn time

The effect of changing OF_{av} was investigated, the results are presented in Fig. 4.25 and Fig. 4.26 for the first and second stage respectively. For the first stage OF_{av}, the pump-fed case optimum is at 1.80 with a local optimum at 1.96 that matches the optimum of the back-fill case. The sharp jump in performance observed in the OF_{av} of the LEE150 case was found to be caused by the upper stage oxidizer tank end cap type changing for the required structural change as the rocket diameter decreased. The body diameter reduced because the diameter of a the fuel grains had a net decrease as they lengthened to fulfill the total thrust requirements even after matching the total impulse requirements. The smaller diameter allowed the upper stage tank end cap to change from flat to a more mass-efficient semi-ellipse. If the design space had sufficient granularity, the jump would not be present and the optimum would likely be 1.96. The optimal value for first stage OF_{av} is slightly below the value that maximizes specific impulse. The lower optimal OF_{av} finding was attributed to shifting of the OF such that the portion of flight in lower back pressure was closer to

121
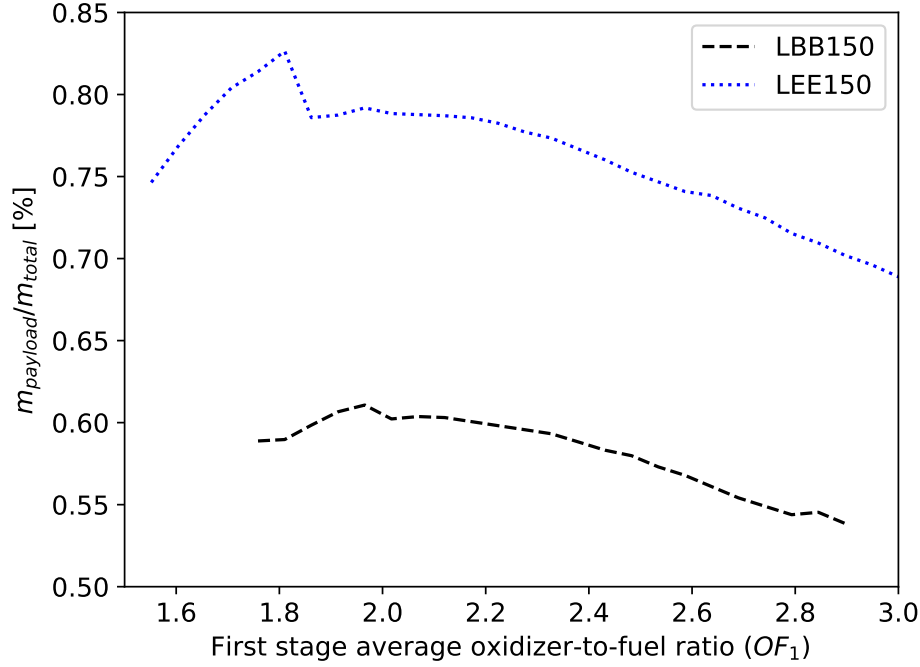
Figure 4.25: Multi-stage payload fraction sensitivity to first stage OF_{av}

optimal. The I_{sp} increases at lower back pressure, a closer to optimal OF in lower back pressure would result in better average performance.

The upper stage back-fill optimal OF matches that predicted by maximizing I_{sp} of 2.0. The pump-fed case has a slightly higher optimum near 2.2. The pump-fed configuration optimal is likely allocating more propellant mass into the relatively low pressure oxidizer tank to improve the mass efficiency.

The nozzle clearance parameter (δ_{nozzle}), which defines the upper stage nozzle exit diameter via Eqn. 3.17, has a very smooth relation to performance (Fig. 4.27). The nozzle clearance parameter trades the I_{sp} by altering nozzle expansion (area ratio), mass of the nozzle bell, and mass of the interstage via the nozzle length. The optimal design of the upper stage nozzle bell seems to be affected more by the required mass than the higher expansion caused by larger exit areas, this would change depending on the material and structural design of both the nozzle bell and interstage.
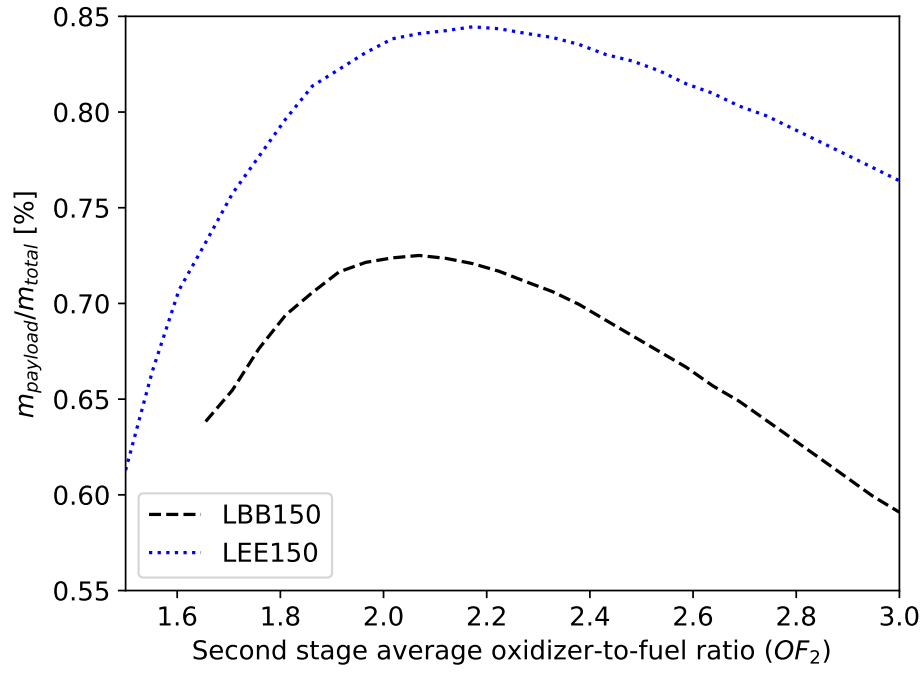
Figure 4.26: Multi-stage payload fraction sensitivity to second stage OF_{av}

Figure 4.27: Multi-stage payload fraction sensitivity to second stage nozzle clearance
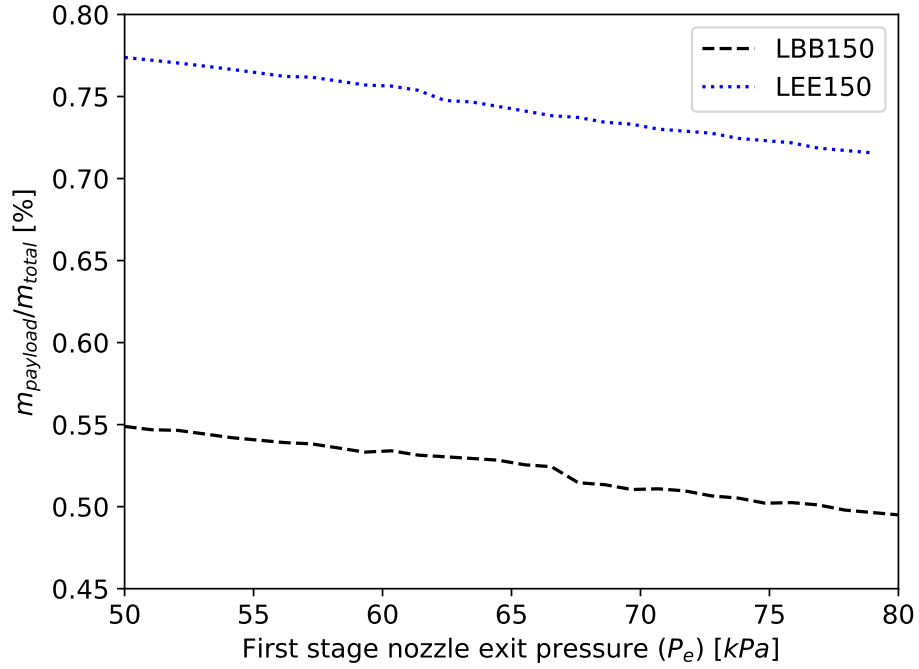
Figure 4.28: Multi-stage payload fraction sensitivity to second stage δ_{nozzle}

During the global optimizations, the first stage nozzle exit pressure design variable was set to a lowest allowable value, as the single-stage parametric studies showed that lowest permissible exit pressure was optimal. The exit pressure was set to 50 kPa in all optimization studies, as this meets the Summerfield criteria (Stark, 2005), with a margin. The sensitivity of changing back pressure to nozzle exit pressure was evaluated and found that changing back pressure affected the performance at the same rate for both feed system configurations (Fig. 4.28). For this orbital launch vehicle first stage, the lowest permissible back pressure was again found to be optimal.

The global optimizer always sought to minimize diameter. It was found that minimal body outer diameter, within constraints, was optimal for the investigated configurations (Fig. 4.29). The increase in vehicle mass was found to be the mechanism for reduced performance, the same as the single-stage studies.

The effect of initial pressurant tank pressure on payload fraction was investigated (Fig.
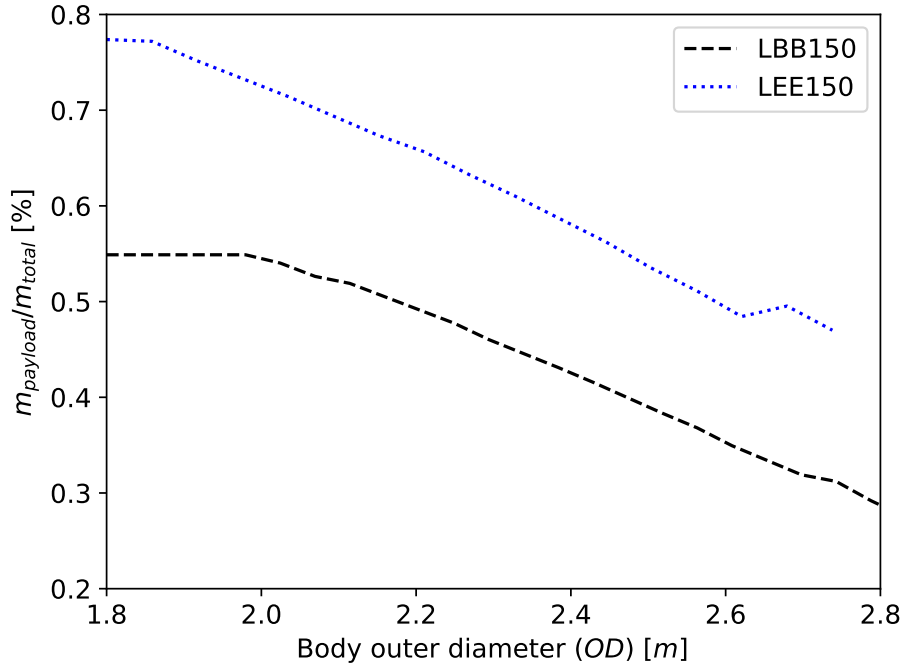
Figure 4.29: Multi-stage payload fraction sensitivity to Body OD

4.30). The same behavior was observed as in the single-stage parametric studies, maximum storage initial pressure reduced tank volume and the inert mass required to house the tank in the rocket. The % payload increased approximately by 0.05 going from 10 MPa to 40 MPa for both configurations. Increasing pressurant pressure beyond 35-40 MPa has very little influence on the performance of the investigated configurations.

The performance sensitivity was investigated for varying combustion efficiency (Fig. 4.31). The relation was found to linear with similar slope found for the investigated configurations. The payload performance was found to be highly sensitive to combustion efficiency.

The oxidizer pump efficiency was altered between 1 % and 100 %. The pump efficiency's influence on payload fraction is presented in Fig. 4.32. The payload fraction is initially very sensitive to pump efficiencies. The sensitivity transitions and performance increase becomes marginal. This plot is useful in the pump development process, showing that additional effort in improving the pump efficiency may not be worth it past certain values (70 %).

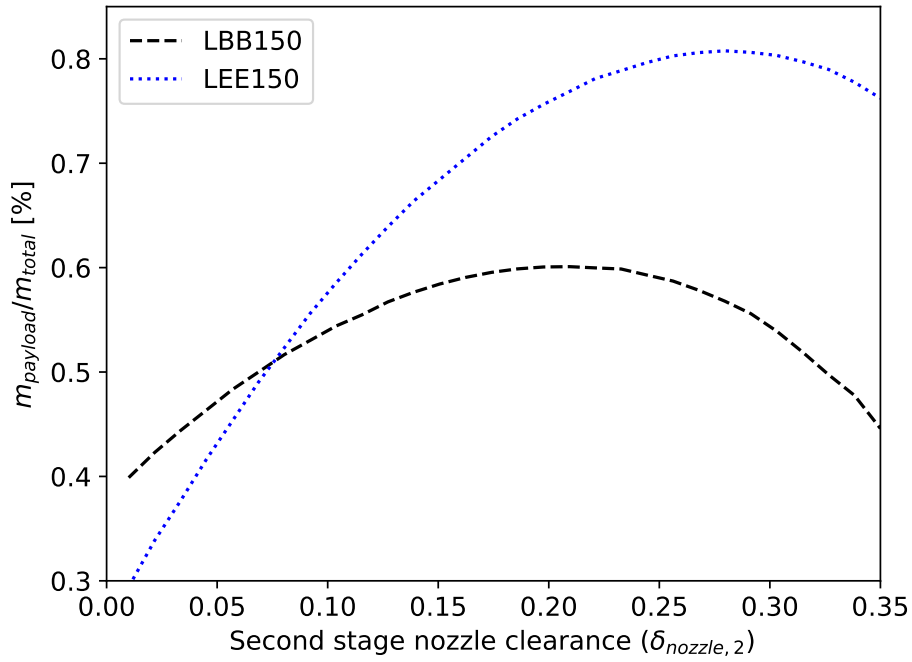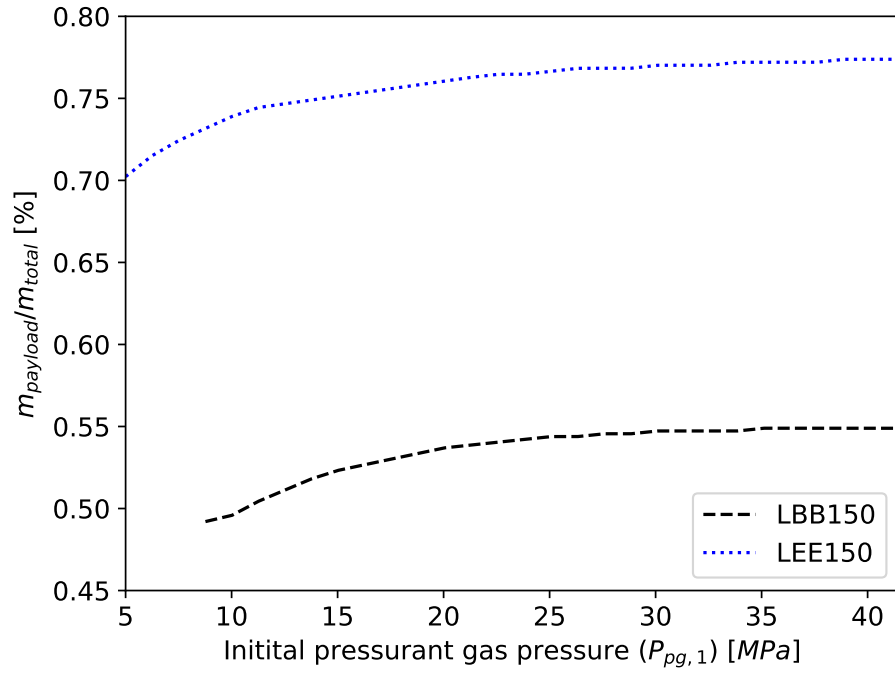Figure 4.30: Multi-stage payload fraction sensitivity to initial pressurant gas pressure
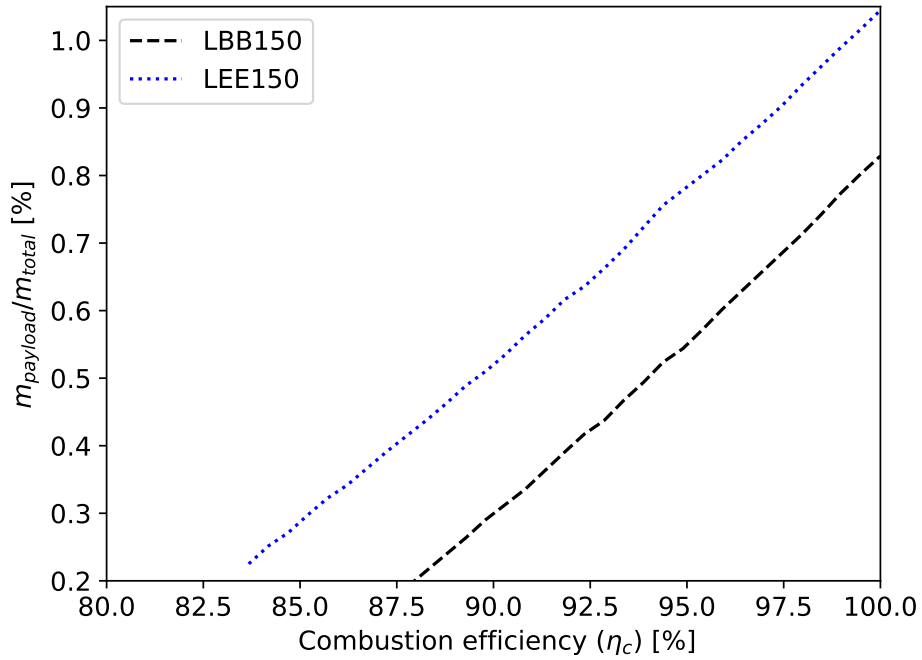
Figure 4.31: Multi-stage payload fraction sensitivity to combustion efficiency
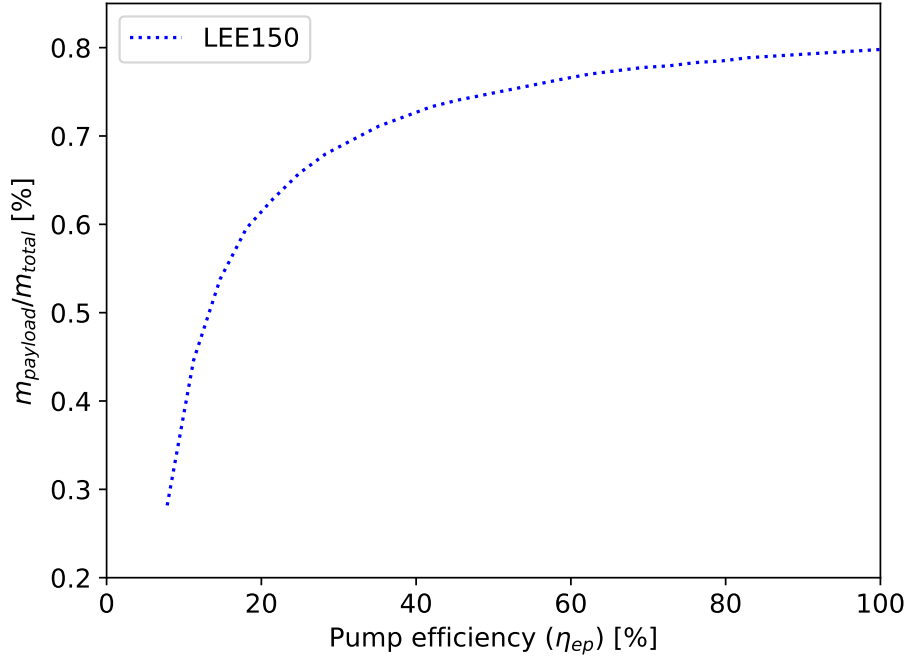
Figure 4.32: Multi-stage payload fraction sensitivity to electric pump efficiency

The battery index is an introduced parameter and used to assess the sensitivity of changes in the battery performance to vehicle performance. The battery index a factor multiplied by the battery power density (δ_{bp}) and battery energy density (δ_{be}). The batteries are either power-limited or energy-limited during operation. Studying solely power density and separately energy density was initially done, but performance increase was always capped by the other unchanged density. Altering both at once showed a more meaningful relation of the battery technology performance's impact on vehicle performance. The battery for LEE150's first stage was found to be power limited while the second stage was found to be energy limited. The battery index's influence on overall performance is shown in Fig. 4.33

The structural index is another introduced parameter. It was introduced to assess the sensitivity of vehicle performance to the structural efficiency (Fig. 4.34). The structural index is a factor multiplied to every safety factor of every structural element on the vehicle. The original safety factors are shown in table B.1 in the appendix. It can be viewed as a
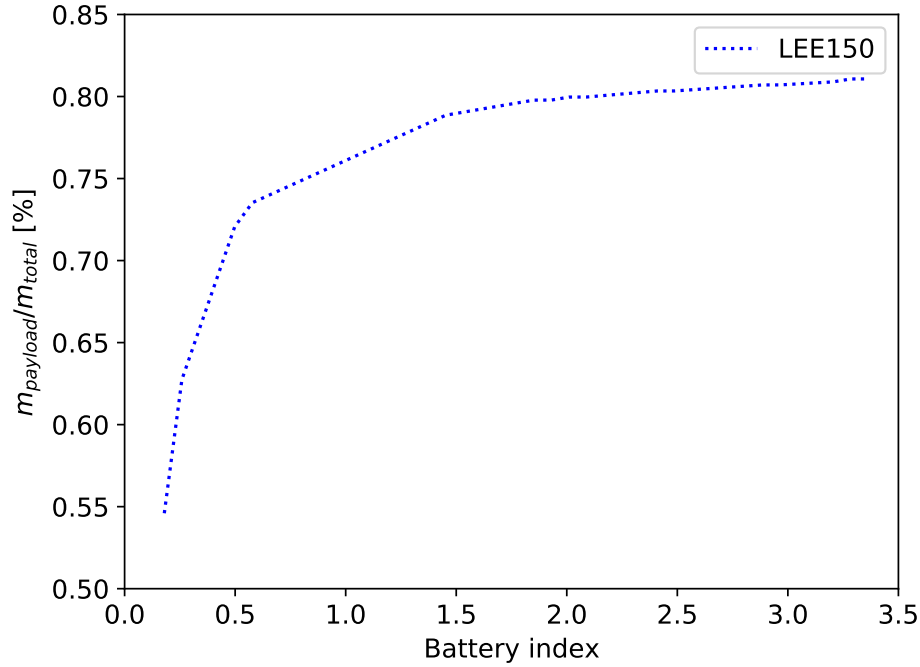
Figure 4.33: Multi-stage payload fraction sensitivity to electric battery multiplier

changing all material's strength-to-weight ratio ($\sigma_{allow}/\rho_{material}$) or stiffness-to-weight ratio by the same factor simultaneously. Since a majority of the structures were modeled as 2024-T6, the performance of using different materials can be approximated by multiplying a new material's strength-to-weight ratio to that of 2024-T6 to find structural index. Caution must be used for the approximate method, as buckling-limited failure modes are a function of stiffness rather than yield strength, and the Youngs modulus of materials does not change drastically between grades as yield strength does. For the most accurate conceptual analysis, with changing material, the material needs to selected or added directly to the code base.

The sensitivity of performance to structural efficiency was higher for the back-fill systems as the oxidizer tank is under higher pressure than the pump-fed cases, so a the same increase in safety factor is a larger increase in mass. Both configurations present different slopes in Fig. 4.34 and would converge on a payload fraction, somewhere below a structural index of 0.5.
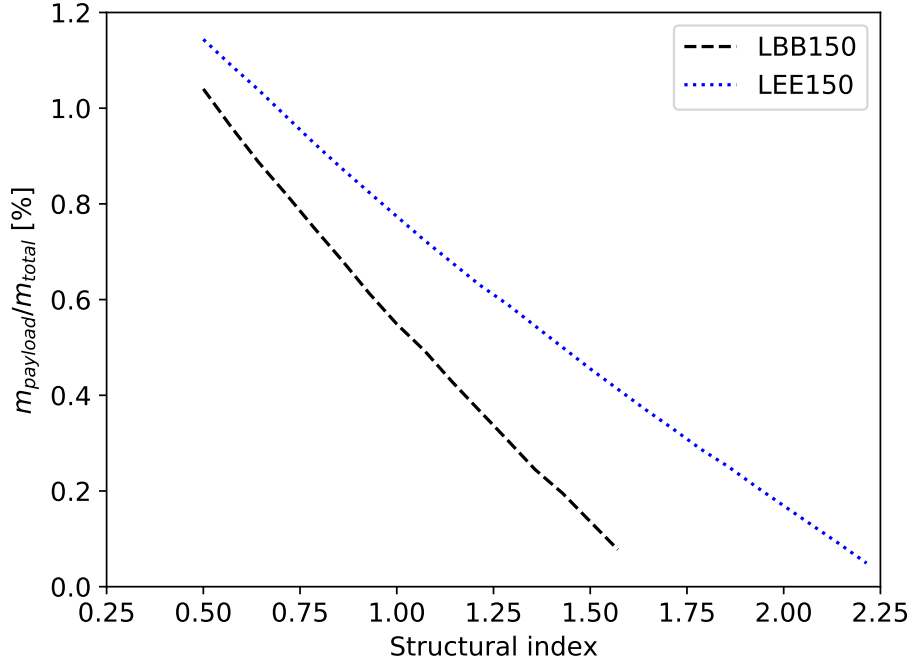
Figure 4.34: Multi-stage payload fraction sensitivity to structural index

In all the parametric analyses, the first stage parameters typically had lower influence on the overall performance (t_b, P_{up}, OF_{av}). To better illustrate why the first stage design parameters had lower sensitivity to performance, the effect of adding inert point mass to the first stage inter-tank to the deliverable payload was investigated (Fig. 4.35). Inert mass, between 0 and 250 kg was added. The sensitivity for both configurations appeared to be between 15 and 20 kg/kg. Put differently, 15 kg can be added to the first stage before you lose 1 kg of payload mass, for this scale and these particular configurations.

Monte Carlo

A Monte Carlo analysis was conducted for the design variables with normal distribution outlined in Table 4.7 for LEE150 and LBB150. One hundred vehicle design instances were generated randomly from the distributions. Approximately 10 instances from each case resulted infeasible designs and did not reach orbit and are not included. The pump-fed
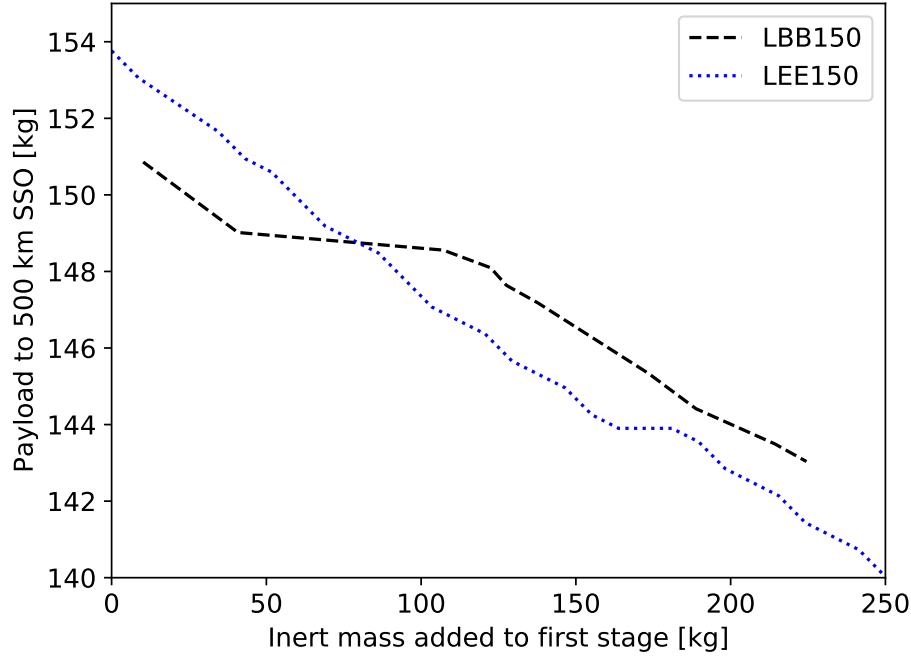
Figure 4.35: Multi-stage payload fraction sensitivity to first stage additional mass

configurations appeared to have a higher average payload fraction and tighter distribution of payload fraction (Fig. 4.36). While the back-fill systems have a higher sensitivity to the same design variable distributions and lower average payload fraction (Fig. 4.37).

4.2.3   Refined Global Optimization Batch Results

The sensitivity analysis revealed that the optima converged upon in the initial global optimizations were not the true global optima, but a local optimal solution. The particle swarm parameters in Table 3.7 were refined using a grid search study (PSO parameter sweep).

Particle Swarm Parameter Refinement

A PSO parameter sweep was conduced in order to tune the algorithm using different PSO constants. The initial constants, in Table 3.7, were used as these gave good results during a preliminary assessment. It was found that the same PSO constants did not produce global

Input variable	Mean	Standard deviation	Lower bound	Upper bound
$I_{t,1}$	Nominal Value	5 % of Nominal	None	None
$I_{t,2}$	Nominal Value	5 % of Nominal	None	None
t_b	Nominal Value	5 % of Nominal	None	None
t_b	Nominal Value	5 % of Nominal	None	None
γ_{po}	Nominal Value	5 % of Nominal	None	$\pi/2\ rad$
$OF_{av,1}$	Nominal Value	10 % of Nominal	None	None
$OF_{av,2}$	Nominal Value	10 % of Nominal	None	None
$P_{up,1}$	Nominal Value	5 % of Nominal	None	None
$P_{up,2}$	Nominal Value	5 % of Nominal	None	None
P_e	Nominal Value	5 % of Nominal	None	None
δ_{nozzle}	Nominal Value	5 % of Nominal	None	None
η_c	0.95	0.05	0	1
η_p	0.66	0.05	0	1
Battery index	1	0.01	0	None
Structural index	1	0.25	0.5	1.5
extra mass, stage 1	10	20	None	None

Table 4.7: Values and bounds assumed for Monte Carlo analysis
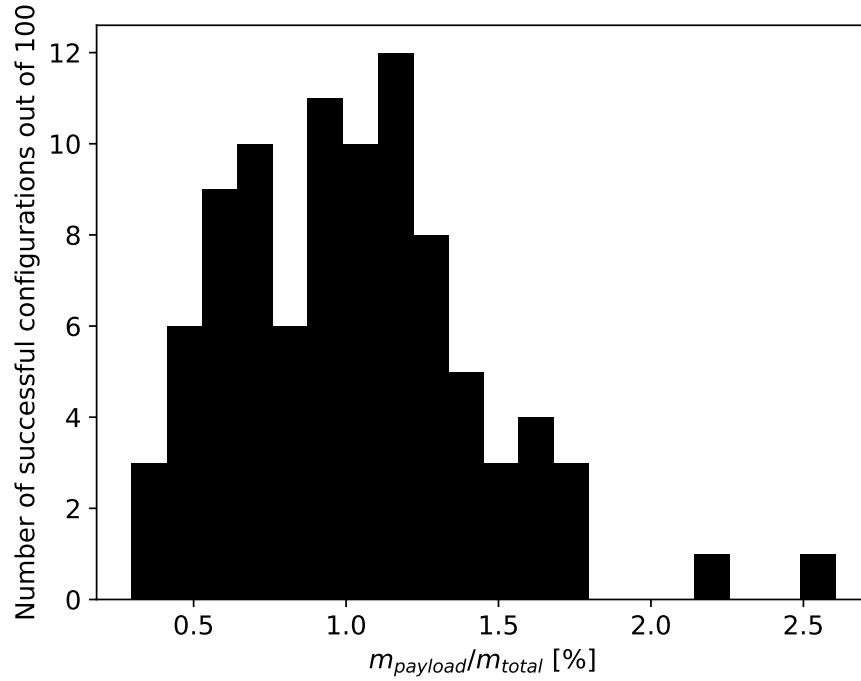
Figure 4.36: LEE150 Monte Carlo % payload distribution
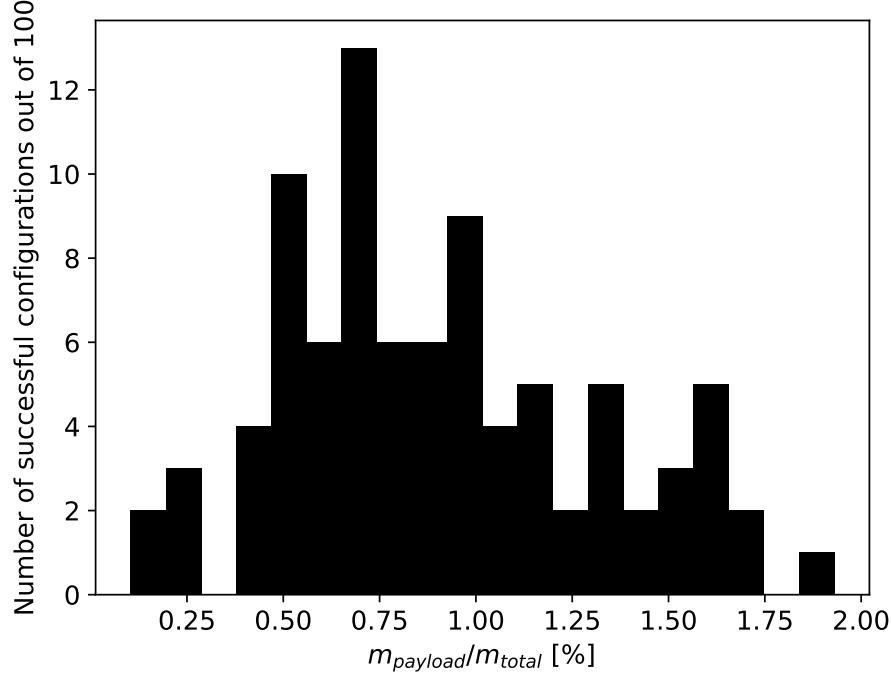
Figure 4.37: LBB150 Monte Carlo % payload distribution

optima during the multi-stage studies since better solutions were found during brute-force parameter sweeps.

A grid search was used to tune the PSO parameters for LEE150. The LEE150 case was chosen so that the solutions could be compared to the sensitivity parametric analysis solutions. The parameters c_1, c_2, and w were either 0.25, 0.5, or 1.5. The grid had 27 (3^3) entries but the [0.5,0.5,0.5] case was omitted as it was close to the initially used values. Each set of PSO parameters within the grid search was given three attempts. The three attempts were used to observe the relative behavior for different random initial conditions. It was desired to observe similar behavior independent of random particle starting position and velocity. The results of the PSO grid search are displayed in Table 4.8. The dry mass was reported to indicate the solution performance. The cost function always reduced to a sole function of dry mass at the end of the optimizations, with negligible propellant residual on the order of 10 m/s of ΔV. The SECO-1 altitude, staging altitude, and positive propellant

remainder error weights were sized to be sufficiently large so that they were never violated in the final solution. The dry masses in Table 4.8 can be converted to cost function values by multiplying by 100. It was found that weighting the social and cognitive parameters relatively high with a lower particle mass resulted in the best consistency between attempts as well as very good global solutions. The payload fractions that were a result of the best global solutions surpassed the maximum encountered in the parametric analysis (when only considering the optimization variables). The highest payload fraction for LEE150 in the global optimization was 1.20 % while the highest found during the sensitivity analysis was 0.97 %, when only considering the optimizable variables. The 0.97 % payload for LEE150 was initially found during the first stage upstream pressure parametric sensitivity analysis.

Solutions using $[c1{:}1.5, c2{:}1.5\ w{:}0.25]$ found the minimum dry mass of the a LEE150 case to be 1350 kg, within a 100 kg window for three attempts, and the best was within 10 kg dry mass of the overall best. The overall best was found using $[c1{:}0.5, c2{:}1.5\ w{:}0.5]$ but was not reliably found from the other attempts for the same PSO parameters. The PSO parameters: $[c1{:}1.5, c2{:}1.5\ w{:}0.25]$ showed the most promise and were used going forward. If time permitted, further refinement of the PSO parameters would be investigated with lower particle mass and higher cognitive and social constants.

The best cost function of a generation, for the $[c1{:}1.5, c2{:}1.5\ w{:}0.25]$ LEE150 cases, for each iteration number is plotted in Fig. 4.38. The plot is a result of three independent concurrent global optimization runs. All three runs converged to within a 100 kg window for the vehicle dry mass. The plot presents more noise than the previous convergence plot (Fig. 4.20). The noise is a result of the higher acceleration and sporadic particle movement. It was initially thought that higher particle weight (inertia) would prevent local optimal convergence, but that was not observed.

Dry Mass [kg]	$[c_1, c_2, w]$
1858	[0.5, 0.5, 0.25]
1625	[0.5, 0.5, 1.5]
1595	[0.5, 0.25, 0.5]
1542	[0.5, 0.25, 0.25]
1756	[0.5, 0.25, 1.5]
1340	[0.5, 1.5, 0.5]
1425	[0.5, 1.5, 0.25]
1553	[0.5, 1.5, 1.5]
1632	[0.25, 0.5, 0.5]
1712	[0.25, 0.5, 0.25]
1674	[0.25, 0.5, 1.5]
1986	[0.25, 0.25, 0.5]
2061	[0.25, 0.25, 0.25]
1734	[0.25, 0.25, 1.5]
1569	[0.25, 1.5, 0.5]
1498	[0.25, 1.5, 0.25]
1865	[0.25, 1.5, 1.5]
1849	[1.5, 0.5, 0.5]
1533	[1.5, 0.5, 0.25]
1811	[1.5, 0.5, 1.5]
1629	[1.5, 0.25, 0.5]
1553	[1.5, 0.25, 0.25]
1699	[1.5, 0.25, 1.5]
1390	[1.5, 1.5, 0.5]
1350	[1.5, 1.5, 0.25]
1696	[1.5, 1.5, 1.5]

Table 4.8: Global optimization results for LEE150 with different PSO parameters
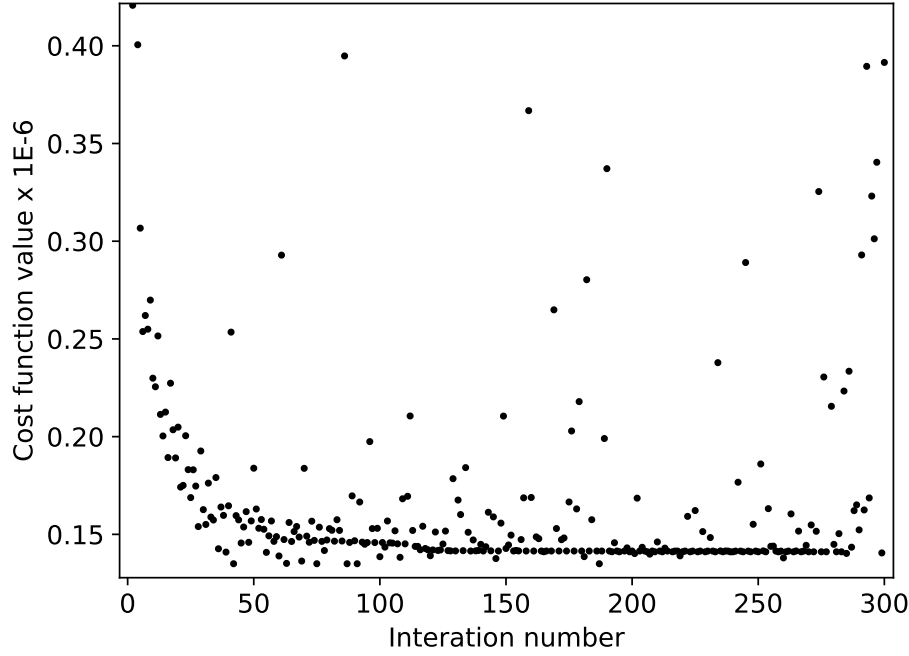
Figure 4.38: LEE150 convergence using $[c_1 : 1.5,\ c_2 : 1.5,\ w : 0.25]$

Test Matrix Results

Three optimizations attempts were made, using PSO parameters $[c_1 : 1.5,\ c_2 : 1.5,\ c_4 : 0.25]$, for each configuration in the test matrix (Table 4.4). The best of the three attempts for each configuration is presented in Tables 4.9 to 4.12. The bounds on total impulse were increased and entirely-pressure-fed N_2O configurations were found.

The results of using the refined PSO parameters show consistent behavior between the scales (payload classes) and configurations. Payload fractions were found less sensitive to the feed systems considered, compared to different payload classes and oxidizers used. Typically, the electric pump first stage and back-fill second stage configurations were superior with the exception of the 150 kg payload class using LOx oxidizer.

The optimal upper stage upstream pressures were typically lower than the first stage upstream pressures, particularly when the upper stage was pressure-fed. The lower pressures of the upper stage are closer to the values that maximized ΔV in the single-stage parametric

135

	LEE150	LEB150	LBE150	LBB150
Total impulse 1 [MN·s]	19.7	18.4	22.3	18.3
Total impulse 2 [MN·s]	4.55	6.76	4.16	6.02
Burn time 1 [s]	114.6	96.0	108.4	85.4
Burn time 2 [s]	493.2	316.3	323.5	327.6
Nozzle clearance	0.287	0.222	0.285	0.151
Average OF 1	2.11	2.43	2.08	2.30
Average OF 2	2.73	2.49	2.35	2.45
Upstream pressure 1 [MPa]	1.55	1.28	1.02	1.26
Upstream pressure 2 [MPa]	1.27	0.51	1.02	0.21
Pitch-over angle [°]	84.41	87.25	88.05	83.02
Bilinear tangent χ constant	-0.422	-0.479	-0.529	-0.543
Bilinear tangent c constant	0.651	0.833	0.906	0.908
Bilinear tangent b constant	0.862	0.817	0.782	0.774
Gross take-off mass [kg]	12488	13308	15060	13205
Propellant mass [%]	89.2	88.4	88.6	86.9
Paylaod % of GTOM	1.20	1.13	1.00	1.14
Outer diameter [m]	1.58	1.57	1.70	1.54
Length [m]	18.1	20.4	19.5	20.9

Table 4.9: Global optimization results of LOx systems with 150 kg payload

	NEE150	NEB150	NBE150	NBB150
Total impulse 1 [MN·s]	30.3	28.1	32.4	30.0
Total impulse 2 [MN·s]	7.30	5.94	7.15	6.69
Burn time 1 [s]	92.3	80.6	72.9	94.6
Burn time 2 [s]	210.9	364.5	242.8	392.0
Nozzle clearance	0.273	0.241	0.237	0.251
Average OF 1	5.64	5.80	5.61	6.00
Average OF 2	7.30	6.68	6.16	6.05
Upstream pressure 1 [MPa]	1.29	1.44	1.31	1.47
Upstream pressure 2 [MPa]	0.864	0.202	0.651	0.283
Pitch-over angle [°]	86.04	83.00	86.04	85.13
Bilinear tangent χ constant	-0.434	-0.690	-0.656	-0.503
Bilinear tangent c constant	0.690	0.935	0.928	0.901
Bilinear tangent b constant	0.852	0.682	0.699	0.798
Gross take-off mass [kg]	21850	19723	23507	21465
Propellant mass [%]	90.2	89.8	88.2	88.1
Paylaod % of GTOM	0.69	0.76	0.64	0.70
Outer diameter [m]	1.84	1.76	1.82	1.83
Length [m]	21.3	20.8	22.7	21.6

Table 4.10: Global optimization results of N$_2$O systems with 150 kg payload

	LEE10	LEB10	LBE10	LBB10
Total impulse 1 [MN·s]	2.86	2.43	3.26	2.70
Total impulse 2 [MN·s]	0.738	0.632	0.878	0.689
Burn time 1 [s]	104.3	86.4	90.4	88.5
Burn time 2 [s]	377.4	388.9	320.6	398.0
Nozzle clearance	0.253	0.312	0.339	0.332
Average OF 1	2.52	2.10	2.46	2.18
Average OF 2	2.81	2.38	2.77	2.38
Upstream pressure 1 [MPa]	1.75	1.17	1.24	1.10
Upstream pressure 2 [MPa]	0.58	0.21	0.92	0.29
Pitch-over angle [°]	85.40	84.03	84.44	82.79
Bilinear tangent χ constant	-0.445	-0.611	-0.505	-0.550
Bilinear tangent c constant	0.724	0.922	0.901	0.910
Bilinear tangent b constant	0.844	0.733	0.797	0.770
Gross take-off mass [kg]	1847	1664	2270	1888
Propellant mass [%]	88.2	89.3	87.8	88.3
Paylaod % of GTOM	0.54	0.60	0.44	0.53
Outer diameter [m]	0.91	0.86	0.95	0.89
Length [m]	9.5	9.1	10.0	9.5

Table 4.11: Global optimization results of liquid oxygen systems with 10 kg payload

	NEE10	NEB10	NBE10	NBB10
Total impulse 1 [MN·s]	5.48	4.36	5.95	4.66
Total impulse 2 [MN·s]	1.12	0.765	1.22	0.783
Burn time 1 [s]	88.2	92.3	85.8	77.4
Burn time 2 [s]	266.0	383.5	284.7	439.8
Nozzle clearance	0.301	0.302	0.302	0.212
Average OF 1	7.19	5.37	5.36	5.47
Average OF 2	5.88	7.85	7.65	6.21
Upstream pressure 1 [MPa]	1.40	1.31	1.07	1.37
Upstream pressure 2 [MPa]	1.06	0.22	0.54	0.20
Pitch-over angle [°]	86.26	85.78	88.31	82.18
Bilinear tangent χ constant	-0.524	-0.561	-0.589	-0.693
Bilinear tangent c constant	0.905	0.912	0.918	0.936
Bilinear tangent b constant	0.786	0.763	0.746	0.680
Gross take-off mass [kg]	3845	3043	4430	3278
Propellant mass [%]	89.5	90.0	89.1	87.4
Paylaod % of GTOM	0.26	0.33	0.23	0.31
Outer diameter [m]	1.14	1.08	1.18	1.06
Length [m]	11.0	10.1	11.6	11.0

Table 4.12: Global optimization results of N_2O systems with 10 kg payload

studies. The higher pressures for first stages may have been necessary for sufficient thrust-to-weight ratios, as upper stages exhibited lower thrust-to-weight ratios (longer burn times). The first stage oxidizer tanks were found to have thicker walls for the loss of pressure on pad failure mode. The required thicker walls naturally support larger pressures, that the optimizer may have taken advantage of, if the additional combustion chamber structure mass was not detrimental.

Propellant mass percentages were found to be similar between the two scales investigated and the same propellants. The requirement to have similar propellant mass fractions between scales can be seen approximately through the rocket equation (Eqn. 3.1). The specific impulse and inert mass trades are similar between scales such that specific impulse is approximately constant across scales and this dictates the propellant mass percentages, since the missions are the same. However, the payload fraction improves as scale is increased since constant mass models are employed for some auxiliary components, and as payload increases it overshadows the auxiliary and smaller-mass component masses.

Nitrous oxide configurations, had approximately half the payload mass fraction compared to LOx-based configurations. The vehicle geometric scale was approximately equal between configurations. The denser N_2O configuration are possible since the higher OF leads to more propellant allocated in volume-efficient cylindrical tanks. Increasing performance of the LOx-based systems could be accomplished with an upper stage diameter reduction to improve mass efficiency, this is suggested for future work.

4.2.4 Detailed Output for LEE150

Detailed results of the LEE150 optimal design are presented. The goals of presenting the detailed results are to assess the capability and outputs of the conceptual design framework. The LEE150 case was selected as it was the highest performing configuration. All plots are plotted until SECO-1, which occurred at approximately 600 s after launch. The downrange distance vs altitude is plotted in Fig. 4.39. The down-range distance is the arc length of
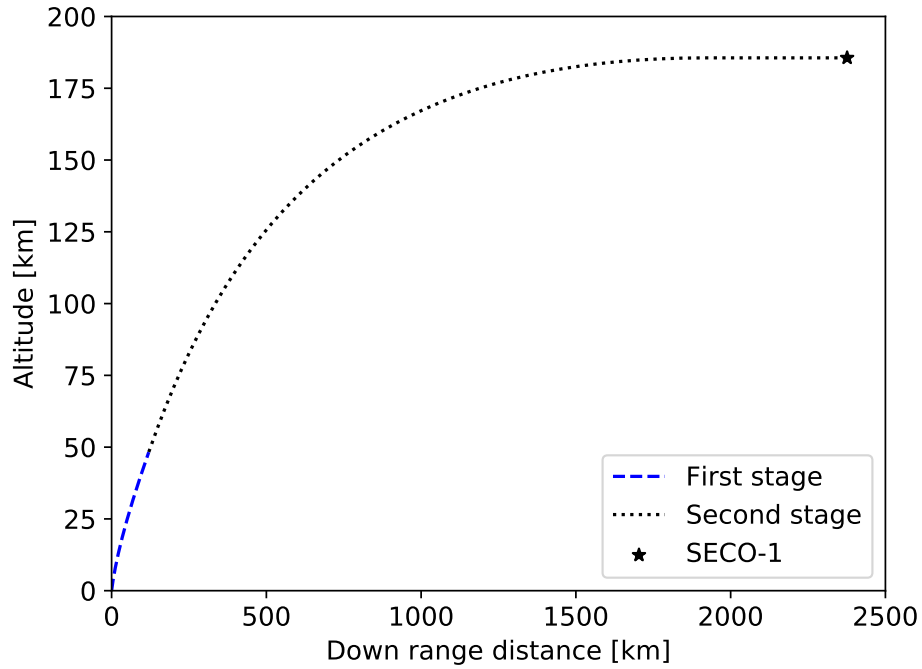
Figure 4.39: Altitude vs Downrange distance for LEE150

the flight path's projection onto Earth's surface. The staging altitude is near 50 km. The staging altitude is consistent with all investigated launchers in the test matrix (Table 4.4) where staging occurred above 50 km.

The altitude time history, presented in Fig. 4.40, inflects when staging occurs. The inflection point is caused by the differences in the vehicle's accelerations due to the respective nominal thrust-to-weight ratios. The upper stage also has a more aggressive steering program, by design, to guide the flight path more horizontal (tangent to Earth's surface). The final altitude is slightly above the 185 km minimum (the 200 km set point with 15 km allowed deviation).

Inspecting the velocity vs time plot (Fig. 4.41), the first stage supplies a smaller portion of the required ΔV, and the rate of change of second stage velocity is less due to the smaller upper stage acceleration (Fig. 4.42). The initial second stage acceleration is negative due to the small amount of drag experienced during the 1 s coast before second stage ignition.
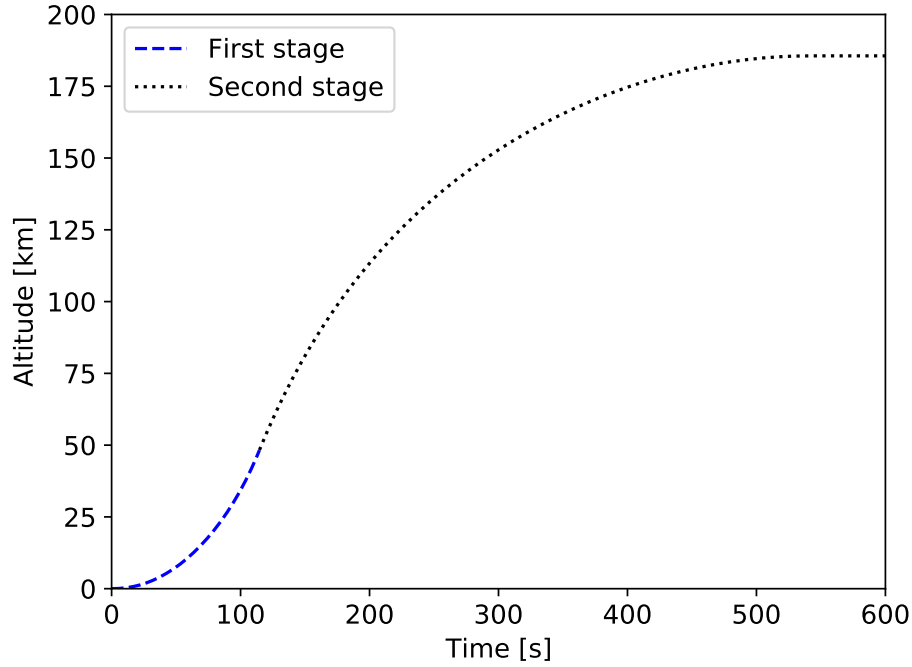
Figure 4.40: Altitude vs time for LEE150

The initial first stage acceleration is within typical ranges of orbital launch vehicles, as some have liftoff thrust-to-weight ratios between 1 and 1.5 (Hammond, 2001).

Supplementary information for the LEE150 mission and full code output are supplied in the appendix C. One thing to note from the detailed code output are the values of the cylindrical section wall thicknesses. The cylindrical section wall thicknesses, encountered in the design process, for the 150 kg payload class, were found to be in the mm range. Having structural thickness in the mm range is commonly accomplished on launch vehicles (Larson and Wetrz, 1999). However as the vehicles scaled down, several thicknesses became sub-mm in the range of tenths of a mm. Such small structures are employed on launch vehicles (Bruno, 2019), but require extra manufacturing and handling. The minimum thickness handling and manufacture constraints for materials are likely going to be design constraints that come in through detailed design and manufacturing stages that limit the theoretical performance of the launch vehicles.

Figure 4.41: Velocity vs time for LEE150

Figure 4.42: Acceleration vs time for LEE150

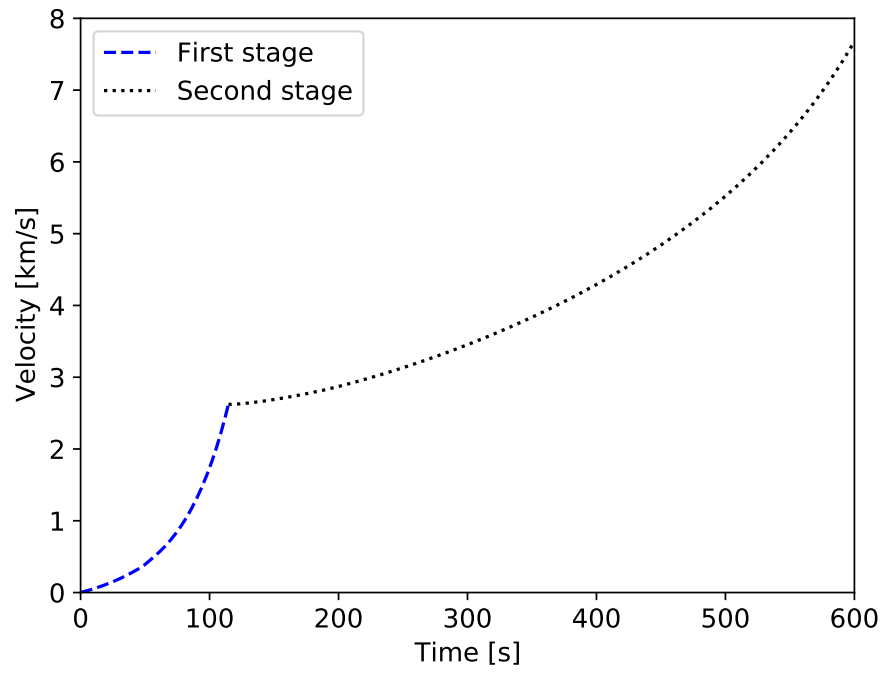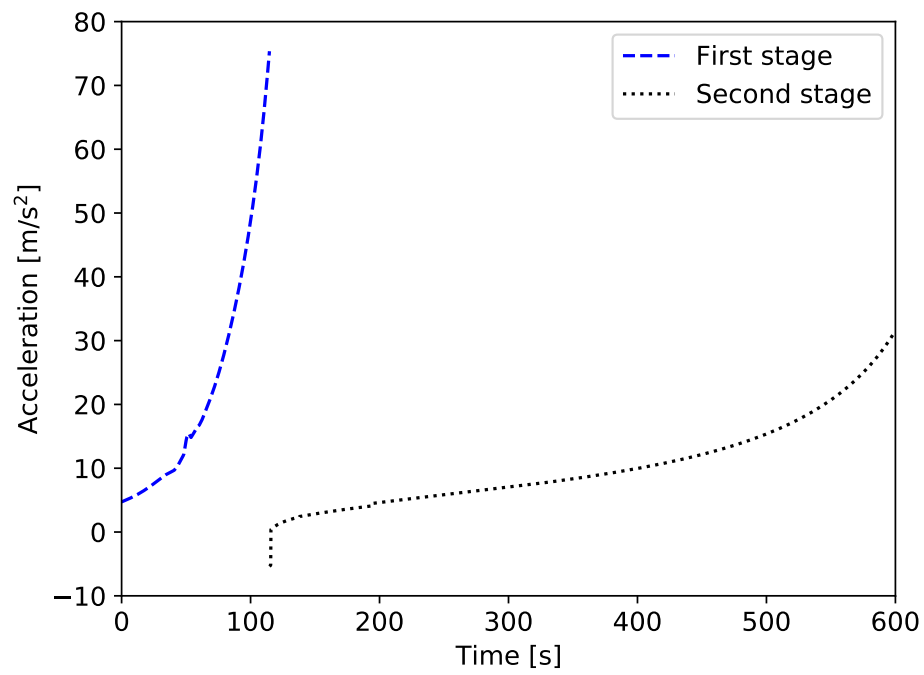|	LEE150 first stage	LEE150 second stage
Average I_{sp} [s]	243	307
m_0 [kg]	12488	1858
m_f [kg]	2691	262
ΔV [m/s]	3659	5896

Table 4.13: Parameters from LEE150 used to calculate ΔV

Comparison to the Rocket Equation

A comparison was conducted of the LEE150 case against the prediction of the rocket equation (Eqn. 3.1). The theoretical ΔV values from the first and second stage are summed to determine total ΔV. The initial and final mass properties of both stages, average specific impulse, and rocket equation ΔV, are presented in Table 4.13. Both stages have a very low inert mass, which is due to the low system pressures. For the first stage system (without second stage masses), the ratio of inert mass, to inert mass plus propellant mass, is 7.8 %. The ratio of upper stage inert mass (minus payload mass), to inert mass (minus payload mass) plus propellant mass, is 6.6 %. The inert mass fractions are lower than typical values for existing launch vehicles (Hammond, 2001). The upper stage delivers a higher I_{sp} due to lower ambient pressure and a vacuum-optimized nozzle. When the ΔV calculated using Eqn. 3.1 of 9.6 km/s is compared to the final orbital velocity of 7.8 km/s, the ΔV losses can be calculated. The ΔV amount to 1.8 km/s.

The Effect of Additional OF Shift

The effect of an additional OF shift due to a port diameter correction for the regression model (Eqn. 3.22) was investigated. The correction adjusts Eqn. 3.22 such that the fuel surface regression rate decreases with an increase in fuel port diameter and is proportional to $ID_f^{-0.2}$ (Cai et al., 2013). The LEE150 optimal design parameters were reused with the new regression formulation to generate a vehicle design. It was found that the additional OF shift resulted in a less than 1% reduction of delivered specific impulse and negligible impact on deliverable payload fraction.

Chapter 5

Conclusions and Recommendations

5.1 Conclusions

This study found that two-stage payload delivery to low Earth orbit was conceptually feasible for hybrid rocket propelled electric pump-fed and pressure-fed vehicles using either N_2O/paraffin or LOx/paraffin propellants. Entirely back-fill-pressure-fed systems were found to have conceptual design solutions for two-stage-to-orbit payload delivery. The performance of the electric-pump feed system configurations was found to be relatively insensitive to technological improvements beyond the values used from current literature. The pressure-fed configurations had comparable payload fractions to pump-fed configurations. The finding of feasible two-stage pressure-fed designs was surprising, as the inert mass was expected to be too high and Miranda (2015) found no feasible solutions.

Design variables were found where the optima occurred on extreme ends. For optima at extreme ends, limiting bounds were chosen from design constraints and practical limits. For variables that exhibited mid-range optimal solutions, a tuned global particle swarm optimization algorithm found high-performing design solutions that traded all multi-disciplinary design variables in the reduction of dry vehicle mass for a given payload mass. It was found that the upper stages were most sensitive to all design variables compared to first stages.

The effects of additional inert mass or propulsion system efficiency is directly impacting the performance of second stage/ payload mass.

The main research question of this thesis was to what extent can orbital-class HRE-based launchers be scaled down? The minimum mass configurations were found with LOx-based systems compared to N_2O-based systems of the same payload class. However the geometric size of the vehicle was approximately the same between N_2O and LOx systems, N_2O systems were denser. Payload fractions improved, across the different configurations, as the vehicle became larger to support larger payloads. The smallest gross vehicle mass, found for the 150 kg mission, was 12488 kg for a dual electric pump LOx/paraffin system. For the 10 kg payload class, the minimum wet mass was found to be 1664 kg for LOx/paraffin system with an electric pump-fed first stage and back-fill-pressure-fed stage second stage.

5.2 Future Work

A possible area of future work is the analysis of hybrid rockets using different engine cycles. The first-stage performance could be improved by incorporating an air-breathing aspect. The various engine cycles, integrated with vehicle design, could greatly improve the vehicle performance. The improved performance may bring down vehicle size and complexity or offer enough margins for, at least first stage, landing and re-use. Recent work, found in this thesis's literature review, have explored fully or partially reusable launch vehicle conceptual design. Re-use of hybrid rockets is an area not found in the literature surveyed for this work.

A possible addition to modeling is including the effects of throttling the oxidizer flow rate. Throttling may further optimize vehicle performance, as limiting max q and/or maximum acceleration would reduce aerodynamic loads and inert mass while trading-off propulsive performance. This was suggested by Miranda (2015) but was not explored here.

Other modeling implementation includes the option to have different outer diameters of each stage. The diametrical changes would potentially increase performance of launch

vehicles by reducing inert mass. This would require generalizing the aerodynamics beyond ogive-cylinder or conic-cylinders in the current modeling.

Exploring the use of an arbitrary number of rocket stages, most likely three, would be useful to determine the vehicle size of three-stage configurations. The potential size reduction could be weighed with the relative complexity of another stage separation event.

The current formulation can only deal with materials whose strength can be predicted using von Mises failure criteria. Adding composite material structural modeling, namely failure modes and material properties, would greatly improve the capability and show the relative benefits of composite structures.

The temperature dependence of material properties would be another potentially useful level of fidelity to include in the structural modeling section. The strength of materials changes over temperature ranges, the experienced material temperatures (both external internal and gradients) may have a non-negligible influence on vehicle inert mass.

Estimating the cost (in dollars) of components, given their size, can be completed using cost estimating relationships. Quantifying vehicle cost can be used to assess different vehicle configurations.

References

Akins, D. (2003). *Akin's Laws of Spacecraft Design.* https://spacecraft.ssl.umd.edu/akins_laws.html.

Altman, D. (1991). Hybrid rocket development history. In *27th Joint Propulsion Conference*. American Institute of Aeronautics and Astronautics. _eprint: https://arc.aiaa.org/doi/pdf/10.2514/6.1991-2515.

Astra (2020). Astra Dedicated Launch Service. https://astra.com/services/.

Balesdent, M. (2011). *Multidisciplinary Design Optimization of Launch Vehicles.* PhD. Thesis, École Centrale de Nantes, Nantes, France.

Barrowman, J. S. (1967). The Practical Calculation of the Aerodynamic Characteristics of Slender Finned Vehicles. Master's thesis, The Catholic University of America, Washington DC.

Bayley, D. J. (2007). *Design Optimization of Space Launch Vehicles Using a Genetic Algorithm.* PhD. Thesis, Auburn University, Auburn, Alabama.

Bell, I. H., Wronski, J., Quoilin, S., and Lemort, V. (2014). Pure and Pseudo-pure Fluid Thermophysical Property Evaluation and the Open-Source Thermophysical Property Library CoolProp. *Industrial & Engineering Chemistry Research*, 53(6):2498–2508.

Blake, W. B. (1998). Missile Datcom: User's Manual - 1997 FORTRAN 90 Revision.

Bradford, J., Charania, A., and St. Germain, B. (2004). REDTOP-2: Rocket Engine Design Tool Featuring Engine Performance, Weight, Cost, and Reliability. In *40th AIAA/ASME/SAE/ASEE Joint Propulsion Conference and Exhibit*, Fort Lauderdale, Florida. American Institute of Aeronautics and Astronautics.

Brauer, G. L. C. (1975). Program to Optimize Simulated Trajectories (POST). Volume 1: Formulation manual. Technical report.

Bruhn, E. F. (1973). *Analysis and Design of Flight Vehicle Structures*. Tri-State Offset Company, U.S.A.

Bruno, T. (2019). Yes. The Amazing Centaur in its dual RL10 configuration. https://twitter.com/torybruno/status/1131638302761578496.

Cai, G., Zeng, P., Li, X., Tian, H., and Yu, N. (2013). Scale effect of fuel regression rate in hybrid rocket motor. *Aerospace Science and Technology*, 24(1):141–146.

Campbell, W. and Farquhar, J. (1973). Centrifugal Pumps for Rocket Engines. In *Pennsylvania State Univ. Fluid Mech., Acoustics, and Design of Turbomachinery, Pt. 2*. NTRS - NASA Technical Reports Server.

Casalino, L., Masseni, F., and Pastrone, D. (2019a). Robust Design of Hybrid Rocket Engine for Small Satellite Launchers. In *AIAA Propulsion and Energy 2019 Forum*, Indianapolis, IN. American Institute of Aeronautics and Astronautics. _eprint: https://arc.aiaa.org/doi/pdf/10.2514/6.2019-4096.

Casalino, L., Masseni, F., and Pastrone, D. (2019b). Viability of an Electrically Driven Pump-Fed Hybrid Rocket for Small Launcher Upper Stages. *Aerospace*, 6(3):36. Number: 3 Publisher: Multidisciplinary Digital Publishing Institute.

Casalino, L. and Pastrone, D. (2010a). Optimal Design of Hybrid Rocket Motors for Launch-

ers Upper Stages. *Journal of Propulsion and Power*, 26(3):421–427. Publisher: American Institute of Aeronautics and Astronautics _eprint: https://doi.org/10.2514/1.41856.

Casalino, L. and Pastrone, D. (2010b). Optimization of a Hybrid Rocket Upper Stage with Electric Pump Feed System. Nashville, TN. American Institute of Aeronautics and Astronautics. _eprint: https://arc.aiaa.org/doi/pdf/10.2514/6.2010-6954.

Castellini, F. (2012). *Multidisciplinary Design Optimization for Expendable Launch Vehicles*. PhD. Thesis, Politecnico di Milano, Milan, Italy.

Castellini, F. and Lavagna, M. R. (2012). Comparative Analysis of Global Techniques for Performance and Design Optimization of Launchers. *Journal of Spacecraft and Rockets*, 49(2):274–285. Publisher: American Institute of Aeronautics and Astronautics _eprint: https://doi.org/10.2514/1.51749.

Castellini, F., Lavagna, M. R., Riccardi, A., and Büskens, C. (2014). Quantitative Assessment of Multidisciplinary Design Models for Expendable Launch Vehicles. *Journal of Spacecraft and Rockets*, 51(1):343–359. Publisher: American Institute of Aeronautics and Astronautics _eprint: https://doi.org/10.2514/1.A32527.

Clark, S. (2016). Falcon 9 rocket explosion traced to upper stage helium system – Spaceflight Now. https://spaceflightnow.com/2016/09/23/falcon-9-rocket-explosion-traced-to-upper-stage-helium-system/.

Cramer, E., Frank, P., Shubin, G., and Dennis, Jr., J. (1992). On alternative problem formulations for multidisciplinary design optimization. In *4th Symposium on Multidisciplinary Analysis and Optimization*, Cleveland,OH,U.S.A. American Institute of Aeronautics and Astronautics.

Elvemar, P. (1990). Document number: TURLA-Ry-2.46 M5. Technical report.

Elzein, B., Gagnon, M., and Goulet-bourdon, M. (2020). Thrust Vector Control for Hybrid Propellants Rocket Engine with Embedded Fluid Injection Ports. *A1 US Patent.* https://www.freepatentsonline.com/y2020/0240365.html.

Faenza, M., Boiron, A. J., Haemmerli, B., and Verberne, C. J. (2019). The Nammo Nucleus Launch: Norwegian Hybrid Sounding Rocket over 100km. In *AIAA Propulsion and Energy 2019 Forum*, Indianapolis, IN. American Institute of Aeronautics and Astronautics. _eprint: https://arc.aiaa.org/doi/pdf/10.2514/6.2019-4049.

Fleeman, E. (2006). *Tactical Missile Design, Second Edition.* AIAA, Reston, VA, 2nd edition edition.

Fleeman, E. (2012). *Missile Design and System Engineering.* American Institute of Aeronautics and Astronautics, Inc., Washington, DC.

Gage, P. J. (1996). New approaches to optimization in aerospace conceptual design. page 1.

Galejs, R. (2018). Wind Instability- What Barrowman Left Out. https://www.argoshpr.ch/j3/articles/pdf/sentinel39-galejs.pdf.

Gavin, H. (2018). Structural Element Stiffness, Mass, and Damping Matrices. *Department of Civil and Environmental Engineering Duke University.* http://people.duke.edu/~hpgavin/cee541/StructuralElements.pdf.

Gegeoglu, K., Kahraman, M., Ucler, C., and Karabeyoglu, A. (2019). Assessment of Using Electric Pumps on Hybrid Rockets. Indianapolis, IN. American Institute of Aeronautics and Astronautics. _eprint: https://arc.aiaa.org/doi/pdf/10.2514/6.2019-4124.

Genevois, C., Deschamps, A., and Vacher, P. (2006). Comparative study on local and global mechanical properties of 2024 T351, 2024 T6 and 5251 O friction stir welds. *Materials Science and Engineering: A*, 415(1-2):162–170.

Graham, R., Lubachevsky, B., Nurmela, K., and Östergård, P. (1998). Dense packings of congruent circles in a circle. *Discrete Mathematics*, 181(1-3):139–154.

Greatrix, D. R. and Karpynczyk, J. (2005). Rocket Vehicle Design for Small-Payload Delivery to Orbit. *Canadian Aeronautics and Space Journal*, 51(3):123–131. Publisher: Canadian Aeronautics and Space Institute.

Guyver (2017). English: https://commons.wikimedia.org/wiki/File:Hybrids_big.png file , by Jonny.dyer , has been converted to svg file and multilingual support has been added for the following languages : English, Turkish, German, French, Spanish. Inkscape software was used.

Hammargren, K. (2018). Aerodynamics Modeling of Sounding Rockets: A Computational Fluid Dynamics Study. Master's thesis, Luleå University of Technology, Luleå, Sweden.

Hammond, W. E. (2001). *Design Methodologies for Space Transportation Systems*. American Institute of Aeronautics and Astronautics, Reston ,VA.

Hermsen, R. and Zandbergen, B. (2017). Pressurization system for a cryogenic propellant tank in a pressure-fed high-altitude rocket. In *7th European Conference for Aeronautics And Aerospace Sciences (EUCASS)*, page 13 pages, Milan Italy. Artwork Size: 13 pages Medium: PDF Publisher: Proceedings of the 7th European Conference for Aeronautics and Space Sciences. Milano, Italy, 3-6 july 2017.

Humble, R. D., Henry, G. N., and Larson, W. J. (1995). *Space propulsion analysis and design*. McGraw-Hill, New York,NY. OCLC: 758292712.

Huzel, D. K. and Huang, D. H. (1992). *Modern Engineering for Design of Liquid Propellant Rocket Engines*. American Institute of Aeronautics and Astronautics, Inc., Washington, DC.

Johnson, D. and Vaughan, W. (2000). Terrestrial Environment (Climatic) Criteria Handbook for Use in Aerospace Vehicle Development. *NASA Technical Standards.*

Karabeyoglu, A., Stevens, J., Geyzel, D., Cantwell, B., and Micheletti, D. (2011). High Performance Hybrid Upper Stage Motor. San Diego, California. American Institute of Aeronautics and Astronautics. _eprint: https://arc.aiaa.org/doi/pdf/10.2514/6.2011-6025.

Karabeyoglu, M. A., Altman, D., and Cantwell, B. J. (2002). Combustion of Liquefying Hybrid Propellants: Part 1, General Theory. *Journal of Propulsion and Power*, 18(3):610–620. Publisher: American Institute of Aeronautics and Astronautics _eprint: https://doi.org/10.2514/2.5975.

Karabeyoglu, M. A., Cantwell, B. J., and Zilliac, G. (2007). Development of Scalable Space-Time Averaged Regression Rate Expressions for Hybrid Rockets. *Journal of Propulsion and Power*, 23(4):737–747. Publisher: American Institute of Aeronautics and Astronautics.

Karolewska, K. and Ligaj, B. (2019). Comparison analysis of titanium alloy Ti6Al4V produced by metallurgical and 3D printing method. page 020025, Bydgoszcz, Poland.

Koko90 and Patrick87 (2011). Circle packing in a circle images. Wikimedia Commons, https://commons.wikimedia.org/wiki/File:Disk_pack9.svg.

Krevor, Z. C. (2007). *A Methodology to Link Cost and Reliability for Launch Vehicle Design.* PhD. Thesis, Georgia Tech, Atlanta, GA.

Kuo, K. K. and Chiaverini, M. J., editors (2007). *Fundamentals of Hybrid Rocket Combustion and Propulsion.* American Institute of Aeronautics and Astronautics, Reston ,VA.

Kwak, H.-D., Kwon, S., and Choi, C.-H. (2018). Performance assessment of electrically driven pump-fed LOX/kerosene cycle rocket engine: Comparison with gas generator cycle. *Aerospace Science and Technology*, 77:67–82.

Larson, W. J. and Wetrz, J. R., editors (1999). *Space Mission Analysis and Design.* Microcosm, El Segundo, Calif. : Dordrecht ; Boston.

Luzum, B., Capitaine, N., Fienga, A., Folkner, W., Fukushima, T., Hilton, J., Hohenkerk, C., Krasinsky, G., Petit, G., Pitjeva, E., Soffel, M., and Wallace, P. (2011). The IAU 2009 system of astronomical constants: the report of the IAU working group on numerical standards for Fundamental Astronomy. *Celestial Mechanics and Dynamical Astronomy*, 110(4):293.

Martins, J. R. R. A. and Lambe, A. B. (2013). Multidisciplinary Design Optimization: A Survey of Architectures. *AIAA Journal*, 51(9):2049–2075. Publisher: American Institute of Aeronautics and Astronautics.

McLean, F. (2020). OrbitalPy: High level orbital mechanics package.

Messerchmitt-Boelkow-Blohm, G. (1970). Data Sheets for the Determination of Normal Force, Moment, and Tangential Force Characteritics of Slender Nose-Cylinder Configurations in the Transonic Speed Regime.

Messinger, T., Hill, C., Quinn, D., Stannard, D., Doerksen, G., and Johansen, C. T. (2019). Development and Test Flight of The Atlantis I Nitrous Oxide/Paraffin-based Hybrid Rocket. In *AIAA Propulsion and Energy 2019 Forum*, AIAA Paper 2019-4011.

Miranda, F. (2015). Design Optimization of Ground and Air-Launched Hybrid Rockets. Master's thesis, TU Delft, Mekelweg, Netherlands.

Miranda, L. J. (2018). PySwarms: a research toolkit for Particle Swarm Optimization in Python. *Journal of Open Source Software*, 3(21):433.

Moore, W. (1813). *A Treatise on the Motion of Rockets: to which is added, an Essay on Naval Gunnery, in theory and practice, etc.* G. & S. Robinson ;, London. OCLC: 83918937.

Moser, T. (2003). Space Shuttle Orbiter Structural Design. https://www.nasa.gov/centers/johnson/pdf/584733main_Wings-ch4g-pgs270-285.pdf.

Mota, F. A. d. S. (2015). *Modeling and Simulation of Launch Vehicles Using Object-Oriented Programming*. PhD. Thesis, Instituto Nacional de Pesquisas Espaciais, São José dos Campos.

Murri, D. G., Jackson, E. B., and Shelton, R. O. (2015). Check-Cases for Verification of 6-Degree-of-Freedom Flight Vehicle Simulations: NASA/TM 2015-218675. *NASA Technical Memo*, 1.

Musk, E. (2015). First time anyone has gone this low for O2. - Twitter post. https://twitter.com/elonmusk/status/677663227271118848.

Niskanen, S. (2009). Development of an Open Source model rocket simulation software. Master's thesis, Helsinki University of Technology, Helsinki, Finland.

NOAA (1976). US Standard Atmosphere 1976. Technical report, NASA-TM-X-74335, Joint NOAA, NASA, and USAF publication, Washington, DC.

Paccagnella, E., Santi, M., Ruffin, A., Barato, F., Pavarin, D., Misté, G. A., Venturelli, G., and Bellomo, N. (2019). Testing of a Long-Burning-Time Paraffin-Based Hybrid Rocket Motor. *Journal of Propulsion and Power*, 35(2):432–442. Publisher: American Institute of Aeronautics and Astronautics _eprint: https://doi.org/10.2514/1.B37144.

Peterson, J. P., Seide, P., and Weingarten, V. I. (1968). Buckling of thin-walled circular cylinders. Technical Report NASA SP-8007, NASA, United States.

Rachov, P. A. P., Tacca, H., and Lentini, D. (2013). Electric Feed Systems for Liquid-Propellant Rockets. *Journal of Propulsion and Power*, 29(5):1171–1180.

Reed, B., Bigalow, J., and Schneider, S. (1997). Iridium-Coated Rhenium Radiation-Cooled Rockets) NASA-TM-107453. Technical Report NASA-TM-107453.

Ribeiro, M. V. F. and Junior, P. C. G. (2011). Hybrid Rocket Motors Propellants: A Historical Approach. Natal, RN, Brazil.

RocketLab (2020a). Rocket Lab - I Can't Believe It's Not Optical Launch 08/31/2020. https://www.youtube.com/watch?v=FPIhI5mRDRI&t=1292s&ab_channel=RocketLab.

RocketLab (2020b). Rocket Lab | Electron - satellite launch vehicle. https://www.rocketlabusa.com/electron/.

Sanford, G. and Mcbride, B. (1994). Computer Program for Calculation of Complex Chemical Equilibrium Compositions and Applications. Part 1: Analysis. NASA-RP-1311.

Schmierer, C., Kobald, M., Fischer, U., Tomolin, K., Petraralo, A., and Hertel, F. (2019a). Advancing Europes Hybrid Rocket Engine Technology with Paraffin and LOX.

Schmierer, C., Kobald, M., Tomilin, K., Fischer, U., and Schlechtriem, S. (2019b). Low Cost Small-Satellite Access to Space Using Hybrid Rocket Propulsion. *Acta Astronautica*, 159:578–583.

SpaceX (2020). Eleventh Starlink Mission Launch (SpaceX) 18/08/2020. https://www.youtube.com/watch?v=jTMJK7wb0rM&t=1062s&ab_channel=SpaceX.

Stark, R. (2005). Flow Separation in Rocket Nozzles, a Simple Criteria. In *41st AIAA/ASME/SAE/ASEE Joint Propulsion Conference & Exhibit*, Tucson, Arizona. American Institute of Aeronautics and Astronautics.

Sutton, G. P. and Biblarz, O. (2001). *Rocket propulsion elements*. John Wiley & Sons, New York, 7th ed edition.

Tewari, A. (2007). *Atmospheric and Space Flight Dynamics: Modeling and Simulation with MATLAB® and Simulink®*. Birkhäuser.

Tizón, J. M. and Roman, A. (2017). A Mass Model for Liquid Propellant Rocket Engines. In *53rd AIAA/SAE/ASEE Joint Propulsion Conference*, AIAA Propulsion and Energy Forum, Atlanta, GA. American Institute of Aeronautics and Astronautics.

Uddanti, N. S. (2015). Analysis of a Hybrid Rocket Burn Using Generalized Compressible Flow. Master's thesis, Embry–Riddle Aeronautical University.

Vallado, D. A. (2010). *Fundamentals of Astrodynamics and Applications*. Microcosm Press/Springer, Hawthorne, Calif.

Van Kesteren, M. W. (2013). Air Launch versus Ground Launch: A Multidisciplinary Design Optimization Study of Expendable Launch Vehicles on Cost and Performance. Master's thesis, TU Delft, Mekelweg, Netherlands.

Virtanen, P., Gommers, R., Oliphant, T. E., Haberland, M., Reddy, T., Cournapeau, D., Burovski, E., Peterson, P., Weckesser, W., Bright, J., van der Walt, S. J., Brett, M., Wilson, J., Millman, K. J., Mayorov, N., Nelson, A. R. J., Jones, E., Kern, R., Larson, E., Carey, C. J., Polat, l., Feng, Y., Moore, E. W., VanderPlas, J., Laxalde, D., Perktold, J., Cimrman, R., Henriksen, I., Quintero, E. A., Harris, C. R., Archibald, A. M., Ribeiro, A. H., Pedregosa, F., and van Mulbregt, P. (2020). SciPy 1.0: fundamental algorithms for scientific computing in Python. *Nature Methods*, 17(3):261–272. Number: 3 Publisher: Nature Publishing Group.

Whitehead, J. (2005). How Small Can a Launch Vehicle Be? Joint Propulsion Conferences, Tucson, Arizona. American Institute of Aeronautics and Astronautics.

Wildvank, R. (2018). Launch vehicle structural mass prediction model. Master's thesis, Delft University of Technology, Delft Netherlands.

Woodward, D. (2017). Space Launch Vehicle Design. Master's thesis, University of Texas at Arlington, Arlington, Texas.

Young, W. C., Budynas, R. G., and Sadegh, A. M. (2011). *Roark's Formulas for Stress and Strain, 8th Edition*. McGraw-Hill Education, New York.

Zimmerman, J. E., Waxman, B. S., Cantwell, B., and Zilliac, G. (2013). Review and Evaluation of Models for Self-Pressurizing Propellant Tank Dynamics. In *49th AIAA/ASME/SAE/ASEE Joint Propulsion Conference*, San Jose, CA. American Institute of Aeronautics and Astronautics.

Zucker, A. J., King, T. K., and Ngo, K. C. (1989). Contamination of liquid oxygen by pressurized gaseous nitrogen. Technical Publication NASA TP-2894, NASA, United States.

Appendix A

Beam Element Mass and Stiffness Matrices

The beam element mass and stiffness matrices are from Gavin (2018), and shown in the following:

$$
M = \frac{\rho A L}{420}
\begin{bmatrix}
140 & 0 & 0 & 70 & 0 & 0 \\
0 & 156 & 22L & 0 & 54 & -13L \\
0 & 22L & 4L^2 & 0 & 13L & -3L^2 \\
70 & 0 & 0 & 140 & 0 & 0 \\
0 & 54 & 13L & 0 & 156 & -22L \\
0 & -13L & -3L^2 & 0 & -22L & 4L^2
\end{bmatrix}
\tag{A.1}
$$

$$
K =
\begin{bmatrix}
\frac{EA}{L} & 0 & 0 & -\frac{EA}{L} & 0 & 0 \\
0 & \frac{12EI}{L^3} & \frac{6EI}{L^2} & 0 & -\frac{12EI}{L^3} & \frac{6EI}{L^2} \\
0 & \frac{6EI}{L^2} & \frac{4EI}{L} & 0 & -\frac{6EI}{L^2} & \frac{2EI}{L} \\
-\frac{EA}{L} & 0 & 0 & \frac{EA}{L} & 0 & 0 \\
0 & -\frac{12EI}{L^3} & -\frac{6EI}{L^2} & 0 & \frac{12EI}{L^3} & -\frac{6EI}{L^2} \\
0 & \frac{6EI}{L^2} & \frac{2EI}{L} & 0 & -\frac{6EI}{L^2} & \frac{4EI}{L}
\end{bmatrix}
\tag{A.2}
$$

Appendix B

Input Constants

Variable name (symbol)	Value
Nosecone type	Ogive
Nosecone bluntness ratio	0.05
Nosecone fineness ratio	1.5
Nosecone material	2024-T3
Nosecone safety factor	2.0
Nose fairing separation altitude	110 km
Upper-tank safety factor	1.5
Upper-tank material	2024-T3
Upper-tank extra mass	1 kg
Upper-tank extra mass density	100 kg/m^3
Interstage safety factor	1.5
Interstage material	2024-T3
Interstage extra mass	1 kg
Interstage extra mass density	100 kg/m^3
Inter-tank safety factor	1.5
Inter-tank material	2024-T3
Inter-tank extra mass	0.5 kg
Inter-tank extra mass density	100 kg/m^3
Pressurant tank material	Ti-6Al-4V
Pressurant tank safety factor	1.5
Oxidizer tank safety factor	1.5
Oxidizer tank material	2024-T3
Oxidizer tank end cap type	Spherical
Pressure-stabilized on-pad	False
Combustion chamber safety factor	2.0
Combustion chamber material	Ti-6Al-4V
Chamber insulation thickness	3 mm
Chamber insulation mass density	1000 kg/m^3
Engine section skirt safety factor	1.5
Engine section skirt material	2024-T3
Thrust structure material	2024-T3
Thrust structure safety factor	2.0
Nozzle bell material	Ir-Coated Re
Nozzle bell safety factor	2.0
Axial mode frequency limit	25 Hz
Bending mode frequency limit	10 Hz
Surface roughness height	200 μm

Table B.1: Aerostructure constants

159

Variable name (symbol)	Value
Oxidizer type	LOx / N$_2$O
Pressurant type	He / N$_2$
Fuel type	Paraffin
Feed system type	e-pump / back-fill / self-press
Combustion efficiency (η_c)	95 %
Combustion chamber pre calibers	1.0
Combustion chamber post calibers	1.5
Combustion pressure fluctuations (P_{fluct})	5 %
Maximum allowable fuel port flux	500 $\frac{kg}{m^2 s}$
Electric pump power density	3.9 kW/kg
Electric pump mass density	500 kg/m^3
Electric pump NPSP	350 kPa
Electric pump efficiency	66 %
Battery energy density	324 kJ/kg
Battery power density	3.0 kW/kg
Battery mass density	1000 kg/m^3
Valve mass density	500 kg/m^3
On-pad oxidizer vent time	1800 s

Table B.2: Propulsion input constants

Variable name (symbol)	Value
Initial pitch-over rate	0.005 rad/s
Initial pitch-over altitude	100 m
Control type	Active
Bilinear tangent initial angle	Post-staging heading
Bilinear tangent final angle	0 rad
Target apogee	500 km
Target perigee	500 km
Target SECO-1 altitude	200 km
Circularize	True
Launch elevation (ASL)	0.0 m
Launch latitude	0.0 rad
Launch longitude	0.0 rad
Launch azimuth	$\pi/2$ rad (polar)
Maximum wind gust magnitude	9 m/s
Synthetic wind profile reference altitude 1	12 km
Synthetic wind profile reference altitude 2	50 km
Stage separation coast time	1 s

Table B.3: Trajectory/environment input constants

Appendix C

LEE150 Supplementary Output
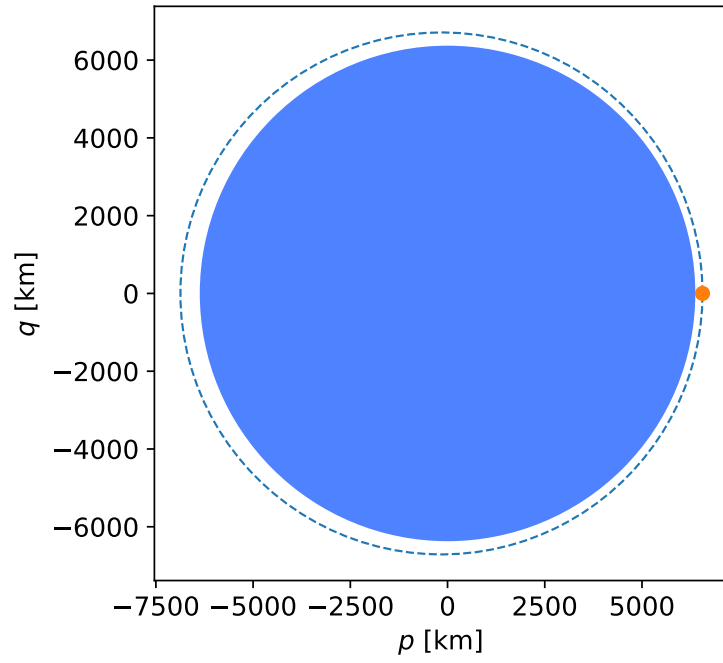
C.1 Mission Plots

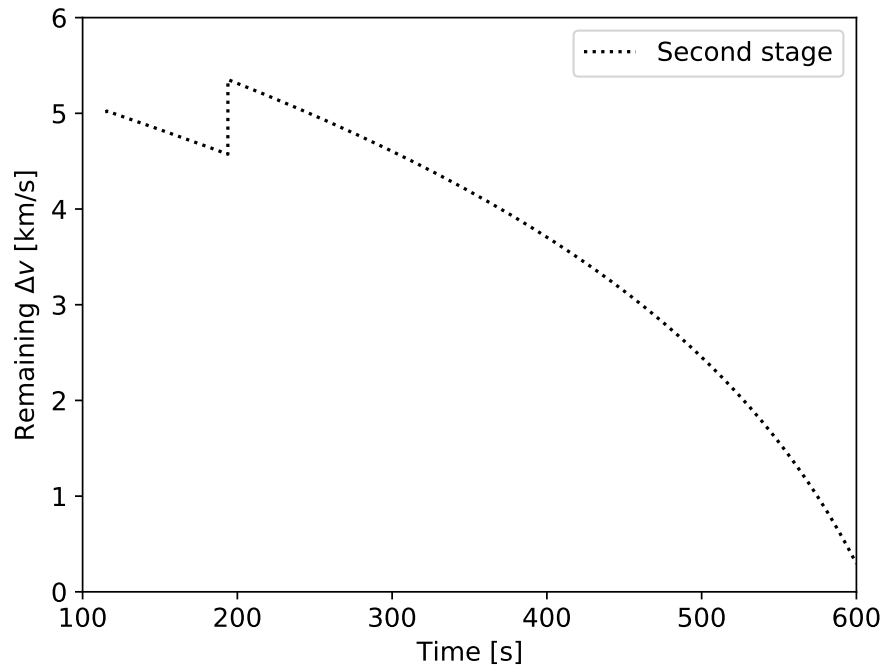Figure C.1: Initial elliptic orbit path for LEE150

Figure C.2: Upper stage remaining ΔV vs time since first stage ignition, for LEE150
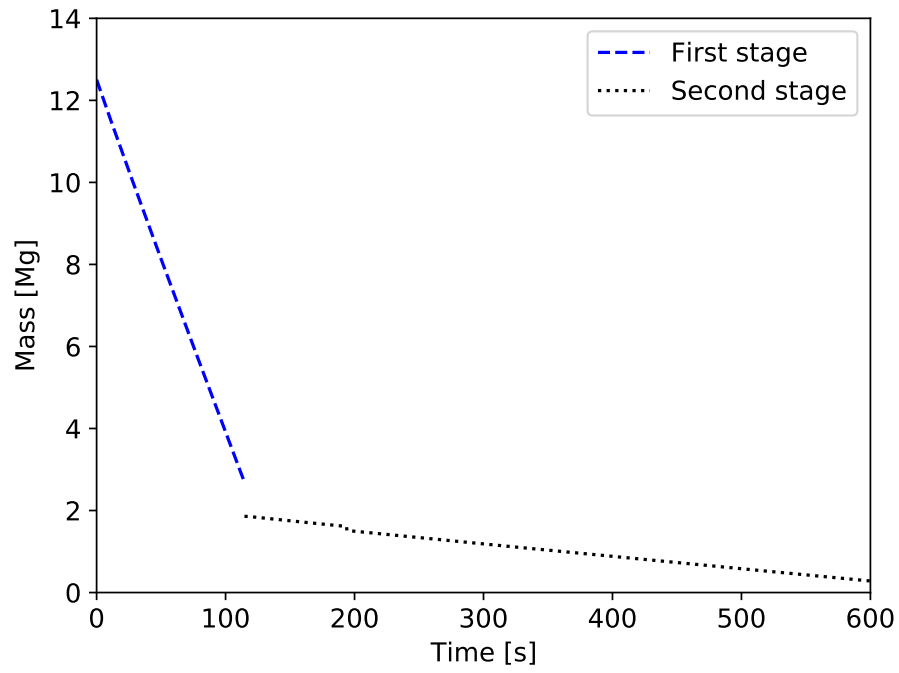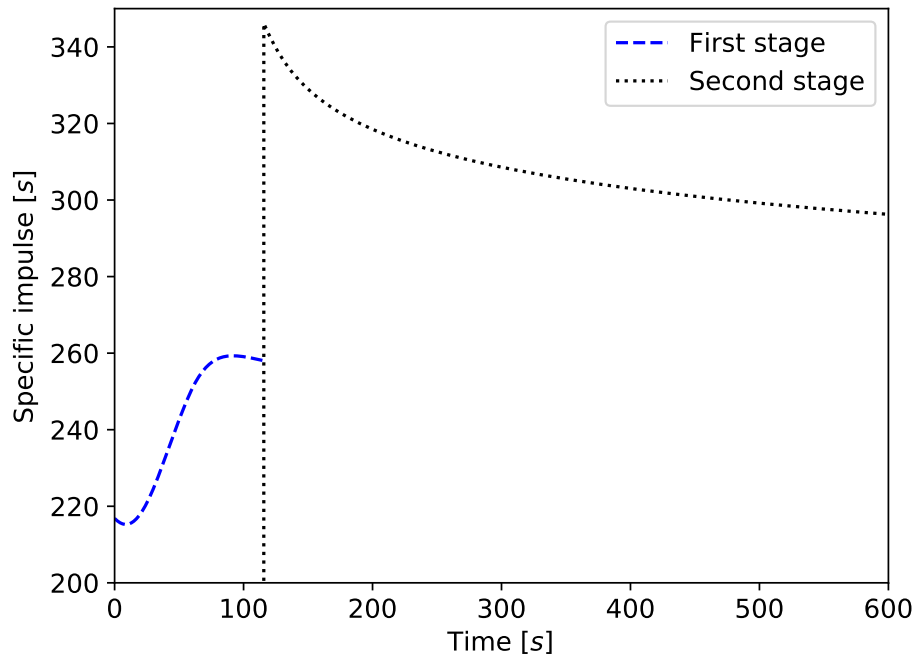
Figure C.3: Total mass vs time for LEE150

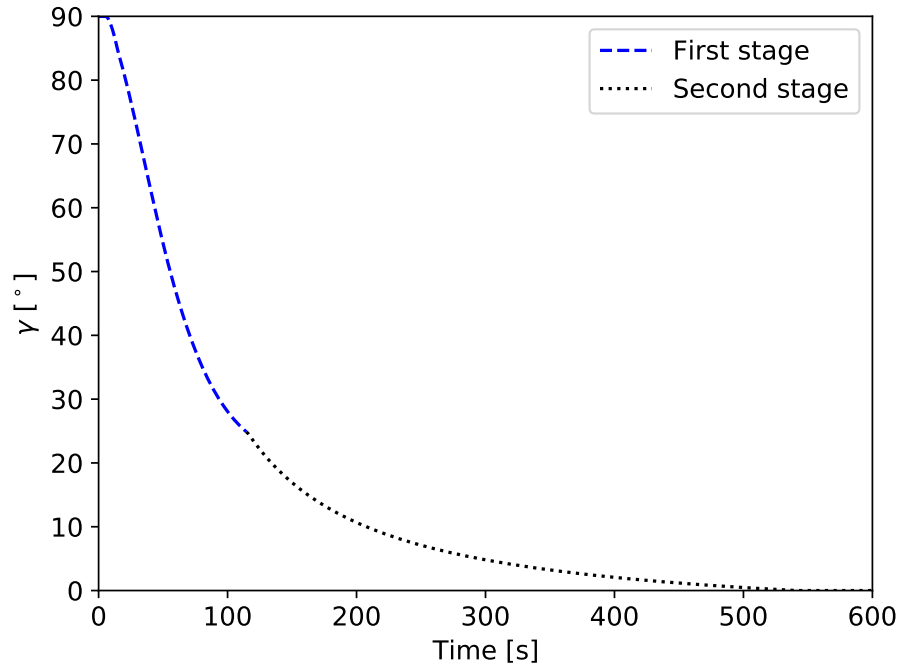Figure C.4: Specific impulse vs time into burn for LEE150

163

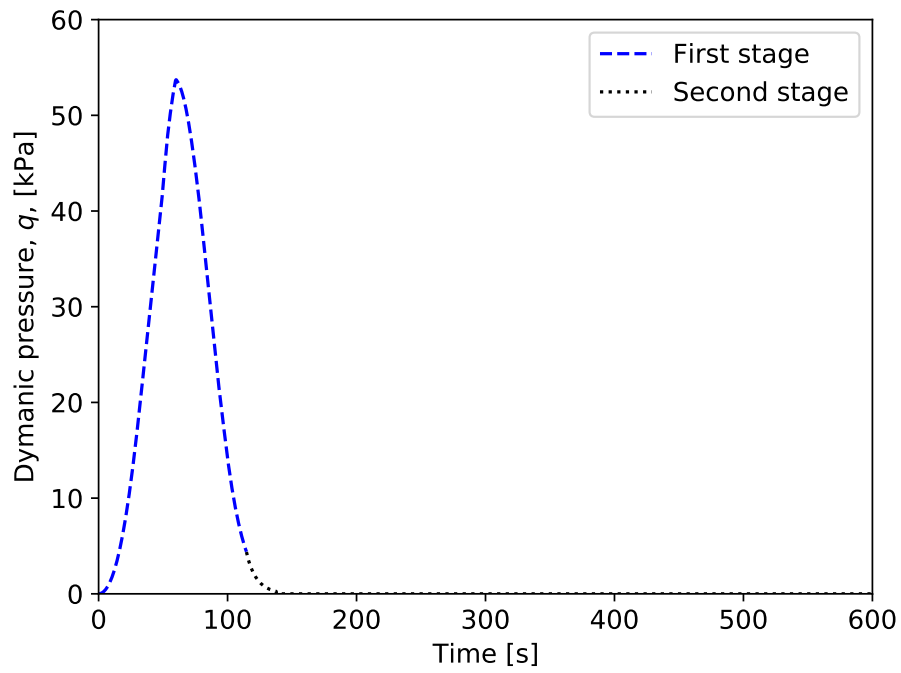Figure C.5: Local flight heading, γ, vs time for LEE150

Figure C.6: Dynamic pressure, q, vs time for LEE150

C.2   Code Outputs

First stage burn time: 114.6 s
Second stage available burn time: 493.2 s
Second engine cut-off-1 time: 606.3 s
Remaining burn time in 2nd stage: 2.5 s
Second engine cut-off-1 altitude: 185.586 km
Second engine cut-off-1 velocity: 7.888 km/s
Maximum Mach number, upper stage: 8.998
Maximum Mach number, combined: 7.965
Gross takeoff mass: 12488 kg
Takeoff dry mass: 1349 kg
Propellant mass percentage, combined: 89.2 %
Payload fraction of gross mass: 1.201 %
Payload fraction of dry mass: 11.114 %
Upper stage wet mass: 1858 kg
Burnout Mass: 263 kg
Maximum acceleration, upper stage: 3.444 gs
Maximum acceleration, combined: 7.682 gs
Vehicle body outer diameter: 1.58 m
Vehicle aspect ratio: 11.4
Upper stage remaining Delta V: 2.7 m/s

————————————————-

Detailed info: first/main stage:

————————————————-

Number of engines: 7
Nominal combustion chamber pressure: 1032.733 kPa
Nominal, initial conditions total impulse: 19711.51 kN-s
Nominal, initial conditions thrust per engine: 24.57 kN
Delivered average thrust per engine: 28.97 kN
Single engine oxidizer flow rate: 8.29 kg/s
Single fuel grain outer diameter: 51.85 cm
Single fuel grain inner diameter: 15.827 cm
Single fuel grain length: 262.208 cm
Single fuel grain mass: 449.58 kg
Nozzle throat diameter: 15.827 cm
Nozzle exit diameter: 30.198 cm
Nozzle length: 52.41 cm
Fuel name: Paraffin(C73H124)
Fuel mass (total) 3147.08 kg
Oxidizer name: Oxygen
Oxidizer mass: 6650.1 kg
Pressurant tank mass: 51.78 kg
Pressurant gas mass: 5.96 kg

Electric pump mass (total): 23.99 kg
Electric pump battery mass (total): 39.73 kg

————————————————————-

Detailed info: upper stage:

————————————————————-

Number of engines: 1
Nominal combustion chamber pressure: 846.903 kPa
Nominal, initial conditions total impulse: 4548.67 kN-s
Nominal, initial conditions thrust per engine: 9.22 kN
Delivered average thrust per engine: 9.22 kN
Single engine oxidizer flow rate: 2.24 kg/s
Single fuel grain outer diameter: 67.308 cm
Single fuel grain inner diameter: 8.633 cm
Single fuel grain length: 129.294 cm
Single fuel grain mass: 403.57 kg
Nozzle throat diameter: 8.633 cm
Nozzle exit diameter: 67.38 cm
Nozzle length: 155.302 cm
Fuel name: Paraffin(C73H124)
Fuel mass (total) 403.57 kg
Oxidizer name: Oxygen
Oxidizer mass: 1103.07 kg
Pressurant tank mass: 8.59 kg
Pressurant gas mass: 0.99 kg
Electric pump mass (total): 0.71 kg
Electric pump battery mass (total): 5.06 kg

————————————————————-

Rocket element info for first/main stage:

————————————————————-

Nosecone
Material: 2024-T6
Wall thickness: 1.932 mm
Section length: 2.37 m

————————————————————-

Upper-tank
Material: 2024-T6
Wall thickness: 1.769 mm
Section length: 0.34 m

————————————————————-

Oxidizer tank
Material: 2024-T6
Wall thickness: 1.244 mm
Section length: 0.51 m

————————————————————-

Interstage

Material: 2024-T6
Wall thickness: 2.64 mm
Section length: 4.55 m

———————————————————————-

Upper-tank
Material: 2024-T6
Wall thickness: 2.851 mm
Section length: 1.42 m

———————————————————————-

Oxidizer tank
Material: 2024-T6
Wall thickness: 2.094 mm
Section length: 3.55 m

———————————————————————-

Inter-tank
Material: 2024-T6
Wall thickness: 3.516 mm
Section length: 0.86 m

———————————————————————-

Engine
Material: 2024-T6
Wall thickness: 1.455 mm
Section length: 4.46 m

———————————————————————-